NASA/CR—1999-208879

UTRC Report R98–4.101.0255

Development of a Linearized Unsteady Euler Analysis With Application to Wake/Blade-Row Interactions

Joseph M. Verdon, Matthew D. Montgomery, and H. Andrew Chuang
United Technologies Research Center, East Hartford, Connecticut

Prepared under Contract NAS3–27727

National Aeronautics and
Space Administration

Glenn Research Center

March 1999

Available from

NASA Center for Aerospace Information
7121 Standard Drive
Hanover, MD 21076
Price Code: A05

National Technical Information Service
5285 Port Royal Road
Springfield, VA 22100
Price Code: A05

Development of a Linearized Unsteady Euler Analysis with Application to Wake/Blade-Row Interactions

Contents

Summary 1

1 Introduction 2

2 Unsteady Flow through a Blade Row 4

3 Unsteady Aerodynamic Formulations 6
- 3.1 Linearized Unsteady Aerodynamic Model 7
- 3.2 Solution Strategy 10

4 Near-Field Numerical Model 11
- 4.1 Finite Volume Equations 11
- 4.2 Evaluation of Flux Terms and Pseudo-Time Integration 12

5 Unsteady Perturbations in the Far-Field 15
- 5.1 Uniform Mean Flow 16
- 5.2 Nonuniform Mean Flow 18
- 5.3 Numerical Results for Simple Swirling Flows 21

6 Analytic Wake Excitation Model 25

7 Numerical Results: 3D 10th Standard Configuration 28
- 7.1 Steady Background Flow/Vortical Excitations 29
- 7.2 Unsteady Response Predictions 30

8 Numerical Results: Fan Exit Guide Vane 34
- 8.1 Rotor-Exit/Stator-Inlet Conditions 35
- 8.2 Steady Background Flow 38
- 8.3 Unsteady Response Predictions 39

9 Concluding Remarks 43

References 46

List of Figures 50

Figures 1 through 50 54

Development of a Linearized Unsteady Euler Analysis with Application to Wake/Blade-Row Interactions

Joseph M. Verdon, Matthew D. Montgomery and H. Andrew Chuang
United Technologies Research Center
East Hartford, CT 06108

Summary

A three-dimensional, linearized, Euler analysis is being developed to provide a comprehensive and efficient unsteady aerodynamic analysis for predicting the aeroacoustic and aeroelastic responses of axial-flow turbomachinery blading. The mathematical models needed to describe nonlinear and linearized, inviscid, unsteady flows through a blade row operating within a cylindrical annular duct are presented in this report. A numerical model for linearized inviscid unsteady flows, which couples a near-field, implicit, wave-split, finite volume analysis to far-field eigenanalyses, is also described. The linearized aerodynamic and numerical models have been implemented into the three-dimensional unsteady flow code, LINFLUX. This code is applied herein to predict unsteady subsonic flows driven by wake or vortical excitations. The intent is to validate the LINFLUX analysis via numerical results for simple benchmark unsteady flows and to demonstrate this analysis via application to a realistic wake/blade-row interaction. Detailed numerical results for a three-dimensional version of the 10th Standard Cascade and a fan exit guide vane indicate that LINFLUX is becoming a reliable and useful unsteady aerodynamic prediction capability that can be applied, in the future, to assess the three-dimensional, flow physics important to blade-row aeroacoustic and aeroelastic responses.

1. Introduction

The development of analyses to predict unsteady flows in turbomachines has been motivated primarily by the need to predict the aeroelastic (flutter and forced vibration) and aeroacoustic (sound generation and propagation) characteristics of the blading. Accurate and efficient aerodynamic analyses are needed to determine the unsteady loads that act on the blades and the unsteady pressure responses that persist upstream and downstream of the blade row for various sources of excitation. The latter include prescribed structural (blade) motions and prescribed aerodynamic disturbances at inlet and exit that carry energy towards the blade row. The computational resources required to simulate nonlinear and viscous unsteady fluid dynamic behavior continue to prohibit the use of such simulations in detailed aeroelastic and aeroacoustic design studies. Therefore, approximate, e.g., linearized inviscid, analyses are still needed to provide efficient predictions of unsteady response phenomena.

Until recently, the linearized analyses available for turbomachinery aeroelastic and aeroacoustic applications have been based on two- and three-dimensional, classical methods, see [Whi87, Nam87] for reviews. Such methods are very efficient, but are restricted to shock-free flows through lightly loaded blade rows. Because of these limitations, two-dimensional linearizations relative to nonuniform potential mean flows have been developed, see [Ver93] for a review. Such analyses account for the effects of real blade geometry, mean blade loading, and operation at transonic Mach numbers on unsteady aerodynamic response. The physical understanding and computational efficiencies offered by the classical and potential-based linearizations have motivated the recent development of more comprehensive linearizations to address flows in which strong shocks occur and three-dimensional unsteady flows in which the effects of mean swirl are important. For such flows, the nonlinear Euler equations are required to model the nonisentropic and rotational steady background flow and linearized versions of these equations are required to model the unsteady perturbations.

Thus, much attention is currently being given to the development of two- [HC93a, HC93b, KK93, MV95] and three-dimensional [HL93, HCL94, Sre96, MV97, MG98, MV98] linearized Euler analyses. In particular, the present authors have developed two- and three-dimensional versions of the LINFLUX analysis. This analysis consists of a near-field, implicit, finite-volume analysis to determine the unsteady perturbation of the mean flow through the blade row, and far-field eigenanalyses to determine the unsteady perturbations of fully-developed, axisymmetric, mean flows at inlet and exit. The near-field analysis is based upon the high-resolution, wave-split, finite-volume scheme [WJS88], which is employed in the nonlinear steady and unsteady flow analysis TURBO [Jan89, JHW92, CW93]. The flux or wave splitting allows a sharp resolution of nonlinear shock phenomena — a feature which should facilitate the accurate prediction of impulsive unsteady shock loads with the linearized analysis. The far-field eigenanalyses, which are coupled to the near-field, finite-volume analysis at the computational inflow and outflow boundaries, have been constructed to allow incoming external aerodynamic excitations to be prescribed, and outgoing response disturbances to pass through these computational boundaries without reflection.

The 2D LINFLUX analysis is reported in [MV95, VMK95] along with numerical results for subsonic and transonic unsteady flows through the 10th Standard Cascade [FV93], that are excited by prescribed blade motions or by prescribed external aerodynamic disturbances. Comparisons of the 2D LINFLUX results with those of the potential-based linearization,

LINFLO [VC84, UV91, HV91], and the nonlinear Euler/Navier-Stokes analysis, NPHASE [HSR91, SLH+94], indicate that the former gives accurate response information for the various sources of unsteady excitation. However, improvements in the numerical modeling in the vicinity of shocks and near blade surfaces would lead to better resolutions of unsteady transonic flows and unsteady flows excited by vortical gusts, respectively.

The 3D LINFLUX analysis has been reported in [MV97, MV98] along with numerical results for subsonic unsteady flows through a helical fan and a three-dimensional version of the 10th Standard Cascade (3D SC10) excited by prescribed blade motions or acoustic disturbances at inlet and exit. To allow comparisons with 2D theories, the helical fan and 3D SC10 have high hub to tip ratios, and were subjected to nearly two-dimensional unsteady excitations. For the most part, the 3D LINFLUX results at blade midspan were found to be in very good agreement with those of the classical 2D analysis of Smith [Smi72], for the helical fan, and those of the 2D LINFLO analysis, for the 3D SC10.

Under the present effort, the 3D LINFLUX analysis has been extended and applied to predict three-dimensional, unsteady, subsonic flows that are driven by vortical or wake excitations at inlet. In principle, such excitations must be prescribed as solutions of the governing flow equations. However, this is not feasable, at present, for the unsteady perturbations of three-dimensional, nonuniform, mean flows. Thus, as an interim practical approach, based on exact solutions for uniform mean flows and a numerical study described in §5.3 of this report, we have represented vortical excitations as convected velocity disturbances that carry no pressure or density. These disturbances satisfy the fluid-dynamic conservation equations axially and circumferentially, at each radial station, but radial momentum is not conserved.

We will consider vortically-excited unsteady flows through rotor and stator blade rows, and present numerical results for the axial eigenvalues, radial eigenmodes, and the amplitudes of the far-field acoustic responses, the unsteady pressure fields and the unsteady pressures acting at the blade surfaces. In each case the mean or steady background flow is determined using the TURBO analysis, and the unsteady perturbation is determined using LINFLUX.

The rotor is the three-dimensional version of the 10th Standard Cascade studied in [MV97, MV98]. For validation purposes, we have subjected this rotor to relatively simple vortical excitations, and have compared the 3D LINFLUX results at midspan with those of the 2D LINFLO analysis. The stator is the fan exit guide vane (FEGV) of the NASA/PW 22 inch Advanced Ducted Propulsor [Neu97, Pod97]. Here, the wake excitation is based on velocity measurements, taken downstream of the fan rotor, at NASA Lewis Research Center [Pod97]. However, a number of simplifying physical assumptions, as outlined in §6 and §8.1, have been introduced to approximate the actual inflow conditions to the FEGV by an analytical representation that is suitable for use with LINFLUX.

The numerical results, presented both previously and in this report, indicate that the 3D LINFLUX analysis is becoming a reliable and useful unsteady aerodynamic prediction capability for determining the unsteady pressure responses of blade rows to various sources of unsteady excitation. In particular, this analysis promises to be a valuable resource for understanding the flow physics associated with blade-row aeroelastic and aeroacoustic responses. Improvements in the modeling of steady inflow conditions and unsteady wake excitations are still needed, however, so that the unsteady pressure responses associated with realistic wake/blade-row interactions can be predicted accurately.

2. Unsteady Flow through a Blade Row

We consider time-dependent adiabatic flow, with negligible body forces, of an inviscid non-heat conducting perfect gas through a vibrating, rotor or stator, blade row (see Figure 1). The blade row operates within a long stationary annular duct which has hub and duct radii of $r = r_H$ and $r = r_D$, respectively. It consists of N_B blades which, in the case of a rotor, rotate about the duct axis at constant angular velocity $\mathbf{\Omega} = \Omega \mathbf{e}_\xi$; for a stator, $\Omega = 0$. In the absence of vibratory motion, the blades are identical in shape, equally spaced around the rotor, and identical in orientation relative to an axisymmetric inlet flow.

We will analyze this unsteady flow in a reference frame that rotates with the blade row, in terms of cylindrical $(r,\ \theta,\ \xi,\ t)$ and Cartesian $(x_1, x_2, x_3, t) = (\xi,\ r\sin\theta,\ -r\cos\theta, t)$ coordinates. Here ξ and r measure distance in the axial flow direction and radially outward from the duct axis, respectively, θ measures angular distance in the $\mathbf{e}_\xi \times \mathbf{e}_r = \mathbf{e}_\theta$ direction, which, for a rotor, is opposite to the direction of blade rotation, and $\mathbf{e}$ is a unit vector. We will also have occasion to examine a rotor flow in a stationary reference frame, and a stator flow in a rotating frame. Thus, when needed for clarity, we will use the superscripts rel or abs to indicate that a physical quantity is measured relative to a rotating or stationary frame of reference, respectively; e.g., $\theta^{\text{abs}} = \theta^{\text{rel}} + \Omega t$.

To describe flows in which the fluid domain deforms with time, it is useful to consider two sets of independent variables, say $(\mathbf{x}, t)$ and $(\bar{\mathbf{x}}, t)$. The position vector $\mathbf{x}(\bar{\mathbf{x}}, t) = \bar{\mathbf{x}} + \boldsymbol{\mathcal{R}}(\bar{\mathbf{x}}, t)$ describes the instantaneous location, in the blade row frame of reference, of a moving field point, $\bar{\mathbf{x}}$ refers to the reference or mean position of this point, and $\boldsymbol{\mathcal{R}}(\bar{\mathbf{x}}, t)$ is the displacement of the point from its reference position. The displacement field, $\boldsymbol{\mathcal{R}}$, is prescribed so that the solution domain deforms with the vibratory motions of the blades and is rigid far from the blade row. Thus, if the blades do not vibrate, $\boldsymbol{\mathcal{R}}$ is simply set equal to zero.

In the present discussion, the physical variables are, for the most part, reported in dimensionless form. Lengths have been scaled with respect to the reference length L^*_{Ref}, time with respect to the ratio $L^*_{\text{Ref}}/V^*_{\text{Ref}}$ where V^*_{Ref} is the reference flow speed, velocity with respect to V^*_{Ref}, density with respect to a reference density ρ^*_{Ref}, pressure with respect to $\rho^*_{\text{Ref}}(V^*_{\text{Ref}})^2$ and specific internal energy with respect to $(V^*_{\text{Ref}})^2$. Here, the superscript $*$ refers to a dimensional value of a flow variable. To allow convenient comparisons between the 3D LINFLUX solutions and those of previous 2D analyses, the reference length is taken here to be the blade chord at midspan; the reference fluid density and flow speed, to be the inlet freestream density and relative flow speed at midspan, respectively.

For aeroelastic and aeroacoustic applications, we are usually interested in a restricted class of unsteady flows; those in which the unsteady fluctuations can be regarded as perturbations of a background flow that is steady in a reference frame that rotates with the blade row. Moreover, the steady background flows far upstream (say $\xi \leq \xi_-$) and far downstream ($\xi \geq \xi_+$) from the blade row can be assumed to consist of at most a small steady perturbation from a fully-developed, axisymmetric, steady flow. The time-dependent or unsteady fluctuations in these flows arise from temporally and circumferentially periodic unsteady excitations of small-amplitude, i.e., prescribed vibratory blade motions and prescribed aerodynamic disturbances at inlet and exit that travel towards the blade row.

For example, if the blades vibrate at reduced frequency, ω, as seen by an observer in the blade-row frame, and at constant interblade phase angle, σ, we can write

$$\mathcal{R}_{\mathrm{B}_n}(\bar{r}, \bar{\theta} + 2\pi n/N_B, \bar{\xi}, t) = \mathbf{T}_n Re\{\mathbf{R}_{\mathrm{B}}(\bar{r}, \bar{\theta}, \bar{\xi}) \exp[i(\omega t + n\sigma)]\}, \ \bar{\mathbf{x}} \text{ on } B \ . \qquad (2.1)$$

Here, $\mathcal{R}_{\mathrm{B}_n}$ is the displacement of a point on the nth moving blade surface from its mean position in the rotating frame; $\mathbf{T}_n$ is a rotation matrix, which relates a vector in the reference ($n = 0$) passage to its counterpart in the nth passage; $n = 0, 1, 2, \ldots, N_B - 1$ is a blade index; $Re\{\ \}$ denotes the real part of $\{\ \}$; $\mathbf{R}_{\mathrm{B}}$ is the complex amplitude of the reference ($n = 0$) blade displacement; and B refers to the mean position of the reference blade. The interblade phase angle, σ, in equation (2.1), is determined by the nodal diameter pattern of the vibratory blade motion, i.e., $\sigma = 2\pi N_{\mathrm{D}}/N_B$, where $|N_{\mathrm{D}}|$, the number of nodal diameters, is the integer count of the number of times a disturbance pattern repeats around the wheel. The sign of N_{D} is determined by the direction of rotation of the vibratory disturbance pattern. If this pattern travels in the negative θ-direction, $N_{\mathrm{D}} > 0$. Thus, for a rotor, if $N_D > 0$, the vibratory disturbance pattern travels in the direction of blade rotation.

The unsteady disturbances in the far upstream and far downstream regions are, in part, prescribed as a fluid dynamic excitation and, in part, depend upon the interaction between the fluid and the blading. Typically, an unsteady aerodynamic excitation is represented as a linear combination of fundamental disturbances that are harmonic in time, at temporal frequency ω, and in the circumferential direction, at circumferential angular wave number $\bar{m} = N_{\mathrm{D}} + mN_{\mathrm{B}}$, $m = 0, \pm 1, \pm 2, \ldots$. For example, if the underlying absolute mean flow is uniform, the pressure associated with a fundamental acoustic excitation is of the form

$$\tilde{p}_{\mathrm{A}}^{\pm}(r, \theta, \xi, t) = Re\{a^{\pm} p^{\mathrm{R},\pm}(r) \exp[\chi^{\pm}\xi + i(\bar{m}\theta + \omega t)]\}, \quad \xi \lesseqgtr \xi_{\mp} \ . \qquad (2.2)$$

Here, $\tilde{p}_{\mathrm{A}}^{\pm}(\mathbf{x}, t)$ describes an incident pressure disturbance, i.e., a pressure disturbance that travels towards the blade row from far upstream ($\xi \leq \xi_-$) or far downstream ($\xi \geq \xi_+$). The quantities ω, $\bar{m} = N_{\mathrm{D}} + mN_{\mathrm{B}}$ or $\sigma_m = 2\pi(N_D/N_B + m)$, and the disturbance amplitude, $a^{\pm}$, are prescribed; the radial mode shape, $p^{\mathrm{R},\pm}(r)$, and the axial exponential coefficient $\chi^{\pm} = \beta^{\pm} + i\kappa_{\xi}^{\pm}$, where β is the axial attenuation coefficient and κ_{ξ} is the axial wave number, are determined from the equations that govern the unsteady fluid motion in the far field.

3. Unsteady Aerodynamic Formulations

Nonlinear equations that govern the unsteady flows, described in §2, are derived from the conservation laws for mass, momentum and energy and the thermodynamic relations for a perfect gas. Consider an arbitrary moving control volume, $\mathcal{V}(t)$, which is bounded by the control surface $\mathcal{A}(\mathbf{x},t)=0$. The conservation laws for the fluid within $\mathcal{V}$ at time t, referenced to a coordinate frame that rotates with the blade row at constant angular velocity $\mathbf{\Omega}$, can be written in the form

$$\frac{d}{dt}\int_{\mathcal{V}}\tilde{\mathbf{U}}d\mathcal{V}+\int_{\mathcal{A}}[\tilde{\mathbf{F}}_{x_j}-\tilde{\mathbf{U}}\dot{\mathcal{R}}_{x_j}]n_{x_j}d\mathcal{A}=\int_{\mathcal{V}}\tilde{\mathbf{S}}d\mathcal{V}\ . \tag{3.1}$$

Here, the symbol $\tilde{}$ indicates an unsteady flow quantity, $\dot{\mathcal{R}}=(\dot{\mathcal{R}}_{x_1},\ \dot{\mathcal{R}}_{x_2},\ \dot{\mathcal{R}}_{x_3})$ is the velocity of a moving field point, at say $\mathbf{x}=\bar{\mathbf{x}}+\mathcal{R}(\bar{\mathbf{x}},t)$, $\mathbf{n}$ is a unit normal vector pointing outward from the surface, $\mathcal{A}$, and a summation over repeated indices is implied. The displacement field $\mathcal{R}$ is prescribed, and the source term on the right-hand-side of (3.1) accounts for the rotation of the reference coordinate frame. The latter is equal to zero if the blade row is stationary.

The state, $\tilde{\mathbf{U}}$, flux, $\tilde{\mathbf{F}}_{x_j}, j=1,2,3$, and source term, $\tilde{\mathbf{S}}$, vectors in equation (3.1) are defined by

$$\tilde{\mathbf{U}}=\begin{bmatrix}\tilde{\bar{\rho}}\\ \tilde{\bar{\rho}}\tilde{V}_{x_1}\\ \tilde{\bar{\rho}}\tilde{V}_{x_2}\\ \tilde{\bar{\rho}}\tilde{V}_{x_3}\\ \tilde{\bar{\rho}}\tilde{E}_T\end{bmatrix}\ ,\ \tilde{\mathbf{F}}_{x_j}(\tilde{\mathbf{U}})=\begin{bmatrix}\tilde{U}_{j+1}\\ \tilde{U}_{j+1}\tilde{U}_2/\tilde{U}_1+\tilde{P}\delta_{1j}\\ \tilde{U}_{j+1}\tilde{U}_3/\tilde{U}_1+\tilde{P}\delta_{2j}\\ \tilde{U}_{j+1}\tilde{U}_4/\tilde{U}_1+\tilde{P}\delta_{3j}\\ \tilde{U}_{j+1}(\tilde{U}_5+\tilde{P})/\tilde{U}_1\end{bmatrix}\ ,\ \tilde{\mathbf{S}}(\tilde{\mathbf{U}},\mathbf{x})=\begin{bmatrix}0\\ 0\\ \Omega^2\tilde{U}_1x_2+2\Omega\tilde{U}_4\\ \Omega^2\tilde{U}_1x_3-2\Omega\tilde{U}_3\\ \Omega^2(\tilde{U}_3x_2+U_4x_3)\end{bmatrix}\ . \tag{3.2}$$

Here $\tilde{\bar{\rho}}$, $\tilde{\mathbf{V}}$, $\tilde{E}_T=\tilde{E}+\tilde{V}^2/2$ and $\tilde{P}=(\gamma-1)\tilde{\bar{\rho}}\tilde{E}=(\gamma-1)[\tilde{U}_5-\tilde{U}_1^{-1}(\tilde{U}_2^2+\tilde{U}_3^2+\tilde{U}_4^2)/2]$ are the time-dependent fluid density, velocity, specific total internal energy, and pressure, respectively. The velocity and total internal energy are measured relative to the blade-row frame of reference.

Local Field Equations

After interchanging the order of time differentiation and volume integration in equation (3.1), converting the surface integral to a volume integral, and taking the limit of the resulting volume integrals as $\mathcal{V}(t)\to 0$, we arrive at a differential equation, i.e.,

$$\partial\tilde{\mathbf{U}}/\partial t\Big|_{\mathbf{x}}+\partial\tilde{\mathbf{F}}_{x_j}/\partial x_j=\tilde{\mathbf{S}}\ , \tag{3.3}$$

that governs the inviscid fluid motion at the field points, $\mathbf{x}$, within the fluid domain, at which this motion is continuous and differentiable. In addition, if we choose a volume that contains a surface at which the fluid variables are discontinuous, and take the limits of the terms in (3.1) as this volume collapses into the surface of discontinuity, we determine jump conditions, i.e.,

$$[\mathbf{F}_{x_j}-\tilde{\mathbf{U}}\dot{\mathcal{R}}_{x_j}]n_{x_j}=0\quad\text{for}\quad\mathbf{x}\in\mathcal{W}_n\quad\text{or}\quad\mathbf{x}\in\mathcal{S}h_n\ , \tag{3.4}$$

that apply at vortex-sheet wakes, $\mathcal{W}_n$, and at shocks, Sh_n. Here $[\![\ ]\!]$ denotes the jump in a flow quantity across a surface of discontinuity and $\dot{\mathcal{R}}$ is the surface velocity. In principle, jump conditions should be imposed explicitly in unsteady fluid dynamic calculations, but, because of the associated difficulties, the usual procedure is to solve conservative forms of the governing equations, e.g., (3.1) or (3.3), over the entire fluid domain and apply special discretization techniques in an attempt to "capture" wake and shock phenomena.

We will also require a form of the field equation (3.3), that applies at fixed locations ($\dot{\mathcal{R}} \equiv \mathbf{0}$) in the blade-row frame, to describe the unsteady flow in the regions far upstream ($\xi < \xi_-$) and far downstream ($\xi > \xi_+$) of the blading. Expressed in terms of cylindrical coordinates, this equation has the form

$$\left.\frac{\partial \tilde{\mathbf{U}}^{\mathrm{cyl}}}{\partial t}\right|_{\mathbf{x}} + r^{-1}\frac{\partial r\tilde{\mathbf{F}}_r}{\partial r} + r^{-1}\frac{\partial \tilde{\mathbf{F}}_\theta}{\partial \theta} + \frac{\partial \tilde{\mathbf{F}}_\xi}{\partial \xi} = \tilde{\mathbf{S}}\ , \tag{3.5}$$

where $\mathbf{x} = \bar{\mathbf{x}}$, and the state and source-term vectors are given by

$$\tilde{\mathbf{U}}^{\mathrm{cyl}} = \begin{Bmatrix} \tilde{\bar{\rho}} \\ \tilde{\bar{\rho}}\tilde{V}_r \\ \tilde{\bar{\rho}}\tilde{V}_\theta \\ \tilde{\bar{\rho}}\tilde{V}_\xi \\ \tilde{\bar{\rho}}\tilde{E}_T \end{Bmatrix}, \qquad \tilde{\mathbf{S}} = r^{-1}\begin{Bmatrix} 0 \\ (\tilde{U}_3^{\mathrm{cyl}})^2/\tilde{U}_1^{\mathrm{cyl}} + \tilde{P} \\ -\tilde{U}_2^{\mathrm{cyl}}\tilde{U}_3^{\mathrm{cyl}}/\tilde{U}_1^{\mathrm{cyl}} \\ 0 \\ 0 \end{Bmatrix} + \Omega\begin{Bmatrix} 0 \\ 2\tilde{U}_3^{\mathrm{cyl}} + \tilde{U}_1^{\mathrm{cyl}}\Omega r \\ -2\tilde{U}_2^{\mathrm{cyl}} \\ 0 \\ \tilde{U}_2^{\mathrm{cyl}}\Omega r \end{Bmatrix}. \tag{3.6}$$

The flux vectors $\tilde{\mathbf{F}}_r(\tilde{\mathbf{U}}^{\mathrm{cyl}})$, $\tilde{\mathbf{F}}_\theta(\tilde{\mathbf{U}}^{\mathrm{cyl}})$ and $\tilde{\mathbf{F}}_\xi(\tilde{\mathbf{U}}^{\mathrm{cyl}})$ and the pressure $P(\tilde{\mathbf{U}}^{\mathrm{cyl}})$ have functional forms similar to those indicated previously for $\tilde{\mathbf{F}}_{x_j}(\tilde{\mathbf{U}})$, $j = 1, 2, 3$, and $\tilde{P}(\tilde{\mathbf{U}})$.

Boundary Conditions

The foregoing field equations must be supplemented by conditions on the unsteady flow at blade surfaces, duct walls, and at the inflow ($\xi = \xi_-$) and outflow ($\xi = \xi_+$) boundaries of the near-field computational domain. Flow tangency conditions, i.e.,

$$(\tilde{\mathbf{V}} - \dot{\mathcal{R}}) \cdot \mathbf{n} = 0 \quad \text{for} \quad \mathbf{x} \in \mathcal{B}_n\ , \quad r = r_H \quad \text{and} \quad r = r_D\ , \tag{3.7}$$

apply at the moving blade surfaces, $\mathcal{B}_n$, and at the stationary ($\dot{\mathcal{R}} \equiv \mathbf{0}$) duct walls. In addition, temporally- and circumferentially-averaged values of the total pressure, the total temperature and the inlet flow angle are specified as functions of radius at the computational inflow boundary, and the circumferentially- and temporally-averaged static pressure is specified at the outflow boundary, consistent with radial equilibrium. The unsteady fluctuations at inlet and exit that carry energy towards the blade row must also be specified; those that carry energy away from the blade row must be determined as part of the unsteady solution.

3.1 Linearized Unsteady Aerodynamic Model

Since the unsteady excitations are assumed to be of small amplitude (e.g., $|\mathcal{R}_{B_n}| \sim \mathcal{O}(\epsilon) << 1$) and to occur at a single temporal frequency, ω, in the rotating frame, the unsteady component of the inviscid flow can be approximated as a first-order (in ϵ), harmonic

perturbation of an underlying zeroth-order, nonlinear, background flow that is steady in the blade-row frame. This approximation offers several computational advantages. First, since the first-order unsteady flow properties have harmonic time-dependence, physical time dependence can be removed from the unsteady boundary value problem. Second, as a consequence of our assumptions regarding rotor geometry, inlet and exit mean-flow conditions, and the circumferential behaviors of the unsteady excitations, numerical resolutions of the steady and linearized unsteady flows can be limited to a single, extended, blade-passage region, i.e., a region of angular pitch $\Delta\theta = 2\pi/N_B$. Finally, solutions for the unsteady perturbations of fully-developed, axisymmetric, steady background flows can be constructed and matched to a computational near-field solution to limit the axial extent of the computational domain.

To determine the linearized unsteady aerodynamic equations, we expand the unsteady state vector, $\tilde{\mathbf{U}}$, into an asymptotic series of the form [HC93a]

$$\tilde{\mathbf{U}}[\mathbf{x}(\bar{\mathbf{x}},t),t] = \mathbf{U}(\bar{\mathbf{x}}) + \tilde{\mathbf{u}}[\mathbf{x}(\bar{\mathbf{x}},t),t] + \ldots = \mathbf{U}(\bar{\mathbf{x}}) + Re\{\mathbf{u}(\bar{\mathbf{x}})\exp(i\omega t)\} + \ldots \,, \tag{3.8}$$

where the column vectors $\mathbf{U}(\bar{\mathbf{x}})$ and $\tilde{\mathbf{u}}[\mathbf{x}(\bar{\mathbf{x}},t),t]$ contain the conservation variables for the steady background flow at the mean position, $\bar{\mathbf{x}}$, and the first-order unsteady flow at the instantaneous position, $\mathbf{x} = \bar{\mathbf{x}} + \boldsymbol{\mathcal{R}}(\bar{\mathbf{x}},t) = \bar{\mathbf{x}} + \mathrm{Re}\{\mathbf{R}(\bar{\mathbf{x}})\exp(i\omega t)\}$, of a moving field point, respectively, and the dots refer to higher order terms. The components of the vector $\mathbf{u}$ are the complex amplitudes of the first-order unsteady conservation variables, i.e., $\mathbf{u}^T = [\rho\,,\ \bar{\rho}v_{x_1}+\rho V_{x_1}\,,\ \bar{\rho}v_{x_2}+\rho V_{x_2}\,,\ \bar{\rho}v_{x_3}+\rho V_{x_3}\,,\ \bar{\rho}e_T+\rho E_T]$ where $\bar{\rho}$, $\mathbf{V}$ and E_T and ρ, $\mathbf{v}$, and e_T are the steady and the complex amplitudes of the first-order unsteady, primitive, flow variables, respectively. The unsteady flux, $\tilde{\mathbf{F}}_{x_j}$, and source term, $\tilde{\mathbf{S}}$, vectors are approximated using Taylor series expansions about the mean flow state, $\mathbf{U}$, and the reference spatial location, $\bar{\mathbf{x}}$, i.e.,

$$\tilde{\mathbf{F}}_{x_j}(\tilde{\mathbf{U}}) = \mathbf{F}_{x_j}(\mathbf{U}) + \frac{\partial \mathbf{F}_{x_j}}{\partial \mathbf{U}}\tilde{\mathbf{u}} + \ldots \quad \text{and} \quad \tilde{\mathbf{S}}(\tilde{\mathbf{U}},\mathbf{x}) = \mathbf{S}(\mathbf{U},\bar{\mathbf{x}}) + \frac{\partial \mathbf{S}}{\partial \mathbf{U}}\tilde{\mathbf{u}} + (\boldsymbol{\mathcal{R}}\cdot\boldsymbol{\nabla}_{\bar{\mathbf{x}}})\mathbf{S} + \ldots \,, \tag{3.9}$$

where, $\partial\mathbf{F}_{x_j}/\partial\mathbf{U}$ and $\partial\mathbf{S}/\partial\mathbf{U}$ are flux and source-term Jacobian matrices, respectively.

The integral equations (3.1) have been expressed in terms of the moving control volume, $\mathcal{V}$, and the moving control surface, $\mathcal{A}$; the corresponding differential equations (3.3), in terms of the moving spatial coordinate $\mathbf{x}$. However, because of the dependent variable expansion (3.8), it is more appropriate to express the corresponding steady and linearized unsteady equations in terms of the mean or steady-state values, $\bar{V}$, $\bar{A}$, and $\bar{\mathbf{x}}$ of $\mathcal{V}$, $\mathcal{A}$, and $\mathbf{x}$ respectively. To within first-order in ϵ, the required spatial transformation relations are

$$d\mathcal{V} = (1 + \boldsymbol{\nabla}_{\bar{\mathbf{x}}}\cdot\boldsymbol{\mathcal{R}})d\bar{V} + \ldots \,, \quad \mathbf{n}d\mathcal{A} = \bar{\mathbf{n}}d\bar{A} + \Delta(\bar{\mathbf{n}}d\bar{A})\exp(i\omega t) + \ldots \,,$$
$$\text{and} \tag{3.10}$$
$$\partial\,/\partial x_j = \partial\,/\partial\bar{x}_j - (\partial\mathcal{R}_{x_m}/\partial\bar{x}_j)\partial\,/\partial\bar{x}_m + \ldots$$

where $(\boldsymbol{\nabla}_{\bar{\mathbf{x}}}\cdot\boldsymbol{\mathcal{R}}) = \partial\mathcal{R}_m/\partial\bar{x}_m$, $\bar{\mathbf{n}}$ is the unit outward normal vector to the control surface $\bar{A}$, and $\Delta(\bar{\mathbf{n}}d\bar{A})$ is the complex amplitude of the first-harmonic component of $\mathbf{n}d\mathcal{A} - \bar{\mathbf{n}}d\bar{A}$. Finally, to within first order in ϵ, the temporal derivative terms in equations (3.1) and (3.3) transform according to

$$\frac{d}{dt}\int_{\bar{\mathcal{V}}}(\quad)d\mathcal{V} = \int_{\bar{\mathcal{V}}}\left(\left.\frac{\partial(\quad)}{\partial t}\right|_{\bar{\mathbf{x}}} + (\quad)\boldsymbol{\nabla}_{\bar{\mathbf{x}}}\cdot\dot{\boldsymbol{\mathcal{R}}}\right)d\bar{V} + \ldots \quad \text{and} \quad \left.\frac{\partial}{\partial t}\right|_{\mathbf{x}} = \left.\frac{\partial}{\partial t}\right|_{\bar{\mathbf{x}}} + \dot{\mathcal{R}}_{x_m}\frac{\partial}{\partial\bar{x}_m} + \ldots \tag{3.11}$$

The equations that govern the zeroth-order steady and the first-order unsteady flows are obtained by substituting the foregoing series expansions into the nonlinear governing equations; equating terms of like power in ϵ; and neglecting terms of second and higher order in ϵ. This procedure leads to nonlinear and linear variable-coefficient equations, respectively, for the zeroth- and first-order flows. The variable coefficients in the linear equations depend upon the underlying steady background flow.

The conservation equation for the steady background flow is

$$\int_{\bar{A}} \mathbf{F}_{x_j} n_{x_j} d\bar{A} = \int_{\bar{V}} \mathbf{S} d\bar{V} \quad \text{or} \quad \partial \mathbf{F}_{x_j} / \partial \bar{x}_j = \mathbf{S} \ . \tag{3.12}$$

In addition, the flow tangency conditions,

$$\mathbf{V} \cdot \mathbf{n} = 0 \ , \quad \text{for} \quad \bar{\mathbf{x}} \in B_n \ , \ r = r_H \text{ and } r = r_D \tag{3.13}$$

apply at the reference blade surfaces and at the duct walls, and periodic conditions on the steady flow variables; e.g.,

$$\bar{\rho}(\bar{r}, \bar{\theta} + 2\pi n/N_B, \bar{\xi}) = \bar{\rho}(\bar{r}, \bar{\theta}, \bar{\xi}) \quad \text{and} \quad \mathbf{V}(\bar{r}, \bar{\theta} + 2\pi n/N_B, \bar{\xi}) = \mathbf{T}_n \mathbf{V}(\bar{r}, \bar{\theta}, \bar{\xi}) \tag{3.14}$$

apply upstream and downstream of the blade row. Finally, circumferentially averaged values of the appropriate steady flow variables are specified as functions of radius at the inflow and outflow boundaries and circumferential harmonics of these variables are allowed to evolve to values that are consistent with a blade row operating within a long annular duct.

The conservation equation that governs the first-harmonic unsteady perturbation is

$$\begin{aligned} i\omega \int_{\bar{V}} \mathbf{u} d\bar{V} + \int_{\bar{A}} \left(\frac{\partial \mathbf{F}_{x_j}}{\partial \mathbf{U}} \mathbf{u} \right) \bar{n}_{x_j} d\bar{A} - \int_{\bar{V}} \frac{\partial \mathbf{S}}{\partial \mathbf{U}} \mathbf{u} d\bar{V} = - \int_{\bar{V}} i\omega \left(\frac{\partial R_{x_m}}{\partial \bar{x}_m} \right) \mathbf{U} d\bar{V} \\ + \int_{\bar{A}} \left[i\omega R_{x_j} \mathbf{U} \bar{n}_{x_j} d\bar{A} - \mathbf{F}_{x_j} \Delta(\bar{\mathbf{n}} d\bar{A}) \right] + \int_{\bar{V}} \frac{\partial}{\partial \bar{x}_j} (R_{x_j} \mathbf{S}) d\bar{V} \ , \end{aligned} \tag{3.15a}$$

or

$$\begin{aligned} i\omega \mathbf{u} \ + \ \frac{\partial}{\partial \bar{x}_j} \left(\frac{\partial \mathbf{F}_{x_j}}{\partial \mathbf{U}} \mathbf{u} \right) - \frac{\partial \mathbf{S}}{\partial \mathbf{U}} \mathbf{u} = -i\omega \frac{\partial R_{x_m}}{\partial \bar{x}_m} \mathbf{U} \\ + \ \frac{\partial}{\partial \bar{x}_j} \left[i\omega R_{x_j} \mathbf{U} + \frac{\partial R_{x_j}}{\partial \bar{x}_m} \mathbf{F}_{x_m} - \frac{\partial R_{x_m}}{\partial \bar{x}_m} \mathbf{F}_{x_j} \right] + \frac{\partial}{\partial \bar{x}_j} (R_{x_j} \mathbf{S}) \ , \end{aligned} \tag{3.15b}$$

respectively, where the terms on the right-hand side, which depend on the steady flow quantities and the prescribed displacement field, $\mathbf{R}$, are regarded as known source terms.

Linearized flow tangency conditions, i.e.,

$$\mathbf{v} \cdot \bar{\mathbf{n}} = i\omega \mathbf{R} \cdot \bar{\mathbf{n}} + \mathbf{V} \cdot \boldsymbol{\nabla}(\mathbf{R} \cdot \bar{\mathbf{n}}), \text{ for } \bar{\mathbf{x}} \in B_n \ , \ r = r_H \text{ and } r = r_D \ , \tag{3.16}$$

apply at the mean blade surfaces and at the duct walls, and phase-shifted periodicity conditions, e.g.,

$$\rho(\bar{r}, \bar{\theta} + 2\pi n/N_B \ , \xi) = \rho(\bar{r}, \bar{\theta}, \bar{\xi}) \exp(in\sigma) \quad \text{and} \quad \mathbf{v}(\bar{r}, \bar{\theta} + 2\pi n/N_B, \bar{\xi}) = \mathbf{T}_n \mathbf{v}(\bar{r}, \bar{\theta}, \bar{\xi}) \exp(in\sigma) \ , \tag{3.17}$$

apply upstream and downstream of the blade row. The far-field conditions imposed in the unsteady problem must allow for the prescription of external unsteady aerodynamic excitations and permit unsteady disturbances coming from within the solution domain to pass through the computational inlet (at $\xi = \xi_-$) and exit (at $\xi = \xi_+$) boundaries without reflection.

Differential field equations that describe the steady and the first-order unsteady flows at fixed points, $\mathbf{x} = \bar{\mathbf{x}}$, in the far upstream ($\xi < \xi_-$) or far downstream ($\xi > \xi_+$) regions, can be determined by transforming the differential equations in (3.12) and (3.15) to cylindrical coordinates, or, alternatively, by applying the series expansions (3.8) and (3.9) to the nonlinear, time-dependent equation (3.5), and setting $\mathbf{R} \equiv \mathbf{0}$. We find that

$$r^{-1}\frac{\partial r\mathbf{F}_r}{\partial r} + r^{-1}\frac{\partial \mathbf{F}_\theta}{\partial \theta} + \frac{\partial \mathbf{F}_\xi}{\partial \xi} = \mathbf{S} \tag{3.18}$$

and

$$i\omega\mathbf{u} + r^{-1}\frac{\partial(r\mathbf{A}\mathbf{u})}{\partial r} + r^{-1}\frac{\partial \mathbf{B}\mathbf{u}}{\partial \theta} + \frac{\partial \mathbf{C}\mathbf{u}}{\partial \xi} - \mathbf{D}\mathbf{u} = 0\ , \tag{3.19}$$

where $\mathbf{A} = \partial\mathbf{F}_r\ /\partial\mathbf{U}^{\text{cyl}}$, $\mathbf{B} = \partial\mathbf{F}_\theta\ /\partial\mathbf{U}^{\text{cyl}}$ and $\mathbf{C} = \partial\mathbf{F}_\xi\ /\partial\mathbf{U}^{\text{cyl}}$ are flux Jacobian matrices and $\mathbf{D} = \partial\mathbf{S}\ /\partial\mathbf{U}^{\text{cyl}}$ is the source-term Jacobian matrix.

3.2 Solution Strategy

To predict the unsteady aerodynamic response of a blade row to a prescribed unsteady excitation, we require sequential solutions to the foregoing nonlinear steady and linearized unsteady boundary value problems. In the present study, we shall employ the nonlinear analysis, TURBO [JHW92], to determine the steady background flow, and then seek solutions to the linearized unsteady problem by matching a wave-split, finite-volume analysis for the unsteady perturbation in the near field, i.e., in the region $\xi_- \le \xi \le \xi_+$, to approximate analytic/numeric descriptions for the unsteady perturbations of the fully-developed, axisymmetric, steady background flows that exist in the regions far upstream ($\xi \le \xi_-$) and far downstream ($\xi \ge \xi_+$) of the blade row.

For the near-field, finite-volume analysis, it is advantageous to regard the state vector $\mathbf{u}$ as pseudo time dependent, i.e., to set $\mathbf{u} = \mathbf{u}(\bar{\mathbf{x}}, \tau)$, where τ is the pseudo time variable, and add the term $\partial(\int_{\bar{V}} \mathbf{u} d\bar{V})/\partial\tau$ to the left-hand side of equation (3.15a). This allows conventional time-marching algorithms to be used to converge the solution for the complex amplitude of the unsteady state vector to a steady-state value.

The complex-amplitude of the displacement field, $\mathbf{R}(\bar{\mathbf{x}})$, must be prescribed over the entire solution domain. This field is defined so that the solution domain deforms with the blade motion (i.e., $\mathbf{R}(\bar{\mathbf{x}}) = \mathbf{R}_{\mathrm{B}_n}(\bar{\mathbf{x}})$ for $\bar{\mathbf{x}} \in \mathrm{B}_n$), slides along the hub and duct walls ($\mathbf{R}(\bar{\mathbf{x}}) \cdot \mathbf{e}_r = 0$ for $\bar{r} = r_H, r_D$), and remains rigid far from the blade row ($\mathbf{R}(\bar{\mathbf{x}}) \equiv \mathbf{0}$ for $\bar{\xi} \lesseqgtr \bar{\xi}_{\mp}$). In addition, $\mathbf{R}(\bar{\mathbf{x}})$ is prescribed along one blade-to-blade periodic boundary, and set at the other boundary, so as to satisfy phase-lagged periodicity, cf. (3.17). In the near field, $\mathbf{R}(\bar{\mathbf{x}})$ is determined, first, along the hub and duct walls, and then, in the interior of the computational domain as solutions of Laplace's equation, $\nabla^2_{\bar{\mathbf{x}}}\mathbf{R} = \mathbf{0}$, subject to the appropriate Dirichlet boundary conditions. For unsteady flows in which the blades are stationary in the blade-row frame, $\mathbf{R}$ is simply set equal to zero.

4. Near-Field Numerical Model

The numerical procedures used in LINFLUX to resolve the linearized unsteady flow in the near field are based on those employed in the nonlinear analysis, TURBO [Jan89, JHW92, CW93]. TURBO is applied in the present study to determine steady background flows. Both analyses use sheared H-meshes [BH92, SS91] which define a curvilinear coordinate system, such that there is a one-to-one correspondence between the points, $\bar{\mathbf{x}}$, in the physical domain and the points, $\boldsymbol{\alpha}$, in a rectangular computational domain, where the grid is uniform and orthogonal. The α_1, α_2 and α_3 computational coordinates, or the I, J, K computational mesh indices, correspond, generally to the axial, radial and circumferential directions, respectively. Cell faces are surfaces of constant computational coordinate, with each cell bounded by the six surfaces: $\alpha_1 = I \mp 1/2$, $\alpha_2 = J \mp 1/2$ and $\alpha_3 = K \mp 1/2$.

4.1 Finite Volume Equations

If we let the symbol $\hat{}$ refer to a quantity expressed in terms of cell geometry, then a finite-volume spatial discretization of the pseudo time dependent form of the linearized unsteady equation (3.15a) can be written as

$$\frac{\partial \hat{\mathbf{u}}}{\partial \tau} = -i\omega\hat{\mathbf{u}} - \delta_j \hat{\mathbf{f}}_j + \frac{\partial \mathbf{S}}{\partial \mathbf{U}}\hat{\mathbf{u}} - i\omega(\Delta\vartheta)\mathbf{U} - \delta_j \hat{\mathbf{f}}_j^d + (\Delta\vartheta)\mathbf{S} + \bar{\vartheta}(\mathbf{R}\cdot\nabla_{\bar{\mathbf{x}}})\mathbf{S} = -\hat{\mathbf{r}} \qquad (4.1)$$

where $\hat{\mathbf{u}} = \bar{\vartheta}\mathbf{u}$, $\hat{\mathbf{f}}_j = (\partial\hat{\mathbf{F}}_j/\partial\mathbf{U})\mathbf{u} = \bar{A}_{jk}(\partial\mathbf{F}_k/\partial\mathbf{U})\mathbf{u} = \bar{A}_{jk}\mathbf{f}_k$, and $\hat{\mathbf{f}}_j^d = -\dot{\vartheta}_j\mathbf{U} + a_{jk}\mathbf{F}_k$. Here, the quantities $\mathbf{u}$, $\mathbf{U}$, and $\mathbf{S}$ represent average values of the physical state and source term vectors over a mean cell volume; $\bar{\vartheta}$ is the mean cell volume; $\bar{A}_{jk}$ is the mean area of a constant α_j cell face projected in the $\bar{x}_k$ direction; the vectors $\hat{\mathbf{F}}_j$ and $\hat{\mathbf{f}}_j$ are the steady and unsteady fluxes, respectively, across a constant α_j cell face; $\hat{\mathbf{f}}_j^d$ is the unsteady flux associated with the displacement field, $\mathbf{R}$; and $\hat{\mathbf{r}}$ is the residual of the first-harmonic unsteady equation. The steady quantities $\bar{\vartheta}$, $\bar{A}_{jk}$, $\mathbf{U}$, $\mathbf{F}_j(\mathbf{U})$ and $\mathbf{S}(\mathbf{U},\bar{\mathbf{x}})$ and the unsteady displacement field, $\mathbf{R}$, are regarded as known for the linearized unsteady analysis.

The operator δ_j in equation (4.1) denotes the difference in the j-direction across adjacent cell interfaces, and the repeated j index implies summation over all computational coordinate directions. Thus, the terms $\delta_j\hat{\mathbf{f}}_j$ and $\delta_j\hat{\mathbf{f}}_j^d$ are the net unsteady fluxes through a cell due to the unsteady fluid motion and the grid motion, respectively. The linearized perturbation equation contains source terms that are associated with changes in cell volume, cell face area, and cell radial location. These terms depend on known steady flow properties and on the prescribed displacement field, $\mathbf{R}(\bar{\mathbf{x}})$. In evaluating the volume terms $\Delta\vartheta = \delta_j(\bar{A}_{jk}R_{x_k})$ and $\dot{\vartheta}_j = i\omega\bar{A}_{jk}R_{x_k}$, the R_{x_k} are taken to be the average displacements over a cell face. The perturbations in the cell face areas, a_{jk}, and in cell location are computed using the displacements of the cell vertices.

The unsteady field equation must be solved subject to conditions at the boundaries of the near-field computational domain. Flow tangency conditions at the blade surfaces and the duct walls, cf. (3.16), are implemented using phantom cells inside a solid surface. The density and pressure in a phantom cell are defined by a first-order accurate reflection condition, and the phantom cell velocity is defined such that the velocity at the

solid surface, which is the average of the velocities in the phantom and the interior cells, satisfies the flow tangency condition, in a manner consistent with the finite volume discretization. The phase-shifted periodicity condition, cf. (3.17), is imposed along a passage boundary by taking advantage of grid periodicity in the blade-to-blade direction. Thus, we set $\mathbf{u}|_{I,J,K} = \mathbf{T}_{\pm 1}\mathbf{u}_{I,J,K\pm(NK-1)}\exp(\pm i\sigma)$ where NK denotes the number of blade-to-blade grid points, and the $\mathbf{T}_n$ matrix rotates the x_2 and x_3 components of the momentum vector through n blade passages. Finally, analytic/numeric far-field solutions are matched to the numerical near-field solution at the computational inflow and outflow boundaries ($\xi = \xi_{\mp}$).

After replacing the pseudo time derivative in (4.1) by a first-order accurate, two-point, backward, difference expression, and expanding the residual, $\hat{\mathbf{r}}^{n+1}$, about the nth time level, we can write the discretized unsteady field equation as

$$\left(\hat{\Theta}\mathbf{I} + \frac{\partial \hat{\mathbf{r}}}{\partial \mathbf{u}}\right)\Delta\mathbf{u}^n = -\hat{\mathbf{r}}^n \,, \tag{4.2}$$

or, after making the appropriate substitutions, as

$$\left(\hat{\Theta} + i\omega\bar{\vartheta} - \bar{\vartheta}\frac{\partial \mathbf{S}}{\partial \mathbf{U}}\right)\Delta\mathbf{u}^n + \delta_j\left(\frac{\partial \hat{\mathbf{F}}_j}{\partial \mathbf{U}}\Delta\mathbf{u}^n\right) = -\bar{\vartheta}\left(i\omega - \frac{\partial \mathbf{S}}{\partial \mathbf{U}}\right)\mathbf{u}^n - (\delta_j\hat{\mathbf{f}}_j)^n + \mathbf{s}^n = -\hat{\mathbf{r}}^n \,, \tag{4.3}$$

where $\mathbf{s}$ is the grid deformation source term. In equations (4.2) and (4.3), the superscript n refers to the nth pseudo time level, $\hat{\Theta} = \bar{\vartheta}/\Delta\tau$, $\Delta\mathbf{u}^n = \mathbf{u}^{n+1} - \mathbf{u}^n$, $\hat{\mathbf{r}}$ is defined as in (4.1), and $\partial\hat{\mathbf{r}}/\partial\mathbf{u}$ is a constant, since the unsteady residual is a linear function of the state vector $\mathbf{u}$.

4.2 Evaluation of Flux Terms and Pseudo-Time Integration

To simplify the descriptions of the spatial discretizations that are used to approximate the flux terms in equation (4.3), and the pseudo-time integration that is used to solve this equation, we will consider a "one-dimensional flow" in which $\hat{\mathbf{F}}_j = \hat{\mathbf{F}}$ and $\hat{\mathbf{f}}_j = \hat{\mathbf{f}}$ are the steady and unsteady flux vectors in the $\alpha_j = \alpha$ coordinate direction. The subscript J refers to the cell volume bounded by the cell surfaces at $\alpha = J + 1/2$ and $\alpha = J - 1/2$. Extensions of the equations that follow to three-dimensional flows is straightforward conceptually, but involves the use of tedious additional nomenclature.

Flux difference splitting is applied to evaluate the flux terms on the left- and right-hand sides of (4.3). The flux splitting, i.e.,

$$\hat{\mathbf{f}} = \frac{\partial \hat{\mathbf{F}}}{\partial \mathbf{U}}\mathbf{u} = \left(\frac{\partial \hat{\mathbf{F}}}{\partial \mathbf{U}}^{+} + \frac{\partial \hat{\mathbf{F}}}{\partial \mathbf{U}}^{-}\right)\mathbf{u} = \hat{\mathbf{T}}(\hat{\mathbf{\Lambda}}^{+} + \hat{\mathbf{\Lambda}}^{-})\hat{\mathbf{T}}^{-1}\mathbf{u} \,, \tag{4.4}$$

is based on a similarity transformation and an eigenvalue decomposition of the flux Jacobian matrix, $\partial\hat{\mathbf{F}}/\partial\mathbf{U}$, into matrices that account for right (+) and left (−) traveling disturbances. The matrices $\hat{\mathbf{T}}$ and $\hat{\mathbf{T}}^{-1}$ contain the right and left eigenvectors, respectively, of $\partial\hat{\mathbf{F}}/\partial\hat{\mathbf{U}}$, and $\hat{\mathbf{\Lambda}}^{+}$ and $\hat{\mathbf{\Lambda}}^{-}$ are diagonal matrices containing the positive (+) and negative (−) eigenvalues. The eigenvalues of the flux Jacobian matrix are used to determine which characteristic modes are taken into account, thus controlling the direction of spatial differencing.

We have chosen to evaluate the flux, $\hat{\mathbf{f}}_{J+1/2}$, at the $J+1/2$ cell interface in terms of the flux in the cell to the left (J) of the interface and the flux due to waves approaching the interface from the right. Thus, we set

$$\hat{\mathbf{f}}_{J+1/2} = \left(\frac{\partial \hat{\mathbf{F}}}{\partial \mathbf{U}}\mathbf{u}\right)_{J+1/2} \approx \hat{\mathbf{f}}(\mathbf{u}_J, \bar{A}_{J+1/2}) + \left.\frac{\partial \hat{\mathbf{F}}}{\partial \mathbf{U}}\right|^{-}_{\mathbf{U}^{\mathrm{Roe}}_{J+1/2}, \bar{A}_{J+1/2}} (\mathbf{u}_{J+1} - \mathbf{u}_J) \,, \tag{4.5}$$

where $\hat{\mathbf{f}}(\mathbf{u}_J, \bar{A}_{J+1/2})$ is a flux based on the state vector in the Jth cell and the mean area of the $J+1/2$ cell interface. The flux Jacobian matrix $\partial \hat{\mathbf{F}}/\partial \mathbf{U}|_{\mathbf{U}^{\mathrm{Roe}}_{J+1/2}, \bar{A}_{J+1/2}}$ is evaluated in terms of the Roe-averaged [Roe81] intermediate state vector $\mathbf{U}^{\mathrm{Roe}}_{J+1/2}$ and the area $\bar{A}_{J+1/2}$, where $\mathbf{U}^{\mathrm{Roe}}_{J+1/2}$, is defined using the relations:

$$\bar{\rho}^{\mathrm{Roe}}_{J+1/2} = \sqrt{\bar{\rho}_J \bar{\rho}_{J+1}} \,, \quad \mathbf{V}^{\mathrm{Roe}}_{J+1/2} = \frac{\sqrt{\bar{\rho}_J}\mathbf{V}_J + \sqrt{\bar{\rho}_{J+1}}\mathbf{V}_{J+1}}{\sqrt{\bar{\rho}_J} + \sqrt{\bar{\rho}_{J+1}}} \,,$$

and

$$E^{\mathrm{Roe}}_{T,J+1/2} = \frac{\sqrt{\bar{\rho}_J}E_{T,J} + \sqrt{\bar{\rho}_{J+1}}E_{T,J+1}}{\sqrt{\bar{\rho}_J} + \sqrt{\bar{\rho}_{J+1}}} \,. \tag{4.6}$$

The discrete approximation (4.5) is first-order accurate, since the interfacial fluxes are based only upon information from adjacent cells. Second order spatial accuracy can be achieved by introducing corrective fluxes, which bring in information from additional neighboring cells. In LINFLUX, the corrective perturbation flux at the $J+1/2$ interface is comprised of right traveling waves at the upstream interface ($J-1/2$) of the Jth cell and left traveling waves at the downstream interface ($J+3/2$) of the ($J+1$)th cell. These waves are approximated using the Roe-averaged flux Jacobian matrix at the $J+1/2$ interface. Thus, second order spatial accuracy is achieved by adding the terms

$$\frac{1}{2}\left.\frac{\partial \hat{\mathbf{F}}}{\partial \mathbf{U}}\right|^{+}_{\mathbf{u}^{\mathrm{Roe}}_{J+1/2}, \bar{A}_{J+1/2}} (\mathbf{u}_J - \mathbf{u}_{J-1}) \quad \text{and} \quad -\frac{1}{2}\left.\frac{\partial \hat{\mathbf{F}}}{\partial \mathbf{U}}\right|^{-}_{\mathbf{u}^{\mathrm{Roe}}_{J+1/2}, \bar{A}_{J+1/2}} (\mathbf{u}_{J+2} - \mathbf{u}_{J+1})$$

to the right-hand side of (4.5).

Once the interfacial fluxes have been computed, they are spatially differenced to compute the net flux terms that appear on the right- and left-hand sides of the unsteady equation (4.3). The difference expression for the net unsteady flux through the Jth control volume is

$$\delta \hat{\mathbf{f}}\Big|_J \approx \hat{\mathbf{f}}_{J+1/2} - \hat{\mathbf{f}}_{J-1/2} \,, \tag{4.7}$$

where the second-order discrete approximation is used in conjunction with (4.7) to evaluate the net unsteady flux term that appears on the right-hand side of (4.3). The left-hand side flux term, $\delta[(\partial \hat{\mathbf{F}}/\partial \mathbf{U})\Delta \mathbf{u}]\Big|_J$, i.e., the change in the net unsteady flux due to the pseudo time update, is evaluated using the first-order accurate approximation in (4.5).

The linearized unsteady equation (4.2) is discretized, as outlined above, leading to a system of linear algebraic equations. This system is solved, at each pseudo-time step, using

a symmetric Gauss-Seidel (SGS) iteration procedure in which the left-hand side matrix is decomposed into diagonal and off-diagonal submatrices. Thus, we set

$$\left(\hat{\Theta}_J \mathbf{I} + \left.\frac{\partial \hat{\mathbf{r}}}{\partial \mathbf{u}}\right|_{\mathbf{u}_J^n}\right) \Delta \mathbf{u}_J^n = \mathbf{D}_J \Delta \mathbf{u}_J^n - \mathbf{M}_{J-1}^{+} \Delta \mathbf{u}_{J-1}^n + \mathbf{M}_{J+1}^{-} \Delta \mathbf{u}_{J+1}^n = -\hat{\mathbf{r}}_J^n \ , \qquad (4.8)$$

where the $\mathbf{D}$ submatrix contains the diagonal elements of the original matrix, and the $\mathbf{M}^{+}$ and $\mathbf{M}^{-}$ submatrices contain the off-diagonal elements in the negative and positive computational coordinate directions, respectively.

The unsteady solutions to equation (4.8) are marched in pseudo-time until they converge to a steady state, i.e., $||\hat{\mathbf{r}}^n|| \rightarrow 0$. The current LINFLUX implementation uses explicit boundary conditions. These conditions are incorporated into the SGS iteration procedure, so that they are imposed in a semi-implicit manner. This treatment has been found to yield better convergence properties than a purely explicit implementation.

5. Unsteady Perturbations in the Far-Field

Analytical descriptions, based on reduced sets of governing equations, of the linearized unsteady flows in the regions far upstream ($\xi < \xi_-$) and far downstream ($\xi > \xi_+$) from a blade row can be applied to limit the axial extent of the near-field computational domain. In particular, approximate representations for the unsteady perturbations of fully-developed, axisymmetric, mean flows can be used to describe the behaviors of the convected and the modal type unsteady disturbances that exist in the far field. Such descriptions allow unsteady disturbances that enter the computational domain (excitations) to be prescribed as approximate solutions to the linearized governing equations, and by matching the far-field solutions to a numerical near-field solution, to render the computational inflow and outflow boundaries transparent or reflective, with specified coefficients, to outgoing waves.

We assume that, far from the blade row, the mean or steady flow quantities depend only on radius; i.e., $\bar{\rho} = \bar{\rho}(r)$, $P = P(r)$, etc., and that the radial component of the steady velocity is negligible; i.e., $\mathbf{V} = V_\theta(r)\mathbf{e}_\theta + V_\xi(r)\mathbf{e}_\xi$. Under these conditions, the steady field equation (3.18) reduces to

$$\bar{\rho}^{-1}\frac{dP}{dr} = r^{-1}V_\theta^2 + 2\Omega V_\theta + \Omega^2 r = r^{-1}(V_\theta^{\text{abs}})^2 \ . \tag{5.1}$$

After combining (5.1) with the thermodynamic relations $P\bar{\rho}^{-\gamma}\exp(-\gamma S) = C$, where C is a constant, and $E = \gamma^{-1}T = (\gamma-1)^{-1}P\bar{\rho}^{-1}$, we obtain the following equations to describe the radial behaviors of the mean-flow thermodynamic properties

$$\begin{aligned}\frac{\gamma}{\gamma-1}[C\exp(\gamma S)]^{1/\gamma}\,\frac{dP^{(\gamma-1)/\gamma}}{dr} &= \frac{\gamma}{\gamma-1}[C\exp(\gamma S)]\left[\frac{d\bar{\rho}^{\gamma-1}}{dr} + (\gamma-1)\bar{\rho}^{\gamma-1}\frac{dS}{dr}\right] \\ &= \frac{dT}{dr} - T\frac{dS}{dr} = r^{-1}V_\theta^2 + 2\Omega_x V_\theta + \Omega^2 r = r^{-1}(V_\theta^{\text{abs}})^2 \ .\end{aligned} \tag{5.2}$$

Certain kinematic and thermodynamic information must be specified to determine a fully-developed, axisymmetric, steady background flow. Typically, the absolute total temperature, $T_T^{\text{abs}} = T + (V^{\text{abs}})^2/2$, the absolute total pressure, $P_T^{\text{abs}} = P\left[(\gamma-1)A^{-2}T_T^{\text{abs}}\right]^{\frac{\gamma}{\gamma-1}}$, where $A^2 = \gamma P/\bar{\rho}$ is the sound speed, and the circumferential velocity, V_θ^{abs} or $V_\theta^{\text{rel}} = V_\theta$, are prescribed functions of radius. If, in addition, we assume that the mean-flow axial velocity and thermodynamic properties are known at some reference radial location, say $r = r_{\text{ref}}$, then the radial distribution of entropy can be determined from the relation

$$S = ln\left[\gamma^{-1}(\gamma-1)C^{-1/\gamma}T_T^{\text{abs}}/\left(P_T^{\text{abs}}\right)^{\frac{\gamma-1}{\gamma}}\right] \ , \tag{5.3}$$

and the radial distributions of the pressure, density and temperature can be determined from the relations given in (5.2). Moreover, the axial velocity, $V_\xi^{\text{abs}} = V_\xi$, is given by

$$V_\xi^{\text{abs}} = V_\xi = \left[2(T_T^{\text{abs}} - T) - (V_\theta^{\text{abs}})^2\right]^{1/2} \ . \tag{5.4}$$

For the mean flow conditions just described, the linearized unsteady equation (3.19) reduces to

$$i\omega\mathbf{u} + r^{-1}\frac{\partial(r\mathbf{A}_2\mathbf{u})}{\partial r} + r^{-1}\mathbf{B}_2\frac{\partial\mathbf{u}}{\partial\theta} + \mathbf{C}_2\frac{\partial\mathbf{u}}{\partial\xi} - \mathbf{D}\mathbf{u} = 0\ , \tag{5.5}$$

where the subscript 2 on the Jacobian matrices in (5.5) indicates that they are evaluated at $U_2^{\mathrm{cyl}} = \bar{\rho}V_r = 0$; e.g., $\mathbf{A}_2 \equiv \partial\mathbf{F}_r/\partial\mathbf{U}^{\mathrm{cyl}}|_{U_2^{\mathrm{cyl}}=0}$.

5.1 Uniform Mean Flow

For the special case of a uniform mean flow, in the absolute frame, exact solutions to equation (5.5) can be determined [VMK95]. Such solutions indicate that an arbitrary first-order, unsteady, aerodynamic perturbation can be represented as the sum of independent entropic, vortical and irrotational acoustic disturbances. The entropic and vortical disturbances are convected by the mean flow, and therefore, have general solutions of the form $\tilde{s} = \tilde{s}(r, r\theta - V_\theta t, \xi - V_\xi t)$ and $\tilde{\mathbf{v}}^{\mathrm{R}} = \tilde{\mathbf{v}}^{\mathrm{R}}(r, r\theta - V_\theta t, \xi - V_\xi t)$, where $\tilde{\mathbf{v}}^{\mathrm{R}}$ is the (rotational) velocity associated with the vorticity, $\tilde{\boldsymbol{\zeta}} = \boldsymbol{\nabla}\times\mathbf{v} = \boldsymbol{\nabla}\times\mathbf{v}^{\mathrm{R}}$. The acoustic disturbances are governed by a convected wave equation for the pressure, which can be solved analytically using the method of separation of variables [TS62, VTM82]. The state vector $\mathbf{u}$ that describes an unsteady perturbation of a uniform stream can thus be expressed in the form $\mathbf{u} = \mathbf{u}_C + \mathbf{u}_A$, where $\mathbf{u}_C$ describes convected entropic and vortical disturbances and $\mathbf{u}_A$ describes acoustic disturbances.

For an unsteady flow occurring at frequency ω, the state vector, $\mathbf{u}_C$, is a solution of the convection equation $\bar{D}\mathbf{u}_C/Dt = i\omega\mathbf{u}_C + \mathbf{V}\cdot\boldsymbol{\nabla}\mathbf{u}_C = 0$, of the form

$$\mathbf{u}_C = \sum_{m=-\infty}^{\infty}\mathbf{u}_m(r)\exp[i(\kappa_{\xi,m}\xi + \bar{m}\theta)]\ . \tag{5.6}$$

Here, the $\mathbf{u}_m$ are arbitrary functions of radius; $\kappa_{\xi,m} = -(\omega - \bar{m}\Omega)V_\xi^{-1} = -\omega_m^{\mathrm{abs}}V_\xi^{-1}$ and $\bar{m} = N_{\mathrm{D}} + mN_B$ are constant axial linear and circumferential angular wave numbers, respectively; and $\omega_m^{\mathrm{abs}} = \omega - \bar{m}\Omega$ is the temporal frequency of the mth disturbance as seen by an observer stationed in the absolute frame.

The vectors $\mathbf{u}_m$ in (5.6) can be expressed in terms of the mth entropic, s_m, and rotational velocity, $\mathbf{v}_{R,m}$, disturbances by setting $\rho_m = -\bar{\rho}s_m$, $\mathbf{v}_m = \mathbf{v}_m^{\mathrm{R}}$ and $e_{T,m} = \mathbf{V}\cdot\mathbf{v}_m^{\mathrm{R}} + s(E_T - V^2/2)$ to determine that

$$\mathbf{u}_m = \begin{bmatrix} \rho_m \\ \bar{\rho}v_{r,m} \\ \rho_m V_\theta + \bar{\rho}v_{\theta,m} \\ \rho_m V_\xi + \bar{\rho}v_{\xi,m} \\ \rho_m E_T + \bar{\rho}e_{T,m} \end{bmatrix} = \bar{\rho}s_m \begin{bmatrix} 1 \\ 0 \\ V_\theta \\ V_\xi \\ V^2/2 \end{bmatrix} + \bar{\rho}\mathbf{v}_m^{\mathrm{R}}\cdot\begin{bmatrix} 0 \\ \mathbf{e}_r \\ \mathbf{e}_\theta \\ \mathbf{e}_\xi \\ V_\theta\mathbf{e}_\theta + V_\xi\mathbf{e}_\xi \end{bmatrix}\ . \tag{5.7}$$

The first term on the right-hand side of equation (5.7) describes the state variable flucuations associated with the mth entropic disturbance; the second term, the fluctuations associated with the mth rotational velocity or vortical disturbance.

The analytic solution for the complex-amplitude of the unsteady pressure has the form

$$p = \sum_{m=-\infty}^{\infty} \exp(i\bar{m}\theta) \sum_{\mu=0}^{\infty} \left[a^{-}_{m\mu} \exp(\chi^{-}_{m\mu}\xi) + a^{+}_{m\mu} \exp(\chi^{+}_{m\mu}\xi) \right] E_{m\mu}(r) \ . \tag{5.8}$$

Here, the $a^{\mp}_{m\mu}$ are the complex amplitudes of upstream $(-)$ and downstream $(+)$ traveling pressure waves and the $E_{m\mu}(r) = J_{\bar{m}}(k_{m\mu}r) + Q_{m\mu}Y_{\bar{m}}(k_{m\mu}r)$ are the "characteristic E-functions" of [TS62]. The E-functions are combinations of Bessel functions, of order $\bar{m}$, of the first and second kinds. The constants $k_{m\mu}$ and $Q_{m\mu}$ are determined by the duct-wall boundary conditions, e.g., see (3.16), and the index $\mu = 0, 1, 2, \ldots$ indicates the number of zero crossings or nodes in the μth radial mode.

The axial exponential coefficients, $\chi^{\mp}_{m\mu}$, in equation (5.8) are given by

$$\chi^{\mp}_{m\mu} = \beta^{\mp}_{m\mu} + i\kappa^{\mp}_{\xi,m\mu} = (1 - M^2_{\xi})^{-1} \left[iM_{\xi}\omega^{\text{abs}}_{m}/A \pm [(1 - M^2_{\xi})k^2_{m\mu} - (\omega^{\text{abs}}_{m}/A)^2]^{1/2} \right] , \tag{5.9}$$

where $M_{\xi} = V_{\xi}/A < 1$ and A are the axial Mach number and speed of sound propagation in the steady background flow, respectively. If $(\omega^{\text{abs}}_{m})^2 > (1 - M^2_{\xi})A^2k^2_{m\mu}$, then the $\chi^{\mp}_{m\mu}$ are purely imaginary, and the $m\mu^{\text{th}}$ pressure patterns propagate. If the $\chi^{\mp}_{m\mu}$ are complex, then one pattern attenuates, and the other grows exponentially, with increasing axial distance. Each upstream and downstream traveling acoustic mode has a unique axial exponential coefficient, $\chi^{\mp}_{m\mu}$, except at an acoustic resonance condition, and thus a unique propagation/decay behavior and state vector.

The perturbation state vector for the irrotational acoustic disturbances is given by

$$\mathbf{u}_A = \sum_{m=-\infty}^{\infty} e^{i\bar{m}\theta} \sum_{\mu=0}^{\infty} \left[a^{-}_{m\mu}\mathbf{u}^{-}_{m\mu}(r) \exp\left(\chi^{-}_{m\mu}\xi\right) + a^{+}_{m\mu}\mathbf{u}^{+}_{m\mu}(r) \exp\left(\chi^{+}_{m\mu}\xi\right) \right] \ . \tag{5.10}$$

where the modal state vectors, $\mathbf{u}^{\mp}_{m\mu}(r)$, are determined, in terms of the modal pressure, $p^{\mp}_{m\mu}(r) = E_{m\mu}(r)$, from the linearized unsteady field equations. In particular, after carrying out the necessary algebra, we find that

$$\mathbf{u}^{\mp}_{m\mu} = \begin{bmatrix} \rho^{\mp}_{m\mu} \\ \bar{\rho}v^{\mp}_{r,m\mu} \\ \rho^{\mp}_{m\mu}V_{\theta} + \bar{\rho}v^{\mp}_{\theta,m\mu} \\ \rho^{\mp}_{m\mu}V_{\xi} + \bar{\rho}v^{\mp}_{\xi,m\mu} \\ \rho^{\mp}_{m\mu}E_T + \bar{\rho}e^{\mp}_{T,m\mu} \end{bmatrix} = \begin{bmatrix} A^{-2} \\ -(\lambda^{\mp}_{m\mu})^{-1}\partial/\partial r \\ A^{-2}V_{\theta} - i\bar{m}(\lambda^{\mp}_{m\mu})^{-1} \\ A^{-2}V_{\xi} - (\lambda^{\mp}_{m\mu})^{-1}\chi^{\mp}_{m\mu} \\ (\gamma - 1)^{-1}\left[1 + (\gamma - 1)M^2/2\right] \\ -(\lambda^{\mp}_{m\mu})^{-1}(i\bar{m}r^{-1}V_{\theta} + \chi^{\mp}_{m\mu}V_{\xi}) \end{bmatrix} p^{\mp}_{m\mu} \ , \tag{5.11}$$

where the $\lambda^{\mp}_{m\mu} = iw^{\text{abs}} + V_{\xi}\chi^{\mp}_{m\mu} = i(\omega - \bar{m}\Omega) + V_{\xi}\chi^{\mp}_{m\mu}$ are constants determined by the material derivative operator, $\bar{D}/Dt = i\omega + \mathbf{V} \cdot \boldsymbol{\nabla}$.

Note that, in addition to different axial behaviors, the convected disturbances in (5.6) and the acoustic disturbances in (5.10) have different radial behaviors. The radial dependence of the former can be specified arbitrarily, whereas that of the latter depends upon radial modes, which must be determined from the unsteady field equations.

5.2 Nonuniform Mean Flow

Guided by the exact solutions for uniform mean flows, approximate solutions to equation (5.5) can be constructed for the unsteady perturbations of nonuniform, fully-developed and axisymmetric, mean flows. For this purpose, we set $\mathbf{u} = \mathbf{u}_C + \mathbf{u}_W$, where $\mathbf{u}_C$, describes a convected disturbance field and $\mathbf{u}_W$ describes a series of modal disturbances. The convected disturbances are solutions of the unsteady equation (5.5) that satisfy the convection equation, $\bar{D}\mathbf{u}_C/Dt = \mathbf{0}$. Therefore, $\mathbf{u}_C$, has a solution of the form (5.6), i.e.,

$$\mathbf{u}_C = \sum_{m=-\infty}^{\infty} \mathbf{u}_m(r) \exp\{i[\kappa_{\xi,m}(r)\xi + \bar{m}\theta]\} \ , \tag{5.12}$$

but, in the present case, the axial wave number, $\kappa_{\xi,m}(r) = -[\omega + \bar{m}r^{-1}V_\theta(r)]/V_\xi(r) = -[\omega_m^{\text{abs}} + \bar{m}r^{-1}V_\theta^{\text{abs}}(r)]/V_\xi(r)$, depends on radius. The convected field may contain entropic and/or vortical disturbances, depending on the properties of the mean flow. However, for general nonisentropic, rotational mean flows no convected disturbance field will exist, because the entropic and vortical disturbances are coupled to the modal disturbances [Ker77]

The complex amplitude, $\mathbf{u}_W$, of the wave-type or modal disturbances is assumed to have the form

$$\mathbf{u}_W = \sum_{m=-\infty}^{\infty} \sum_{n=0}^{\infty} a_{mn} \mathbf{u}_{mn}^R(r) \exp(\chi_{mn}\xi + i\bar{m}\theta) \ , \tag{5.13}$$

where the terms on the right-hand-side are to be determined by solving of equation (5.5), subject to boundary conditions at the duct walls.

Far-Field Eigenanalysis

After substituting the assumed form of the solution for $\mathbf{u}_W$ (5.13) into the field equation (5.5) we determine the system of ordinary differential equations

$$i\omega\mathbf{I}\ \mathbf{u}_{mn}^R + r^{-1}\frac{d}{dr}\left(r\mathbf{A}_2\ \mathbf{u}_{mn}^R\right) + i\bar{m}r^{-1}\mathbf{B}_2\ \mathbf{u}_{mn}^R + \chi_{mn}\mathbf{C}_2\ \mathbf{u}_{mn}^R - \mathbf{D}_2\ \mathbf{u}_{mn}^R = \mathbf{0} \ , \tag{5.14}$$

which must be solved numerically. After discretizing equation (5.14), and applying the duct wall boundary conditions $v_r = 0$ at $r = r_H$ and $r = r_D$, we obtain the matrix equation

$$(\mathbf{P} - \chi_{mn}\mathbf{C}_2)\ \mathbf{u}_{mn}^R = \mathbf{0} \tag{5.15}$$

where $\mathbf{P} = -i\omega\mathbf{I} - \mathbf{L}(r, \mathbf{A}_2) - i\bar{m}r^{-1}\ \mathbf{B}_2 + \mathbf{D}_2$ and $\mathbf{L}(r, \mathbf{A}_2)$ is a finite difference approximation to $r^{-1}d(r\mathbf{A}_2\mathbf{u}_{mn}^R)/dr$. The column vector $\mathbf{u}_{mn}^R$ in equation (5.15) contains an entry for each of the five conservation variables at each radial discretization point.

Equation (5.15) can be solved, using a standard linear algebra routine, to determine the axial eigenvalues, χ_{mn}, and the associated right eigenvectors, $\mathbf{u}^R_{mn}(r)$, of the modal far-field disturbances. The left eigenvectors, $\mathbf{u}^L_{mn}$, are determined as a solution to the equation $(\mathbf{P} - \chi_{mn}\mathbf{C})^H \mathbf{u}^L_{mn} = \mathbf{0}$, where the superscript H denotes the conjugate transpose. An orthonormal set of left eigenvectors can then be obtained by setting $(\mathbf{v}^L_{mn})^H = (\mathbf{u}^L_{mn})^H \mathbf{C}/[(\mathbf{u}^L_{mn})^H \mathbf{C}\mathbf{u}^R_{mn}]$. Once the eigenvalues and the left and right eigenvectors of the system (5.14) have been computed, the complex amplitudes, a_{mn}, of the modal disturbances can be determined by taking inner products involving $\mathbf{v}^L_{mn}$ and $\mathbf{u}_W$; i.e.,

$$\begin{aligned} a_{mn} &= \langle \mathbf{v}^L_{mn}, \frac{N_B}{2\pi} \int_\theta^{\theta+2\pi/N_B} \mathbf{u}_W \exp(-i\bar{m}\theta) d\theta \rangle \\ &= \frac{1}{r_D - r_H} \int_{r_H}^{r_D} (\mathbf{v}^L_{mn})^H \left\{ \frac{N_B}{2\pi} \int_\theta^{\theta+2\pi/N_B} \mathbf{u}_W \exp(-i\bar{m}\theta) d\theta \right\} dr \ . \end{aligned} \tag{5.16}$$

As described in §5.1, the unsteady perturbations of uniform mean flows can be represented as superpositions of independent entropic, vortical and irrotational acoustic disturbances. The entropic and vortical disturbances are convected downstream at the mean flow velocity and, if the axial mean flow is subsonic, the acoustic disturbances travel upstream and downstream. For nonuniform mean flows, the situation is more complicated [Kou95]. For example, for a rotational, but isentropic, mean flow, the unsteady entropy is an independent convected disturbance; however, the unsteady vortical and acoustic disturbances are coupled. Thus, instead of independent vortical and acoustic disturbances, downstream traveling, nearly-convected, vorticity-dominated, modal disturbances, which contain pressure, and upstream and downstream traveling, acoustic or pressure-dominated disturbances, which contain vorticity, occur [AG98]. These types of disturbances emerge as solutions of the eigenvalue problem (5.14).

The group velocity

$$V_{g,mn} = \frac{\partial \omega}{\partial \chi_{mn}} = \frac{\langle \mathbf{v}^L_{mn}, \mathbf{C}\mathbf{u}^R_{mn} \rangle}{\langle \mathbf{v}^L_{mn}, (\partial \mathbf{P}/\partial \omega)\, \mathbf{u}^R_{mn} \rangle} \ , \tag{5.17}$$

i.e., the axial velocity at which an unattenuated mnth modal disturbance carries energy, is used to classify disturbances. Nearly-convected disturbances travel downstream, without attenuation, at axial speeds slightly less than and slightly greater than the mean flow speed. Unattenuated acoustic disturbances to a subsonic axial mean flow travel both upstream and downstream.

We can decompose the state vector, $\mathbf{u}_W$, by setting

$$\mathbf{u}_W(r, \theta, \xi) = \mathbf{u}_N(r, \theta, \xi) + \mathbf{u}_A(r, \theta, \xi) \ , \tag{5.18}$$

where $\mathbf{u}_N$ and $\mathbf{u}_A$ are the complex amplitudes of the vorticity- and the pressure-dominated unsteady disturbances, respectively. The state vector for the nearly convected disturbances is given by

$$\mathbf{u}_N = \sum_{m=-\infty}^{\infty} \exp(i\bar{m}\theta) \sum_{\mu=1}^{\infty} \left[a^-_{m\mu,N} \mathbf{u}^{R,-}_{m\mu,N}(r) \exp\left(i\kappa^-_{\xi,m\mu,N}\xi\right) + a^+_{m\mu,N} \mathbf{u}^{R,+}_{m\mu,N}(r) \exp\left(i\kappa^+_{m\mu,N}\xi\right) \right] \tag{5.19}$$

where the index μ indicates the number of radial nodes, and the $-$ and $+$ superscripts refer to disturbances that travel slightly slower and slightly faster than the convection speed. The axial eigenvalues of the modal nearly-convected disturbances are purely imaginary and the axial wave numbers, $\kappa^{-}_{\xi,m\mu,N}$ and $\kappa^{+}_{\xi,m\mu,N}$, are less than and greater than, respectively, the axial wave number of a corresponding mth convected disturbance, i.e., $\kappa^{-}_{\xi,m\mu,N} < \kappa_{\xi,m,C}(r) < \kappa^{+}_{\xi,m\mu,N}$.

The acoustic disturbances, i.e.,

$$\mathbf{u}_A = \sum_{m=-\infty}^{\infty} \exp(i\bar{m}\theta) \sum_{\mu=0}^{\infty} \left[a^{-}_{m\mu,A} \mathbf{u}^{R,-}_{m\mu,A}(r) \exp\left(\chi^{-}_{m\mu,A}\xi\right) + a^{+}_{m\mu,A} \mathbf{u}^{R,+}_{m\mu,A}(r) \exp\left(\chi^{+}_{m\mu,A}\xi\right) \right] \tag{5.20}$$

are also ordered according to the number, μ, of radial nodes, but in this case starting with $\mu = 0$. The $-$ and $+$ superscripts in equation (5.20) refer to upstream and downstream traveling acoustic disturbances, and the eigenvalues, $\chi^{\mp}_{m\mu} = \beta^{\mp}_{m\mu} + i\kappa^{\mp}_{\xi,m\mu}$ are complex.

Numerical Considerations

In numerical calculations, the series in equations (5.12), (5.19) and (5.20) must be truncated, since only finite numbers of circumferential and radial modes can be accommodated. Also, the numerical solutions to (5.15) will yield spurious modes; i.e., modes that satisfy the difference equation (5.15) but not the differential equation (5.14). These modes must be filtered out to yield a valid solution set. Since only a finite number of modes are retained after the truncation and filtering processes, the far field modal description may be incomplete. This caveat applies to both the circumferential and radial modes. Since the acoustic and nearly-convected modes are ordered by the number of radial zero crossings, to determine if any of the lower order modes are missing or if spurious modes are being kept, one can count the zero crossings in the kept modes. If the number of kept modes with a given number of zero crossings is one, or two for the nearly convected modes, then it is likely that only the genuine modes are being retained.

The far field solutions must be applied in conjunction with a numerical near-field solution to determine the linearized unsteady flow. The amplitudes of the incoming unsteady aerodynamic disturbances (excitations) are prescribed, and those of the outgoing disturbances are determined by matching near- and far-field solutions. Convected, nearly-convected, and acoustic disturbances that travel downstream are incoming disturbances at the inflow boundary ($\xi = \xi_-$) of the near-field computational domain, and outgoing disturbances at the outflow ($\xi = \xi_+$) boundary. Acoustic waves that travel upstream are incoming disturbances at $\xi = \xi_+$ and outgoing disturbances at $\xi = \xi_-$.

The amplitudes of the outgoing modal disturbances are determined by taking inner products, cf. (5.16), using the near-field state vector, $\mathbf{u}$ in lieu of $\mathbf{u}_W$. Thus, we assume that $\langle \mathbf{v}^L_{mn}, \mathbf{u} \rangle \approx \langle \mathbf{v}^L_{mn}, \mathbf{u}_W \rangle$, i.e., that the left eigenmodes of the modal disturbances are nearly orthogonal to the convected disturbance. Once the amplitudes of the outgoing modes are determined, by applying (5.16) at the computational inflow and outflow boundaries, the wave-type modes are superposed to provide solutions for $\mathbf{u}_W = \mathbf{u}^A + \mathbf{u}^N$. This solution is based on the finite numbers of circumferential and radial modes that can be represented accurately on the computational grid used to determine the near-field solution.

At the upstream far-field boundary, the convected disturbance is set to describe any incident convected gust. At the downstream far-field boundary, the wave-type modes are subtracted from the total unsteady disturbance and the remainder, $\mathbf{u}_C = \mathbf{u} - \mathbf{u}_W$, is treated as a convected disturbance. The convected disturbance in the region, $\xi > \xi_+$, is computed by the method of characteristics as a solution of the equation $\bar{D}\mathbf{u}_C/Dt \equiv 0$. Since the mean radial velocity has been assumed to be negligible, the functional form of the far-downstream convected field along the constant-radius characteristics is $\mathbf{u}_C(r,\theta,\xi) = \mathbf{u}_C(r,\theta,\xi_+)\exp[-i\omega(\xi-\xi_+)/V_\xi]$.

In the near field, the linearized unsteady governing equations are solved using the pseudo-time marching technique described in §5. After each iterative update of the near-field solution, the amplitudes of the outgoing wave-type modes, i.e., $a^-_{m\mu,A}$ at $\xi = \xi_-$ and $a^+_{m\mu,A}$ and $a^\mp_{m\mu,N}$ at $\xi = \xi_+$, and the far-downstream convected disturbance, $\mathbf{u}_C(r,\theta,\xi_+)$, are updated. The far-field solutions, which are the sums of the incoming and outgoing wave-type and convected disturbances, are then updated, and used to supply the far-field information needed for the next near-field update.

In principle, a linearized unsteady solution could proceed as outlined above. However, in practice, it is very difficult to numerically determine the axial and radial behaviors of the nearly-convected modal disturbances. Therefore, at present, for practical three-dimensional, unsteady flow calculations, some liberties must be taken in describing the unsteady perturbations of nonuniform mean inlet and exit flows. In particular, in the present effort, such perturbations will be represented approximately as the sum of a finite series of acoustically-dominated modal disturbances and a "convected" disturbance field. The axial eigenvalues and radial shapes of the acoustic modes are determined by the far-field eigenanalysis. The amplitudes of the incoming acoustic disturbances are prescribed, and those of the outgoing acoustic disturbances are determined by matching the near- and far-field unsteady solutions. The "convected" disturbance field, $\mathbf{u} - \mathbf{u}^A$, is prescribed at inlet and numerically convected downstream at the exit boundary.

5.3 Numerical Results for Simple Swirling Flows

At this point we have described a theoretical procedure for determining the axial and radial behaviors of unsteady perturbations of a fully-developed, axisymmetric, steady background flow. We proceed now to evaluate the capabilities of the numerical eigenanalysis, currently used in the LINFLUX code, anticipating that it will be difficult to determine the eigenvalues and radial modes of the nearly-convected disturbances, and extremely difficult to represent an arbitrary vortically-dominated disturbance as a series of nearly-convected, modal disturbances.

We have determined numerical eigensolutions for the modal unsteady perturbations of fully-developed, swirling, mean flows. These flows are assumed to occur far upstream of a rotor, consisting of 24 blades, which rotate at constant angular velocity, Ω, and reside in an annular duct with $r_D = 4.244$ and $r_H/r_D = 0.8$. The following conditions are prescribed on

the inlet mean or steady-background flows at midspan, i.e., at $r = r_M = (r_H + r_D)/2$:

$$\bar{\rho}(r_M) = 1.0\ , \quad V(r_M) = 1.0\ , \quad S(r_M) = 0\ ,$$
$$M(r_M) = 0.5\ , \quad \text{and} \quad \Omega_F(r_M) = 55\,\text{deg}\ , \tag{5.21}$$

where M and $\Omega_F = \cos^{-1}(V_\theta/V)$ are the mean-flow Mach number and tangential flow angle, respectively, in the rotating frame. The pressure, $P = \bar{\rho}V^2/(\gamma M^2)$ and the temperature, $T = V^2/[(\gamma - 1)M^2]$, at the reference radial location, $r = r_M$, are 2.857 and 10, respectively.

In addition to these reference flow conditions, we assume that the absolute, circumferential velocity at inlet is given by

$$V^{\text{abs}}_{\theta,-\infty} = C_S + \Omega_S r + \Gamma_S r^{-1}\ , \tag{5.22}$$

where the terms on the right-hand side describe constant, solid-body, and free-vortex swirl velocities, respectively. The swirl velocity, C_S, the angular velocity, Ω_S, and the circulation, Γ_S, are prescribed quantities. Note that $V_\theta = V^{\text{abs}}_\theta - \Omega r$, where Ω is the angular velocity of the rotor, and $V_\theta(r_M) = V \sin\Omega_F$. The radial distributions of temperature, pressure and density can be found by integrating the relations in (5.2). For example the temperature distribution is given by

$$\begin{aligned} T(r) &= T(r_M) + \Omega_S^2(r^2 - r_M^2)/2 + 2\Omega_S C_S(r - r_M) + (2\Omega_S\Gamma_S + C_S^2)\ln(r/r_M) \\ &- 2\Gamma_S C_S(r^{-1} - r_M^{-1}) - \Gamma_S^2(r^{-2} - r_M^{-2})/2\ . \end{aligned} \tag{5.23}$$

Finally, we assume that the absolute total temperature, T^{abs}_T, and the absolute total pressure, P^{abs}_T, are constants, i.e., $T^{\text{abs}}_T(r) = T^{\text{abs}}_T(r_M)$ and $P^{\text{abs}}_T(r) = P^{\text{abs}}_T(r_M)$, and hence, the mean flow is isentropic with $S(r) = 0$. The radial distribution of the inlet axial velocity can be determined from equation (5.4).

Numerical solutions have been determined for absolute steady flows with constant swirl, $V^{\text{abs}}_\theta = C_S$, solid-body swirl, $V^{\text{abs}}_\theta = \Omega_S r$, and free-vortex swirl, $V^{\text{abs}}_\theta = \Gamma_S r^{-1}$. In each case the absolute swirl velocity, V^{abs}_θ, and the blade-row angular velocity, Ω, are prescribed, so that twenty (20) percent of the relative circumferential velocity at midspan, $V_\theta(r_M)$, is due to the absolute flow, and eighty (80) percent is due to blade rotation. Thus, we set $C_S = 0.1638$ for the constant swirl condition, $\Omega_S = 0.0429$ for the solid-body swirl and $\Gamma_S = 0.6258$ for the free-vortex swirl. In each case, $\Omega = -0.1716$. Also, in each case, the absolute total temperature and absolute total pressure are $T^{\text{abs}}_T = 10.178$ and $P^{\text{abs}}_T = 3.039$. The unsteady flow is excited by a disturbance at the blade passing frequency of a stator or stationary blade row consisting of $N_V = 18$ vanes, placed upstream or downstream of the rotor. Thus, the unsteady flows occur at $\omega = -N_V\Omega = 3.089$ and $\sigma = -2\pi N_V/N_B = -3\pi/2$.

The radial distributions of selected mean flow quantities are shown in Figure 2 for the flow with constant swirl. The fluid thermodynamic properties, $\bar{\rho}, P$ and T, vary only very slightly with radius; the axial velocity varies from 0.579 at the hub to 0.569 at the tip; the relative circumferential velocity, from 0.746 to 0.892; and the radial velocity is zero. The relative inlet Mach number and flow angle vary from 0.472 and 52.19 deg, respectively, at the hub, to 0.529 and 57.48 deg at the tip.

The predicted axial eigenvalues and radial pressure modes for the acoustic disturbances to the prescribed mean flow with constant swirl are shown in Figures 3 and 4, respectively. The numbers m, μ above each symbol in Figure 3, indicate the circumferential (m) and radial (μ) mode orders of the acoustic disturbance. Only the acoustic disturbances in the (1,0) mode are of propagating type. These disturbances repeat six times around the wheel and travel in the direction of rotor rotation. The upstream propagating or response disturbance has an axial wave number, κ_ξ^-, of 2.411; the downstream propagating disturbance (excitation), an axial wave number of -1.046. The radial pressure modes, $p^R_{m\mu}(r)$, of the upstream traveling acoustic disturbances at $m = -2, \ldots, 2$ and $\mu = 0, 1, 2$ are shown in Figure 4. The pressure in the upstream propagating (1,0) mode shows very little variation with radius. However, the upstream decaying modes show significant radial variation.

We have determined results, similar to those in Figures 2 through 4, for the mean flow with solid-body swirl, $V_\theta^{\text{abs}} = 0.0429r$, and for the mean flow with free vortex swirl, $V_\theta^{\text{abs}} = 0.6258r^{-1}$. In both cases the mean flow thermodynamic properties ($\bar{\rho}, P$, and T) are almost constant across the duct. For the solid-body swirl, the mean axial velocity varies from 0.583 at the hub to 0.562 at the tip; the relative inlet Mach number, from 0.467 to 0.535; and the relative inlet flow angle, from 51.30 deg to 58.28 deg. For the free-vortex swirl, the axial velocity is constant across the duct, $V_\xi = 0.574$, the relative Mach number varies from 0.479 at the hub to 0.523 at the tip, and the relative flow angle, from 53.20 deg at the hub to 56.77 deg at the tip.

For each of these steady background flows, the predicted axial eigenvalues and radial pressure modes, at $m = -2, \ldots, 2$ and $\mu = 0, 1, 2$, for an acoustic disturbance at $\omega = 3.089$ and $\sigma = -3\pi/2$ are in close agreement with the corresponding predictions for the mean flow with constant swirl. The axial eigenvalues for the solid-body and free-vortex swirl cases are shown in Figure 5. For the solid-body swirl, the upstream propagating acoustic disturbance has an axial wave number $\kappa_\xi^- = 2.410$ and for the downstream propagating disturbance $\kappa_\xi^+ = -1.046$. For the free-vortex swirl, $\kappa_\xi^- = 2.412$ and $\kappa_\xi^+ = -1.047$.

We have also examined acoustic disturbances, at $\omega = 3.089$ and $\sigma = -3\pi/2$, to a uniform mean inlet flow, $V_\theta^{\text{abs}} = 0$, at $T_T^{\text{abs}} = 10.164$, $P_T^{\text{abs}} = 3.025$. Again, the lowest-order axial eigenvalues and radial pressure modes are in close agreement with the corresponding results for the three swirling flows, indicating that the uniform flow or "Tyler-Sofrin" modes may often be useful approximations to the acoustic modes of closely related nonuniform mean flows.

We have not been successful in determining the modal, nearly-convected, unsteady disturbances of the swirling mean flows considered above. For the most part, the axial eigenvalues of these disturbances could not be determined or, when such eigenvalues appeared to be predicted, the corresponding radial distributions of the fluid dynamic variables indicated the modes to be spurious. Because of the serious difficulties associated with representing incoming vortical or wake excitations as a series of nearly-convected modal disturbances, we will adopt the interim, practical, solution strategy, described at the end of §5.3, for unsteady flows, excited by wake/blade-row interactions. In particular, we will represent both the convected and nearly-convected unsteady perturbations of nonuniform flows as convected disturbances. Since the present numerical eigenanalysis seems to identify the axial eigenvalues and radial modes of acoustic perturbations to nonuniform flows, we will apply this

analysis to represent the modal acoustic disturbances in the far upstream and far downstream regions of the flow. Thus, in the far field, we will assume an approximate solution for the state vector, $\mathbf{u}$, of the form $\mathbf{u} = \mathbf{u}_A + \mathbf{u}_C$. The state vector $\mathbf{u}_A$ represents a finite series of low $|m|$ and μ order acoustic disturbances and the vector $\mathbf{u}_C$ represents the remaining part of the unsteady perturbation, which will be treated as a convected disturbance.

6. Analytic Wake Excitation Model

Consider a reference rotating or stationary blade row, see Figure 6, which receives the flow coming from an adjacent upstream row (i.e., a stator or a rotor, respectively). The upstream and reference blade rows rotate at constant angular velocity Ω' and Ω, respectively. Therefore, the upstream blade row rotates at angular velocity $\Omega' - \Omega = \Omega_R = \Omega_R \mathbf{e}_\xi$ relative to the reference array, where Ω_R is the absolute angular velocity of the rotor. Because the blade rows move relative to each other, any downstream traveling steady flow nonuniformity produced by the upstream blade row; e.g., a nonuniformity due to the viscous blade wakes, will excite an unsteady flow through the reference row. Although the wake excitation to the reference array is associated with viscous effects in the flow through the upstream blade row, it will be treated here as an inviscid velocity perturbation at the inlet to the responding or reference blade row.

We will analyze the flow through the reference blade row in terms of cylindrical coordinates (r, θ, ξ) and $(r, \theta' = \theta - \Omega_R t, \xi)$ attached to the reference and the upstream or excitation blade rows, respectively. Here, both θ and θ' measure angular distance in the $\mathbf{e}_\xi \times \mathbf{e}_r = \mathbf{e}_\theta$ direction, where the radial unit vector $\mathbf{e}_r$ points from hub to tip. We assume that in the absence of the reference blade row, the flow "far" downstream of the excitation blade row is steady in the r, θ', ξ coordinate frame, with relative velocity, $\tilde{\mathbf{V}}'(r, \theta', \xi)$, density, $\tilde{\rho}$, and the pressure $\tilde{P}$, given by

$$\begin{aligned} \tilde{\mathbf{V}}'(r, \theta', \xi) &= \mathbf{V}'(r) + \tilde{\mathbf{v}}^{\mathrm{R}}(r, \theta', \xi) + \ldots \\ &= [V'(r) + \tilde{v}^{\mathrm{R}}(r, \theta', \xi)]\mathbf{e}_T(r) + \ldots = \tilde{V}'(r, \theta', \xi)\mathbf{e}_T(r) \qquad (6.1) \\ \tilde{\rho}(r, \theta', \xi) &= \bar{\rho}(r) + \ldots \quad \text{and} \quad \tilde{P}(r, \theta', \xi) = P(r) + \ldots . \end{aligned}$$

Here $\boldsymbol{V}'$, $\bar{\rho}$ and P are circumferentially-averaged flow properties, $\tilde{\mathbf{v}}^{\mathrm{R}}(r, \theta, \xi)$ is the first-order velocity perturbation due to the wakes off the blades in the upstream blade row, the density and pressure fluctuations associated with this velocity perturbation are assumed to be negligible, and $\mathbf{e}_T(r)$ is a unit vector tangent to the cylinder r = constant and pointing in the far-downstream flow direction. Thus, far downstream of the excitation blade row, the radial component of the total fluid velocity is negligible and the circumferentially-averaged fluid velocity, $\mathbf{V}'(r)$ is axisymmetric and independent of axial distance. We assume that circumferentially-averaged flow is a solution of the fluid-dynamic conservation equations; i.e., the nonlinear Euler equations, for steady inviscid flow, cf. §5. However, in general, our analytical representation for the wake perturbation will only approximate a true solution to the linearized Euler equations.

The flow velocity, $\tilde{\mathbf{V}}' = \tilde{V}'\mathbf{e}_r$, far downstream of the exciting blade row can be expressed in terms of a Fourier series, i.e.,

$$\tilde{V}'(r, \theta', \xi) = \sum_{n=-\infty}^{\infty} V'_n(r, \xi) \exp(-inN'\theta') = V'_0(r) + \sum_{n=1}^{\infty} \mathrm{Re}\{v^{\mathrm{R}}_n(r, \xi) \exp(-inN'\theta')\} \qquad (6.2)$$

where $N' > 0$ is the number of blades in the upstream blade row and the Fourier coefficients, V_n, are given by

$$V'_n(r,\xi) = \frac{N'}{2\pi}\int_{\theta'}^{\theta'+2\pi/N'} \tilde{V}'(r,\theta',\xi)\exp(inN'\theta')d\theta', \quad n = 0,\pm1,\pm2,\ldots \tag{6.3}$$

Here, $V'_0 = V'$ is the circumferentially-averaged value of the far-downstream flow velocity and $v_n^{\mathrm{R}}(r,\xi) = 2V'_n, n = 1,2,\ldots$, is the complex amplitude of the nth circumferential harmonic component of the perturbation velocity. The velocity $\tilde{\mathbf{V}}'$, and therefore, V', the perturbation velocity $v_n^{\mathrm{R}}(r,\xi), n = 1,2,\ldots$, and the unit vector $\mathbf{e}_T(r)$, can be determined experimentally or by performing a viscous flow calculation to determine the steady relative flow through the upstream blade row.

If we assume that the complex amplitudes of the Fourier components of the perturbation velocity, $\mathbf{v}_n^{\mathrm{R}} = v_n^{\mathrm{R}}\mathbf{e}_T$, vary harmonically with axial distance, i.e., $v_n^{\mathrm{R}}(r,\xi) = v_n^{\mathrm{R}}(r)\exp(in\kappa_\xi\xi)$, and set

$$\boldsymbol{\kappa} = \kappa_T\mathbf{e}_T = (\kappa_\xi V_\xi - r^{-1}N'V'_\theta)\mathbf{e}_T/V' = 0\ , \tag{6.4}$$

where κ_T is the wave number of a "convected" velocity perturbation in the relative flow direction; then the foregoing first-order flow perturbation will satisfy the linearized, inviscid, conservation equations for mass, axial and circumferential momenta, and energy. However, in general, this representation of a wake excitation does not satisfy the linearized conservation equation for radial momentum, unless the absolute steady background flow is uniform. Thus, for a nonuniform, absolute mean flow, it is, at best, only a convenient and hopefully useful, approximate solution to the fluid-dynamic equations governing the inviscid flow through the reference blade row.

The flow exiting from the upstream or excitation blade row enters the field of the reference blade row. In particular, the imposed relative velocity at the inlet to the reference blade row is

$$\tilde{\mathbf{V}} = \tilde{\mathbf{V}}' + \Omega_R\mathbf{e}_\xi \times \mathbf{r} = \mathbf{V}' + \Omega_R\mathbf{e}_\xi \times \mathbf{r} + \tilde{\mathbf{v}}^{\mathrm{R}} + \ldots = \mathbf{V} + \tilde{\mathbf{v}}^{\mathrm{R}} + \ldots \tag{6.5}$$

where the perturbation velocity, $\tilde{\mathbf{v}}^{\mathrm{R}}$, is invariant under a transformation from the r,θ',ξ frame to the r,θ,ξ frame. Thus, in terms of the coordinates r,θ,ξ fixed to the reference blade row, the steady and unsteady perturbation velocities at inlet are

$$\mathbf{V}(r) = V_\xi\mathbf{e}_\xi + (V'_\theta + \Omega_R r)\mathbf{e}_\theta = V_\xi\mathbf{e}_\xi + V_\theta\mathbf{e}_\theta \tag{6.6}$$

and

$$\tilde{\mathbf{v}}^{\mathrm{R}} = \sum_{n=1}^{\infty}\mathrm{Re}\{\mathbf{v}_n^{\mathrm{R}}\exp[in(\kappa_\xi\xi - N'\theta + N'\Omega_R t)]\}\ , \tag{6.7}$$

where

$$\tilde{\mathbf{v}}_n^{\mathrm{R}} = (v_n^{\mathrm{R}}/V')(V_\xi\mathbf{e}_\xi + V'_\theta\mathbf{e}_\theta) = (v_n^{\mathrm{R}}/V')[V_\xi\mathbf{e}_\xi + (V_\theta - \Omega_R r)\mathbf{e}_\theta]\ , \tag{6.8}$$

$\omega = N'\Omega_R$ is the fundamental ($n = 1$) excitation frequency in the frame of the reference blade row and $\kappa_\xi = -(\omega - r^{-1}N'V_\theta)/V_\xi$ is the axial wave number of the fundamental wake excitation. The interblade phase angle, σ, of the fundamental excitation is $-2\pi N'/N$, where N is the number of blades in the reference blade row.

Each term on the right-hand-side of equation (6.7) can be determined from the zeroth-order term in the general expression, (5.12), for a convected disturbance at frequency ω by setting $m = 0$, $\bar{m} = N_D = -nN'$, $\omega = nN'\Omega_R$, and $\kappa_{\xi,0} = -nN'\left[\Omega_R - r^{-1}V_\theta(r)\right]/V_\xi(r)$ in equation (5.12). Note that, if the upstream blade row is a stator, $\mathbf{V}'$ is the absolute steady fluid velocity and $\mathbf{V}$ is the velocity relative to the reference rotor blade row. If the upstream blade row is a rotor, $\mathbf{V}'$ is the velocity relative to the rotor and $\mathbf{V}$ is the absolute fluid velocity. In both situations, $\mathbf{\Omega}' - \mathbf{\Omega} = \Omega_R \mathbf{e}_\xi$, where Ω_R is the absolute angular speed of the rotor.

7. Numerical Results: 3D 10th Standard Configuration

The 3D 10th Standard Cascade (3D SC10) consists of 24 blades placed within a cylindrical annular duct of inner radius $r_H = 3.395 = 0.8 r_D$ and outer radius $r_D = 4.244$. It operates in a uniform axial mean inlet flow, which, in the present study, occurs at $M^{\text{abs}}_{-\infty} = 0.2868$, and rotates at constant angular velocity $\Omega = -0.2145 \mathbf{e}_\xi$. The blades are twisted to reduce the variation in relative mean incidence caused by blade rotation, and there is no clearance between the blades and the outer duct wall.

At midspan ($r = r_{\text{M}} = 0.9 r_D$), the blades are staggered at $\Theta(r_{\text{M}}) = 45\,\text{deg}$ with a circumferential spacing, $G(r_{\text{M}}) = 2\pi r_{\text{M}}/N_{\text{B}}$, of unity, and the blade cross section is a NACA 5506 airfoil, altered slightly [Ver89], to close in a wedge-shaped trailing edge. This midspan geometry was chosen to match the 2D 10th Standard Configuration of [FV93]. The relative inlet Mach number, $M_{-\infty}$, and the relative inlet flow angle, $\Omega_{-\infty} = \tan^{-1}(V_\theta/V_\xi)$, at midspan, are 0.5 and 55 deg, respectively.

The mean blade chord lines are located at

$$r\theta = \xi \tan\Theta(r) + nG(r), \quad 0 \le \xi \le c_{\text{ax}}, \quad n = 0, \ldots, N_{\text{B}} - 1\ , \tag{7.1}$$

where

$$\tan\Theta(r) = (r/r_{\text{M}}) \tan\Theta(r_{\text{M}}) \tag{7.2}$$

and the axial chord, $c_{\text{ax}} = c(r)\cos\Theta(r) = c(r_{\text{M}})\cos\Theta(r_{\text{M}})$, is constant. Hence, $\xi = 0$ and $\theta = 0$ at the reference blade ($n = 0$) leading edge and $\xi = \cos 45\,\text{deg}$ at the trailing edge, along the entire span. The airfoil chord, $c(r)$, varies from 0.946 at the hub to 1.057 at the tip, and the local thickness to chord ratio varies to maintain constant thickness.

TURBO nonlinear steady and LINFLUX linearized unsteady solutions for the 3D SC10 have been determined, over a single extended blade passage, on an H-type grid, cf. Figure 7, consisting of 141 axial, 41 tangential and 11 radial surfaces (56,000 cells), with 81 axial surfaces intersecting the blades. This H-grid extends approximately one axial chord upstream and downstream from the blade row. Axial grid surfaces are clustered near blade leading and trailing edges; circumferential surfaces, near the blades; and the radial surfaces are distributed uniformly. The LINFLUX near-field, finite-volume solutions have been coupled to far-field acoustic eigensolutions, which have been determined on a radial grid consisting of 36 points clustered near the hub and duct walls. For the unsteady flows under consideration, convected vortical disturbances are prescribed at inlet, and any convected or nearly convected disturbances that occur downstream of the blade row are simply convected numerically through the computational outflow boundary.

The 3D SC10 solutions reported herein were determined on an IBM-3CT Workstation. At present, LINFLUX has no convergence acceleration. As a result, 5,000 to 8,000 pseudo-time steps, with two SGS subiterations at each time step, were applied to converge the LINFLUX SC10 calculations. Approximately 600 time steps could be completed per CPU hour on an IBM 3CT, corresponding to 110μsec/time-step/cell or 8 to 13 CPU hrs for a solution. The computing resources required for executing LINFLUX are much less than those that would be required to determine a nonlinear unsteady solution using TURBO, especially for excitations at nodal diameters that require nonlinear solutions over a large number of blade passages.

In addition to the 3D LINFLUX results, for purposes of comparison, we have also determined predictions for the 10th Standard Cascade using the two-dimensional steady full-potential analysis CASPOF [Cas83] and the potential-based, linearized unsteady analysis, LINFLO [Ver93]. The full potential steady solution for the midspan section of the 3D SC10 has been determined on a composite mesh consisting of a local C-mesh embedded in a global H-mesh; the LINFLO unsteady solutions, on a streamline 155 × 41 H-mesh. The H-meshes used in the CASPOF and LINFLO calculations extend one axial chord upstream and downstream from the blade row.

7.1 Steady Background Flow/Vortical Excitations

Predictions for the steady background flows through the 3D and 2D 10th Standard Cascades have been determined using the TURBO 3D nonlinear Euler and the CASPOF 2D full-potential analyses. For the TURBO calculations, the relative total pressure, total temperature, and flow angle are specified at inlet (i.e., at $\xi = \xi_-$), and the mean-flow static pressure at the hub is specified at the exit ($\xi = \xi_+$). For the CASPOF calculation, the relative inlet Mach number, $M_{-\infty} = 0.5$, and inlet flow angle, $\Omega_{-\infty} = 55\,\text{deg}$, are specified and a Kutta condition is imposed at the blade trailing edges. In the present study, the exit static pressure for the 3D calculation has been chosen such that the relative inlet flow at midspan matches the conditions prescribed for the 2D CASPOF calculation.

The 3D 10th Standard Cascade operates in a uniform, absolute, mean inlet flow, but, because of steady blade loading, the mean exit flow has swirl and axial shear. Radial distributions of selected inlet and exit, mean-flow quantities for the 3D SC10, operating at $M^{\text{abs}}_{-\infty} = 0.2868$ and $\Omega = \Omega \mathbf{e}_\xi = -0.2145 \mathbf{e}_\xi$, are shown in Figure 8. For the three-dimensional flow, the steady pressure ($P = 2.857$), density ($\bar{\rho} = 1.0$), and axial velocity ($V_\xi = 0.574$) are constant at inlet, the relative circumferential velocity, $V_\theta = -\Omega r$ varies linearly from 0.728 at the hub to 0.910 at the tip, and the relative Mach number, $M = [\bar{\rho}/(\gamma P)]^{1/2} V$ varies from 0.464 at the hub to 0.578 at the tip. At the exit boundary, the steady pressure, density, and axial velocity vary with radius, and the circumferential velocity varies nonlinearly with radius. The steady blade loading for this compressor blade row leads to small increases in the pressure and density, a small decrease in the axial velocity and relatively large decreases in the circumferential velocity and Mach number, across the blade row.

Predicted, steady, isentropic, surface Mach number and surface pressure distributions for the 3D 10th Standard Cascade, are shown in Figures 9 and 10. The isentropic Mach number, i.e.,

$$M_i = \left\{ 2(\gamma - 1)^{-1} \left[(P_{T,-\infty}/P)^{\frac{\gamma-1}{\gamma}} - 1 \right] \right\}^{1/2} \tag{7.3}$$

is based on the local static pressure, $P(r, \theta, \xi)$ and the local relative total pressure, $P_{T,-\infty}(r)$ at inlet. The TURBO steady-flow predictions at the hub, $r/r_{\text{D}} = 0.8$, midspan, $r/r_{\text{D}} = 0.9$, and tip, $r/r_{\text{D}} = 1.0$, in Figures 9 and 10, indicate that the isentropic Mach numbers and pressures on the blade suction and pressure surfaces vary with radius, leading to a small increase in blade loading with increasing radius. In addition, the 3D TURBO predictions at midspan are in close agreement with the 2D CASPOF predictions.

We will consider the response of the 3D Tenth Standard Cascade to a fundamental vortical excitation coming from an adjacent upstream stator consisting of N_V equally-spaced vanes.

The circumferentially-averaged background flow at the rotor inlet (stator exit), $\mathbf{V}^{\mathrm{abs}} = V_\xi \mathbf{e}_\xi$, is assumed to be axial and uniform. Superimposed on this uniform axial mean flow is a vortical axial velocity perturbation, $\tilde{\mathbf{v}}^{\mathrm{R}} = \tilde{v}^{\mathrm{R}} \mathbf{e}_\xi$, which is steady in the stator or absolute frame, but unsteady in the rotor or relative frame.

It follows from equations (6.6) and (6.7), with $\mathbf{\Omega}_R = -\mathbf{\Omega}$, $N' = N_V$ and $n = 1$, that the relative steady and unsteady velocities at the rotor inlet, i.e., "far" upstream of the rotor, are given by

$$\mathbf{V} = \mathbf{V}^{\mathrm{abs}} + |\mathbf{\Omega}| r \mathbf{e}_\theta = V_\xi \mathbf{e}_\xi + |\mathbf{\Omega}| r \mathbf{e}_\theta \tag{7.4}$$

and

$$\tilde{\mathbf{v}}^R = \mathrm{Re}\left\{ v^{\mathrm{R}} \mathbf{e}_\xi \exp\left[i(-N_V \theta^{\mathrm{rel}} + N_V |\mathbf{\Omega}| t) \right] \right\} . \tag{7.5}$$

The frequency of the unsteady vortical excitation in the rotor frame is $\omega = N_V |\mathbf{\Omega}| = -N_V \Omega$, the axial wave number, κ_ξ, of this excitation is zero, and the fundamental interblade phase angle, σ, is $-2\pi N_{\mathrm{V}}/N_{\mathrm{B}}$. We are assuming that there is no density, pressure, radial velocity or circumferential velocity associated with the axial velocity perturbation (7.5). Therefore, the state vector, $\mathbf{u}_C$, associated with this perturbation has the form $\mathbf{u}_C^T = \bar{\rho}(0, 0, 0, v_\xi^R, V_\xi v_\xi^R)$. Since the underlying absolute mean flow is uniform, $\mathbf{u}_C$ is an exact solution of the linearized, inviscid, unsteady equations.

For the present purpose of validating the LINFLUX code for relatively simple unsteady flows, we assume that the complex amplitude, $\mathbf{v}^{\mathrm{R}}(r)$, of the vortical velocity is constant along the span. Also, to allow convenient comparisons between 3D LINFLUX and 2D LINFLO response predictions at blade midspan, we choose this constant such that

$$\mathbf{v}^{\mathrm{R}} \cdot \mathbf{e}_N = v^{\mathrm{R}} \mathbf{e}_\xi \cdot \mathbf{e}_N = -v^{\mathrm{R}} \sin \Omega_{-\infty}(r_M) = (1, 0) \quad \text{at} \quad r = r_M , \tag{7.6}$$

Here, $\mathbf{e}_N = \mathbf{V} \times \mathbf{e}_r / |\mathbf{V}|$ is a unit vector tangent to the cylinder $r =$ constant and normal to the inlet steady relative velocity, and $\Omega_{-\infty} = \tan^{-1}(V_\theta / V_\xi)$ is the steady relative inlet flow angle at midspan ($r = r_{\mathrm{M}}$). Thus, the vortical excitation from upstream has a complex amplitude, v^R, of (-1.221,0) and it is convected by a mean flow, which has velocity components, $V_{\xi,-\infty} =$ 0.574 and $V_{\theta,-\infty} = |\mathbf{\Omega}| r$ at inlet.

7.2 Unsteady Response Predictions

We consider fundamental wake (vortical) excitations coming from upstream stators consisting of $N_V = 6, 12$ and 18 blades. These excitations produce unsteady flows through the 3D SC10 at $\omega = -N_V \Omega = 1.287$ and $\sigma = -2\pi N_V / N_B = -90\,\mathrm{deg}$, $\omega = 2.574$ and $\sigma = -180\,\mathrm{deg}$, and $\omega = 3.861$ and $\sigma = -270\,\mathrm{deg}$, respectively. The LINFLUX predictions for the axial eigenvalues of the far field acoustic disturbances, associated with such unsteady flows are shown in Figures 11 through 13. The designations upstream decaying and upstream propagating in these figures refer to acoustic response disturbances at inlet and acoustic excitations at exit; the terms downstream decaying and downstream propagating refer to excitations at inlet and responses at exit. The amplitudes of the acoustic response disturbances are determined by matching the LINFLUX near- and far-field solutions. The amplitudes of the acoustic excitations are set equal to zero in the present study on wake/blade-row interactions.

The results in Figures 11 through 13 indicate that all acoustic disturbances attenuate with increasing axial distance from the blade row for the unsteady flows at $\omega = 1.287$ and $\sigma = -90\,\mathrm{deg}(N_V = 6)$, and $\omega = 2.574$ and $\sigma = -180\,\mathrm{deg}(N_V = 12)$. For $N_V = 6$, the least-damped modes occur at $m, \mu = 0, 0$; for $N_V = 12$, at $m, \mu = 1, 0$. For the unsteady flow at $\omega = 3.861$ and $\sigma = -270\,\mathrm{deg}(N_V = 18)$, propagating acoustic response disturbances, at $m, \mu = 1, 0$, occur far upstream and downstream of the blade row. The remaining acoustic response modes attenuate, with the 1,1 mode having the lowest attenuation constant, $|\beta|$.

The 3D LINFLUX predictions indicate that the upstream and downstream propagating acoustic responses at $N_V = 18$ occur at axial eigenvalues $\chi^-_{1,0} = (0, 3.075)$ and $\chi^+_{1,0} = (0, -1.153)$. Here, the $\chi^{\mp}_{m,\mu}$ are the axial eigenvalues of the acoustic response disturbances in the mth circumferential and the μth radial mode, and the superscripts $-$ and $+$ refer to the upstream and downstream traveling disturbances, respectively. The axial eigenvalues of the least-damped, modal, acoustic responses are as follows: for $N_V = 6$, $\chi^-_{0,0} = (1.642, 0)$ and $\chi^+_{0,0} = (-1.611, 0.084)$; for $N_V = 12$, $\chi^-_{1,0} = (1.685, 0.803)$ and $\chi^+_{1,0} = (-2.453, 0.563)$; and for $N_V = 18$, $\chi^-_{1,1} = (3.152, 0.803)$ and $\chi^+_{1,1} = (-3.425, 0.646)$.

A two-dimensional, unsteady analysis will provide one upstream and one downstream axial eigenvalue, say $\chi^{\mp}_m$, for each circumferential acoustic response mode. These approximate the axial eigenvalues of the zeroth-order radial modes in a three-dimensional flow. In the present study, the far-field eigenvalues, $\chi^{\mp}_m$, $m = 0, \pm 1, \pm 2$, for the 10th Standard Cascade, as predicted using the 2D LINFLO analysis, are in very good agreement with the 3D LINFLUX predictions for $\mu = 0$. In particular, the 2D predictions for the least damped acoustic response modes for $N_V = 6$ are $\chi^-_0 = (1.640, 0)$ and $\chi^+_0 = (-1.601, 0.081)$; those for $N_V = 12$ are $\chi^-_1 = (1.700, 0.804)$ and $\chi^+_1 = (-2.468, 0.567)$. The LINFLO predictions for the eigenvalues of the propagating waves at $N_V = 18$ are $\chi^-_1 = (0, 3.080)$ and $\chi^+_1 = (0, -1.159)$. The 2D solution does not contain the least-damped, (1,1) disturbance modes that occur in the 3D unsteady flow at $N_V = 18$.

As indicated by the results in Figures 11 through 13, the axial wave numbers of the attenuating acoustic disturbances do not depend on radial mode number for the uniform mean flow far upstream; but, in the far downstream region, where the mean flow is nonuniform, the axial wave numbers of the attenuating disturbances in a given circumferential mode vary with radial mode number, μ. Also, valid modes can be inadvertently filtered out by the LINFLUX far-field eigenanalysis; e.g., the upstream and downstream decaying 1,2 modes at inlet and the downstream decaying 0,2 and 2,2 modes at exit are missing from the results for $N_V = 18$. Fortunately, such missing modes are usually highly attenuated, and therefore are expected to have little impact on the unsteady solutions far from the blade row.

The radial eigenmodes of the pressures associated with the 3D SC10 far upstream and far downstream acoustic responses are shown in Figures 14 through 16. Although the inlet and exit mean-flow conditions differ, the upstream and downstream radial pressure modes are very similar, with the downstream modes showing a somewhat greater radial variations than their upstream counterparts. Note that the phases of the modal pressure disturbances are independent of radius for the uniform absolute mean flow at inlet, but vary with radius for the nonuniform mean flow that exists in the far downstream region. Thus, the far-upstream, pressure modes, $p^R(r)$, are purely real, but the far-downstream modes have some imaginary or out-of phase content. Also, the least-damped acoustic modes for $N_V = 6$, i.e., the 0,0 modes, show very little radial variation. The least damped modes for $N_V = 12$ (the 1,0

modes) show some variation. Finally, the propagating (1,0) modes for $N_V = 18$ show little radial variation, but the least-damped (1,1) modes show strong radial variation.

Unsteady blade-surface pressure responses for the 3D SC10, subjected to vortical excitations at $N_V = 6, 12$ and 18, are given in Figures 17 through 22. In particular, 3D LINFLUX solutions for the unsteady surface pressure distributions at the hub, midspan and tip of the reference [i.e., $n = 0$, in (7.1)] 3D SC10 blade are given in Figures 17 through Figures 19, and LINFLUX and 2D LINFLO solutions for the unsteady surface pressures at midspan are given in Figures 20 through 22. Here, the real and imaginary components of the pressure are in- and out-of-phase, respectively, with the excitation velocity at the blade leading-edge at midspan, i.e., at $(r, \theta, \xi) = (r_M, 0, 0)$.

The LINFLUX surface pressure predictions at the hub, midspan and tip in Figures 17 through 19 show reasonable spanwise trends, with, as might be expected, rather small radial variations in unsteady pressure. The LINFLUX and LINFLO results at midspan in Figures 20 through 22 are in very good agreement for the vortical excitations at $N_V = 6$ and 12, but the agreement, although very reasonable, is not as close for the excitation at $N_V = 18$. The reasons for the discrepancies between the LINFLUX and LINFLO predictions for the surface pressure responses at $N_V = 18$ are not clear, but possibilities include insufficient mesh resolution, numerical losses in the steady and linear unsteady Euler calculations, and the existence of three-dimensional acoustic responses that are not predicted by a two-dimensional calculation. Recall that the least-damped, attenuating acoustic response modes, i.e., the 1,1 modes for the vortical excitation at $N_V = 18$ have significant radial variation and are not accounted for in 2D solutions.

Contours of the in-phase component, $\mathrm{Re}\{p\}$, of the unsteady pressure at midspan, as predicted by the 3D LINFLUX and 2D LINFLO analyses, for the unsteady flows through the 3D SC10, caused by the vortical excitations at $N_V = 6, 12$ and 18, are shown in Figures 23 through 25. In each case, the unsteady pressure fields predicted by the two analyses are in good agreement. The unsteady pressure responses associated with the vortical excitations at $N_V = 6$ and $N_V = 12$ attenuate with increasing distance from the blade row. Thus, the unsteady pressure variations at the computational inlet and exit boundaries, shown in Figures 23 and 24, are due primarily to the least damped modal acoustic response disturbances, i.e., the 0,0 disturbances for $N_V = 6$ and the 1,0 disturbances for $N_V = 12$. The excitation at $N_V = 18$ produces propagating 1,0 acoustic response waves of significantly larger amplitude at the inlet and exit boundaries, as indicated by the results in Figure 25.

The LINFLUX calculations indicate that the vortical excitation at $N_V = 6$ produces attenuating (0,0) acoustic response disturbances at amplitudes of 0.144 and 0.075 at the computational inlet and exit boundaries, respectively. The vortical excitation at $N_V = 12$ produces attenuating (1,0) disturbances at amplitudes of 0.190 and 0.033 at these boundaries. The corresponding LINFLO results are 0.113 and 0.091 for $N_V = 6$ and 0.142 and 0.038 for $N_V = 12$. Although the predicted amplitudes of the 3D and 2D attenuating acoustic responses are not expected to be identical, particularly since the axial extents of the 3D and 2D computational domains differ, some level of agreement suggests that both analyses are providing accurate predictions.

The vortical excitation at $N_V = 18$ ($\omega = 3.861$ and $\sigma = -270$ deg) produces propagating 1,0 acoustic responses upstream and downstream of the 3D SC10 rotor. These disturbances occur at $\bar{m} = mN_B - N_V = 6$, i.e., at an interblade phase angle, $\sigma_1 = 2\pi\bar{m}/N_B$, of 90 deg.

Therefore, they repeat six times around the wheel and travel in the direction of rotor rotation. The LINFLUX and LINFLO predictions for the amplitudes of the upstream propagating acoustic response wave are 0.243 and 0.248, respectively, those for the downstream travelling wave are 0.405 and 0.390. If we define a circumferential wave number, κ_η, as $\kappa_\eta = \bar{m}/r$, then the LINFLUX solution, at midspan, indicates that the upstream propagating wave has a wavelength $2\pi/(\kappa_\xi^2 + \kappa_\eta^2)^{1/2}$ of 1.820 and propagates away from the blade row and in the direction of rotor rotation at an angle $\alpha = 180\,\text{deg} - \tan^{-1}(\kappa_\eta/\kappa_\xi)$ of 152.9 deg from the axial flow direction. The downstream propagating response disturbance has a wavelength of 3.224 and travels away from the blade row and in the direction of rotor rotation at an angle $\alpha = 180\,\text{deg} - \tan^{-1}(\kappa_\eta/\kappa_\xi) = 53.72\,\text{deg}$. The LINFLO predictions for the wavelengths and propagation angles of the 1,0 acoustic response waves are in very close agreement with the foregoing LINFLUX predictions.

The foregoing validation study, on a relatively simple 3D model problem, suggests that the LINFLUX code is giving accurate predictions for the unsteady pressure responses resulting from the interactions of vortical gusts with a rotating blade row. One area of concern involves the differences, indicated in Figure 22, between the LINFLUX and LINFLO surface pressure predictions for the gust at $N_V = 18$. We have performed a mesh resolution study to test whether the LINFLUX results will approach those of LINFLO if a more refined mesh is used for the LINFLUX calculations. For this purpose, we have applied the 2D LINFLUX code [MV95] to predict the unsteady flow through the 2D 10th Standard Cascade that is excited by a vortical disturbance from upstream at $\mathbf{v}^R \cdot \mathbf{e}_N = (1, 0)$, $\omega = 3.861$ and $\sigma = -270\,\text{deg}$. The 2D LINFLUX results were determined on a 141 $\times$ 41 grid, similar to that used at midspan in the 3D LINFLUX calculations, and on refined meshes that are 1.5 and 2.0 times as dense as this 141 $\times$ 41 mesh.

Results for the steady isentropic Mach number and unsteady pressure distributions along the reference blade surface are shown in Figures 26 and 27, respectively. The CASPOF and LINFLO results, indicated by the dashed lines in these figures, are the same as those shown in Figures 9 and 22. The LINFLUX results indicate that the mesh refinement has had a negligible impact on the surface Mach number and unsteady pressure predictions. However, the 2D LINFLUX surface pressure distributions are in better agreement with the LINFLO predictions than the corresponding 3D LINFLUX results. This suggests that some of the differences between the LINFLO and the 3D LINFLUX solutions, indicated in Figure 22, are due to the three-dimensional effects that are not captured by the LINFLO analysis.

The 2D unsteady vorticity and pressure fields predicted by the LINFLUX and LINFLO codes, are shown in Figures 28 and 29. The LINFLUX solution on the 281 $\times$ 81 mesh shows vorticity contours that become severely distorted, especially near the blades and their wakes, as the gust moves downstream. Such distortions are even more severe in the coarser-mesh LINFLUX solutions, and probably contribute to the relatively small differences between the LINFLUX and LINFLO unsteady surface pressure predictions. The unsteady pressure fields resulting from the 2D LINFLUX and LINFLO calculations are in good agreement as indicated by the contours shown in Figure 29. Thus, the severe distortion of the vortical gust produced by the LINFLUX calculation seems to have only a minor impact on the unsteady pressure response. Part of the distortion in the LINFLUX predictions is due to the numerical inaccuracies associated with computing velocity gradients, whereas LINFLO computes vorticity directly.

8. Numerical Results: Fan Exit Guide Vane

We proceed to consider a more realistic, three-dimensional, unsteady flows; namely, flows through the exit guide vane of the NASA/PW, 22 inch, advanced ducted propulsor (ADP). We will apply the 3D LINFLUX analysis to predict the unsteady pressure responses of this stator blade row to the Fourier components, at one, two and three times the blade passing frequency (BPF), of a rotor wake excitation. The analytical wake excitation is based on velocity measurements taken downstream of the rotor [Pod97]. The results given below stem from a first-time application of the LINFLUX-based unsteady flow model to a realistic wake/blade row interaction. We anticipate that various aspects of this model, particularly those associated with modeling the wake excitation, will be improved with time, and, in the future, the analytical predictions will be compared with experimental measurements for the modal acoustic responses at the exit of the aft duct.

The application of LINFLUX to predict the unsteady aerodynamic response of a blade row to a wake excitation involves the use of four codes: TIGER [SS91], to generate a 3D H-grid; AWAKEN [TE99], to define the steady and unsteady inflow conditions; TURBO [Jan89, JHW92, CW93], to determine the steady background flow; and LINFLUX to determine the linearized unsteady flow. At present, these codes use different forms of the flow variables. As a consequence, the numerical results given below for the steady and unsteady inflow conditions (Figures 33–36) are reported in terms of dimensional flow variables. The steady flow properties at inlet and exit, given in Figure 39, are shown in terms of the non-dimensional flow variables used in TURBO, which are described in §8.2. All other results for the FEGV are given in terms of the non-dimensional variables used for the LINFLUX output, which are described in §2.

A schematic of the advanced ducted propulsor is shown in Figure 30. The upstream fan rotor consists of 18 blades which rotate clockwise, when viewed from upstream, at 5,425 rpm. The radius of the fan is 11 in. and the nominal blade chord measured over the outer span is 3.5 in. The fan exit guide vane (FEGV), cf. Figure 31, is placed at an axial distance from the rotor-tip trailing edge to the stator-tip leading edge of 5.3 in. It consists of 45 blades, which are twisted, bowed, flared at the tip, and have rounded leading and trailing edges. The FEGV resides in an aft duct which has variable inner and outer radii. The chord, c^*, and axial chord, c^*_{ax}, of the stator blades, at midspan, are 1.666 in. and 1.625 in., respectively. Here, the chord is taken as the linear distance between the leading- and trailing-edge points at blade midspan, and it is the reference length used in non-dimensionalizing the flow variables.

We have introduced several geometric simplifications to the actual FEGV configuration to allow for the application of the TURBO and LINFLUX analyses. In particular, a wedge-shaped, trailing-edge section, approximately 0.2 in. long, has been added to the original vane geometry, so that the analytical vanes close in sharp trailing edges. This modification is needed to eliminate trailing-edge separations from the TURBO predictions for the zeroth-order background flow, thereby allowing the TURBO calculations to converge to a steady solution. In addition, we have modified the aft-duct geometry, to provide a duct with inlet and exit sections of constant inner and outer radii, as required by the assumptions used in developing the LINFLUX far-field eigenanalysis.

The computational domain prescribed for the TURBO and LINFLUX, FEGV calculations extends axially 0.893 in. upstream and 2.707 in. downstream from the blade leading edge at midspan. The axial extent of this domain was kept short deliberately, so that a relatively dense mesh could be applied to resolve the near-field unsteady flow. The constant radii duct sections at inlet and exit extend almost to the blade row and have inner and outer radii of $r_H^* = 5.810$ in. and $r_D^* = 11.410$ in. at inlet; and of $r_H^* = 6.426$ and $r_D^* = 11.288$ in. at exit. In terms of dimensionless coordinates, say $\xi = \xi^*/c^*$ and $r = r^*/c^*$, the key axial coordinates, are $\xi = -0.536$ at the computational inlet boundary, $\xi = 0$ at the midspan leading-edge point, $\xi = 0.975$ at the midspan blunt trailing-edge point, $\xi = 1.085$ at the sharp trailing-edge point, and $\xi = 1.625$ at the computational exit boundary. The inner and outer radii, $r = r^*/c^*$, are 3.487 and 6.849 for the inlet duct section, and $r_H = 3.857$ and $r_D = 6.776$ for the exit section.

The TIGER grid generator [SS91] has been used to define a three-dimensional H-grid, for the FEGV steady and unsteady flow calculations. The numerical results, reported herein, were determined on an H-grid, consisting of 151 axial, 47 tangential and 25 radial surfaces (165,600 cells). This grid extends axially from $\xi = -0.536$ to $\xi = 1.625$ with 47 axial surfaces positioned upstream of the blade row, 83 intersecting the modified blade surfaces and 21 positioned downstream of the blade row. Axial grid surfaces are clustered near blade leading and trailing edges; circumferential surfaces, near the blade suction and pressure surfaces; and radial surfaces, near the tip.

The H-grid used for the FEGV calculations is shown at 4 radial stations; one near the hub, one near midspan, one near seventy five percent span, and one near the tip, in Figure 32. The LINFLUX near-field, finite-volume solutions, computed on this grid, are coupled to far-field acoustic eigensolutions, which have been determined on a radial grid consisting of 36 points clustered near the hub and duct walls. For the unsteady flows under consideration, the unsteady wake excitations are prescribed at inlet, and convected and nearly convected disturbances are convected numerically through the computational outflow boundary.

8.1 Rotor-Exit/Stator-Inlet Conditions

As in §6, we assume that the flow downstream of the fan can be represented as the sum of a circumferentially averaged steady flow in which the velocity, entropy and pressure vary only with radius, and a first-order perturbation in which the velocity is aligned with the mean flow velocity and the density and pressure are negligible. Thus, for the present example, the velocities $\tilde{\mathbf{V}}'$ and $\mathbf{V}'$ in §6 are measured relative to the fan rotor, $N' = N_B$ is the number of fan blades and $\mathbf{\Omega}_R = \mathbf{\Omega}'$ is the angular velocity of the fan rotor.

The absolute steady and unsteady velocities, cf. equations (6.6) and (6.7), at the stator inlet are given by

$$\mathbf{V}^{\text{abs}} = V^{\text{rel}}\mathbf{e}_T + \Omega_R r\mathbf{e}_\theta = V_\xi \mathbf{e}_\xi + (V_\theta^{\text{rel}} + \Omega_R r)\mathbf{e}_\theta \tag{8.1}$$

and

$$\tilde{\mathbf{v}}^{\text{R}} = \tilde{v}^{\text{R}}\mathbf{e}_T = \sum_{n=1}^{\infty} \text{Re}\left\{v_n^{\text{R}}\mathbf{e}_T \exp[in(\kappa_\xi \xi - N_B\theta^{\text{abs}} + N_B\Omega_R t)]\right\} \tag{8.2}$$

where $\omega^{\text{abs}} = N_B\Omega$, $\kappa_\xi = -(\omega - r^{-1}N_B V_\theta^{\text{abs}})/V_\xi$ and $\sigma = -2\pi N_B/N_V$ are the fundamental

frequency, in the stator frame, axial wave number and interblade phase angle, respectively, of the excitation. The flow velocities $V^{\rm rel}$ and $v_n^{\rm R}$ can be determined from a Fourier analysis of the rotor exit velocity, cf. (6.2) and (6.3). The state vector for the rotor wake excitation is $\tilde{\mathbf{u}}^T = \bar{\rho}[0,\ 0,\ \tilde{v}_\theta^{\rm R},\ \tilde{v}_\xi^{\rm R}, V_\theta^{\rm abs}\tilde{v}_\theta^{\rm R} + V_\xi v_\xi^{\rm R}]$. This vector describes a first-order unsteady flow in which mass, axial and circumferential momenta and energy, are conserved. In general, radial momentum will be conserved only if $V_\theta^{\rm abs} = 0$.

The inflow conditions used for the FEGV steady and unsteady flow calculations are based on measurements of the rotor exit flow [Pod97]. In particular, circumferentially-averaged values of the total temperature and total pressure were determined at 10 radial stations in an axial measurement plane 3.720 in. downstream of the rotor-tip trailing edge, and LDV measurements of the rotor exit velocity were taken at 29 radial and 51 circumferential locations in an axial plane 2.650 in. downstream of the rotor-tip trailing edge. This data was post-processsed to provide the analytical inflow conditions; i.e., the radial distributions of the circumferentially-averaged absolute total temperature, total pressure, and flow angle for the TURBO steady flow calculation, and the Fourier amplitudes, $v_n^R(r)$, of the perturbation velocity for the LINFLUX linearized unsteady flow calculation.

In particular, a modification of the mean inflow data near the blade tip was introduced, as part of the post-processing, to eliminate inviscid separation from the TURBO solution for the nonlinear background flow through the FEGV. In addition, the experimental perturbation velocity was modified to remove endwall and splitter affects, and to make the analytical description consistent with the unsteady, far-field, formulation currently used in the LINFLUX analysis. Finally, empirical correlations for wake diffusion as a function of axial distance [MG84] were applied to estimate the strength of the viscous wake excitation, at the FEGV leading edge, from the measurements taken upstream.

Curves describing the radial distributions of the measured and derived absolute total temperature, $T_T^{\rm abs}$, total pressure, $P_T^{\rm abs}$, and flow angle, $\Omega^{\rm abs} = \tan^{-1}\left(V_\theta^{\rm abs}/V_\xi\right)$, at the rotor exit (stator inlet) for the flight condition of interest, i.e., landing approach, are shown in Figure 33. Here, the derived or analytical total temperature distribution has been obtained by fitting a straight line through the data, and is in very close agreement with the experimental distribution. The analytical $P_T^{\rm abs}$ distribution has been obtained by assuming isentropic flow, evaluating the entropy, $S_{\rm Ref}$, at the reference point $r_{\rm Ref} = 5.752$, in terms of the measured total temperature and total pressure at $r_{\rm Ref}$, and calculating the analytic $P_T^{\rm abs}$ distribution in terms of the analytic $T_T^{\rm abs}$ distribution and $S_{\rm Ref}$. Finally, the analytical flow angle distribution has been determined by fitting a linear curve through the corresponding measured data for $r_H < r \leq 6.282$ and continuing this into a quadratic curve for $6.282 \leq r < r_D$. The coefficients in the quadratic fit were adjusted to reduce the inflow angle near the blade tip and thereby avoid separation in the TURBO solution. The analytical distributions in Figure 33 have been used as inlet conditions for the TURBO calculation of the FEGV steady background flow. The analytic static pressure at the stator exit was prescribed such that the analytical and experimental mass-flow rates would be the same.

Although the inflow conditions $(T_T^{\rm abs}, P_T^{\rm abs}, \Omega^{\rm abs})$ prescribed for the TURBO calculation are in reasonably good agreement with the corresponding experimental values there are significant differences between the calculated and measured mean flow velocities, particularly over the outer span of the blade. The circumferentially-averaged, measured, relative and absolute, velocities at the rotor exit (stator inlet) are shown in Figure 34, along with the

values determined from the TURBO steady flow calculation. The reasons for the differences between the measured and calculated steady inflow velocities are not clear at this time, and will be investigated in more detail in our future work. Important contributors to these differences may be representing the measured incoming viscous flow by an analytical inviscid flow, ignoring radial velocities that may be present in the actual flow, and requiring that the calculated inviscid mass flow agree with that observed in the experiment.

The analytical wake excitation model has been derived from the NASA LDV velocity data in the following manner. The first step is to determine the wake velocity perturbation by subtracting the circumferentially-averaged, measured, relative velocity from the actual measured relative velocity. This yields perturbation velocity components, that are parallel, $\tilde{v}_T\ (r, \theta, \xi_{\rm E})$, and normal, $\tilde{v}_N\ (r, \theta, \xi_{\rm E})$, to the circumferentially averaged flow velocity at the velocity measurement plane, $\xi = \xi_E$. The radial component of the wake perturbation velocity was not measured and the normal component was generally found to be small. Thus, in keeping with the assumptions used in developing the wake excitation model of §6, the normal and radial components of the analytic wake perturbation velocity are assumed to be negligible, and the parallel component of the measured perturbation velocity is used to construct the analytic wake excitation velocity. Moreover, this parallel velocity component is assumed to act in the direction of the analytic mean relative velocity at the inlet to the stator, which is indicated by the dashed lines in Figure 34.

In analytical models of wake excitations, e.g., see [MG84], the wakes are assumed to be aligned with the relative mean, rotor-exit velocity and to be identical from blade to blade. At each radial station, the perturbation velocity, $\tilde{v}_T(N)$, in a single wake, is assumed to be symmetric relative to a wake centerline at $N = 0$, and the velocity distribution, $\tilde{v}_T(N)$, is described in terms of the wake edge, $\tilde{v}_{T,e}$, and centerline, $\tilde{v}_{T,\rm min}$, velocities and a shape function $f(N)$ which depends on the wake half-width. In the present study, a symmetric, hyperbolic-secant, velocity profile was fitted to the experimental data for $\tilde{v}_T(r, \theta, \xi_E)$ to provide an analytical description of the wake velocity distribution at each radial station. The wake velocity defect, $\tilde{v}_{T,e} - \tilde{v}_{T,\rm min}$ and wake half-width, were then determined as functions of radius, based on the fitted velocity profiles. The radial and circumferential distributions of the fitted wake velocity field were then modified near the hub and near the tip in an attempt to remove the end wall and splitter effects (cf. Figure 30) contained in the data, and to provide a more or less classical wake excitation over the entire span of the stator blades.

Finally, the diffusion of the viscous wakes, as they proceed downstream, is taken into account by applying empirical relations [MG84] for the behavior of the wake velocity defect and half-width, and hence, that of the analytic wake velocity profiles, with streamwise distance. The viscous wake velocity profiles at the stator leading-edge, are used to determine the Fourier amplitudes, v_n^R, in equation (8.2), of the wake excitation velocity. Thus, the Fourier components of the inviscid wake excitation, prescribed at the computational inlet plane of the FEGV, are based on the estimated, viscous, rotor-wake, velocity distribution at the FEGV leading edge.

Circumferential distributions, over 3 rotor passages, of the analytic, rotor-wake, velocity at the stator midspan leading-edge, as determined from the NASA data and the post-processing procedure outlined above, are shown in Figure 35. In this figure, θ_G is the angular gap of the rotor and, for clarity, the velocity profiles at each radius are offset by $r/r_D \times 10^3$. The curves in Figure 35 indicate only the behavior of the coefficient, $\tilde{v}_T$, of the tangential

perturbation velocity, but there are also strong changes in the direction of this velocity, $e_T(r)$, with radius, as indicated by the dashed curve for Ω^{rel} in Figure 34. The circumferential locations at which the minimum wake velocity occurs also vary significantly along the span. The velocity profiles in Figure 35 indicate that the wake velocity defect and half-width are relatively large near the hub and tip, and much smaller over the blade midspan region. However, this may be due to endwall effects that are still present in the post-processed wake velocity data.

Radial distributions of the amplitude, $|v_n^R|$, and phase, $\arg(v_n^R)$, of the first five Fourier components of the analytic wake excitation velocity at the stator leading edge are shown in Figure 36. The amplitudes of the Fourier excitations decrease with increasing n. Also, the amplitude of the first harmonic excitation shows a very strong radial variation over the span. The higher harmonics show much smaller variations in amplitude. Large phase variations also occur over the span; e.g., a phase variation of approximately 200 deg for the first harmonic and approximately 360 deg for the second harmonic. The higher harmonics show even greater phase variations. As will be seen subsequently, the strong radial variations in the magnitude, direction and phase of the analytic rotor wake excitation lead to rather complicated unsteady pressure responses for the FEGV blade row.

8.2 Steady Background Flow

The steady background flow through the fan exit guide vane (FEGV) has been calculated by applying the TURBO, nonlinear, 3D, Euler analysis on the computational grid illustrated in Figure 32. The radial distributions of absolute total temperature, absolute total pressure and absolute flow angle, indicated by the dashed curves in Figure 33, were prescribed at the computational inlet plane, located at $\xi = \xi_- = -0.536$, and the static pressure at the hub was specified at exit, $\xi = \xi_+ = 1.626$, such that the calculated mass-flow rate matched that measured in the NASA Lewis experiment. Prior to the present study, the TURBO analysis lacked the capability of modeling a radially varying, swirling, inlet flow. Thus, this capability was implemented into TURBO to permit the FEGV steady flow calculation.

Selected results from the TURBO steady flow calculation are shown in Figures 37 through 39. The computed results indicate that the isentropic absolute Mach number varies from 0.27 at the hub to 0.38 at the tip, at inlet, and from 0.20 at the hub to 0.36 at the tip, at exit. The steady pressure field is shown, at four spanwise stations, in Figure 37. The steady pressure variations generated by the stator die out within short axial distances upstream and downstream from the blade row. As a result, the pressure is nearly constant at the computational inlet and exit boundaries. Because of steady blade loading, there is a small pressure rise across the FEGV blade row. The steady pressure distributions over the suction and pressure surfaces of the modified blade, i.e., the original blade with a wedge-shaped trailing-edge section added, are shown in Figure 38 and indicate an increase in blade loading from hub to tip. The peak isentropic Mach numbers at the four radial stations indicated in Figure 38 are approximately 0.38 at J=4, 0.46 at J=10, 0.51 at J=16 and 0.53 at J=22. The spanwise location of the peak Mach number moves aft with increasing radius, but, generally lies in the vicinity of $\xi = 0.25 c_{ax}$.

Radial distributions of the steady density, pressure, and velocity at the computational inlet and exit planes for the FEGV are shown in Figure 39, where the scalings for the non-

dimensional flow variables differ from those used elsewhere in this report. In particular the results given in Figure 39 are based on the scalings used in the TURBO code, where the density is scaled by the standard atmospheric density, $\rho^*_{\text{Std}} = 0.0764$ lb$_m$/ft^3; pressure, by the standard pressure, $P^*_{\text{Std}} = 2,116.2$ lb$_f$/ft^2; and velocity by the standard sound speed $A^*_{\text{Std}} = 1,116.8$ ft/sec. In TURBO, the standard density and sound speed are determined from the standard atmospheric pressure and temperature, $T^*_{\text{Std}} = 519°$R, using the perfect gas relations.

The results in Figure 39 also indicate that the steady pressure and density at the inlet and exit of the FEGV are nearly constant, and there is a slight rise in pressure and density across the blade row. The axial velocities at inlet and exit show fairly similar radial distributions. The circumferential velocity distributions indicate that the steady inlet flow is one of almost constant swirl, and the loading on the stator blade row essentially removes swirl from exit flow. Finally, the inlet flow has, by prescription, zero radial velocity, but the exit flow has a small radial velocity component, even though the prescribed exit section of the annular duct has constant inner and outer radii.

8.3 Unsteady Response Predictions

We have determined the unsteady pressure responses of the FEGV to rotor wake excitations at 1, 2, and 3BPF. Since these excitations are highly dependent on radius (e.g., see Figures 34 and 35), it can be difficult to evaluate or interpret the predictions for the associated unsteady pressure responses. Therefore, we have also determined response predictions for test excitations at 1, 2, and 3BPF. The test excitations occur at the same frequencies and interblade phase angles as the corresponding wake excitations, but their Fourier amplitudes, $|v^R_n|$, cf. equation (8.2), are proportional to the relative mean rotor exit flow speed, and they have a constant phase at $\xi = 0$. In particular, for the test excitations, we have set $v^R_n = -|\mathbf{V}^{\text{rel}}|, 0$.

The LINFLUX unsteady response calculations for the FEGV were performed on the $151 \times 47 \times 25$ mesh illustrated in Figure 32. These calculations required from 3,000 to 4,000 pseudo time steps to converge. This translates to approximately 15 to 20 CPU hours for a converged solution on an IBM 3CT Workstation. No difficulties were experienced in determining the eigenvalues and radial shapes of the far-field, propagating and least-damped, modal acoustic responses. The results for the 1 and 2BPF test and wake excitations are shown in Figures 40 through 50. Although similar results have been determined for the 3BPF excitations, these have not been included in the present report.

The axial eigenvalues of the far field acoustic disturbances associated with the unsteady flows, at 1 and 2BPF, through the FEGV are shown in Figures 40 and 41, respectively, where we have labeled the circumferential and radial mode orders of the propagating and least-damped acoustic response disturbances. The LINFLUX far-field eigenanalyses were applied to determine the lowest-order radial acoustic modes for $m = -2, -1, 0, 1, 2$. As for the 3D SC10 examples, some highly-attenuated modes are filtered out by the far-field analyses, but such modes should have little impact on the overall unsteady solutions.

For the 1BPF excitation (see Figure 40) all acoustic response modes attenuate, with the least damped response modes occurring at $m, \mu = 0, 0$. The axial eigenvalues of the upstream and downstream traveling 0,0 acoustic responses are $\chi^-_{0,0} = 2.991 + 0.192i$ and

$\chi^+_{0,0} = -2.828 + 0.490i$, respectively. For the 2BPF excitation (Figure 41) three modes, i.e., the 1,0, 1,1, and 1,2 modes, propagate upstream and two, the 1,0 and 1,1 modes, propagate downstream. The axial wave numbers of the 1,0 , 1,1 and 1,2 upstream propagating modes are 3.623, 2.972 and 2.217, respectively; those of the 1,0 and 1,1 downstream propagating modes are -1.347 and -0.732. The least damped upstream and downstream attenuating response modes at 2BPF have axial eigenvalues $\chi^-_{1,3} = 1.565 + 0.831i$ and $\chi^+_{1,2} = -1.085 + 0.762i$.

The radial shapes of the propagating acoustic modes for the 2BPF excitation are shown in Figure 42. The propagating response disturbances occur in the $m = 1$ circumferential mode, i.e., at $\bar{m} = -2N_B + N_V = 9$ or $\sigma_1 = 2\pi\bar{m}/N_V = 72\,\text{deg}$. Hence, they repeat nine times around the stator blade row and travel circumferentially counter to the direction of rotor rotation, i.e., in the negative θ-direction. Each of the propagating modes, including those at $\mu = 0$, show a strong spanwise pressure variation.

If we introduce the circumferential linear wave number $\kappa_\eta = \bar{m}/r$, then the LINFLUX far-field solutions for the 2BPF excitations indicate that the upstream 1,0 response wave has a wavelength $\lambda = 2\pi/(\kappa_\xi^2 + \kappa_\eta^2)^{1/2}$, that depends on radius and varies from 1.412 at the hub to 1.630 at the tip. This disturbance travels upstream and counter to the direction of rotor rotation at an angle $\alpha = 180\,\text{deg} - \tan^{-1}(\kappa_\eta/\kappa_\xi)$ that varies from 144.5 deg from the positive ξ-axis at the hub to 160.1 deg at the tip. The upstream propagating 1,1 and 1,2 waves have longer wave lengths and lower propagation angles. The wave length of the downstream propagating 1,0 wave varies from 2.332 at the hub to 3.320 at the tip and travels away from the blade row and opposite to the direction of rotor rotation at an angle of 60 deg at the hub and 44.6 deg at the tip from the axial flow direction.

The unsteady blade surface pressure distributions resulting from the 1BPF test and wake excitations are shown in Figures 43 and 44, respectively. The surface pressure responses are given for the modified FEGV blades, which extend from the blade leading edge near $\xi = 0$ to the sharp trailing edge near $\xi = 1.11c_{ax}$. The trailing edge of the original (blunt-edged) blade occurs near $\xi = c_{ax}$. The amplitude of the test excitation varies with radius like $|\mathbf{V}^{rel}|$, and is, therefore, high near the tip, cf. Figure 34, and the phase is constant at $\xi = 0$. This test excitation gives rise to a surface-pressure response having the very reasonable spanwise behavior, shown in Figure 43.

The amplitude of the 1BPF wake excitation is high at the hub and at the tip, cf. Figure 36, and this excitation undergoes a large phase variation of approximately 200 deg, along the span. As a result, the predicted surface pressure responses, shown in Figure 44, have a more complicated spanwise behavior than those for the 1BPF test excitation. In addition, since the wake excitation occurs at a much smaller amplitudes than the test excitation, the resulting unsteady pressure responses have much smaller amplitudes than those for the test excitation.

The FEGV unsteady pressure fields resulting from the 1BPF test and wake excitations are shown in Figures 45 and 46, where we have plotted the out-of-phase, $Im\{p\}$, unsteady pressure contours. The excitations at 1BPF produce attenuating acoustic responses upstream and downstream of the blade row. Thus, the pressure variations at the computational inlet and exit boundaries, shown in Figures 45 and 46, are due to acoustic responses that die out with increasing axial distance from the blade row. For the test excitation, the amplitudes of the least-damped 0,0 acoustic response modes, at the computational inlet and

exit boundaries, are 0.181 and 0.0797, respectively. The next strongest mode at inlet is the 1,0 mode, with amplitude 0.112. The next strongest mode at exit is the 0,1 mode, which has an amplitude of 0.020. The pressure contours for the test excitation show moderate radial pressure variations at inlet, particularly from blade midspan to tip, and much smaller variations at exit.

For the wake excitation, the two strongest modes at inlet are again the 0,0 and 1,0 modes, which have amplitudes of 0.00476 and 0.00341. The two strongest modes at the exit are also the 0,0 and 1,0 modes which have amplitudes of 0.00224 and 0.00064. Again, the unsteady pressure contours indicate small pressure perturbations at inlet, particularly in the vicinity of 75% span, and very small perturbations at exit. Note that, near the tip (i.e., at $J = 22$), the unsteady pressure contours at inlet show a spurious behavior. This could be due to prescribing a wake excitation that is not a solution of the linearized unsteady equations. Since the near field solver takes this prescribed inflow information and enforces the conservation laws, a spurious pressure behavior may be introduced into the unsteady solution, just downstream of the inlet boundary.

The unsteady surface pressure responses of the FEGV to the 2BPF test and wake excitations are shown in Figures 47 and 48. The complex amplitude, v_2^R, of the 2BPF test excitation is $v_2^R = -|\mathbf{V}^{\mathrm{rel}}|, 0$. The surface pressure responses to this excitation generally show reasonable spanwise trends, with the pressure responses occurring at smaller amplitudes than those for the 1BPF test excitation. The 2BPF wake excitation occurs at amplitudes that vary from 10% at the hub, to 3% at midspan to 7% at the tip of the relative fan exit velocity, $|\mathbf{V}^{\mathrm{rel}}|$, and the phase varies from approximately +180 deg at the hub to −180 deg at midspan to +180 deg at the tip. The real and imaginary surface pressure responses, shown in Figure 48, to this highly three-dimensional excitation show no discernable simple trend, but instead relatively complex radial variations, which are primarily due to the large phase variations in the unsteady excitation. One disconcerting feature of the results for the 2BPF excitations are the relatively large differences that occur in the out-of-phase pressures across the sharp trailing edge of the FEGV blade.

The unsteady pressure fields associated with the 2BPF test and wake excitations are illustrated in Figures 49 and 50, respectively, where, again, we have plotted the contours of the out-of-phase pressure. In each case, there are three propagating acoustic response modes (the 1,0 , 1,1 and 1,2 modes) upstream and two (1,0 and 1,1) downstream. Various characteristics of these response disturbances; i.e., wave numbers, wave lengths, and propagation angles, are determined by the LINFLUX far-field analysis and have been discussed above. For the 2BPF test excitation, the LINFLUX predictions for the amplitudes of the upstream propagating modes are 0.183, 0.062 and 0.101. Those for the downstream propagating modes are 0.292 and 0.101. Thus, the 1,0 modes are dominant, especially downstream. The amplitudes of the attenuating acoustic response modes, at the computational inlet and exit boundaries, are small. Although there is some spurious pressure behavior at inlet, the contours for the test excitation in Figure 49 give a clear indication of the 1,0 modes near the inlet and exit boundaries. These results also indicate that the far-field 1,0 acoustic responses are relatively weak at the hub and strong at the tip — a behavior in accordance with the radial shapes of the 1,0 acoustic modes shown in Figure 42.

The LINFLUX unsteady pressure responses to the 2BPF wake excitation, depicted in Figure 50, indicate complicated acoustic responses, both upstream and downstream of the

blade row. Here, the amplitudes of the upstream propagating 1,0, 1,1 and 1,2 acoustic response modes at inlet are 0.00136, 0.000702, and 0.00255, and the least-damped (1,3) mode has an amplitude of 0.00192. At exit, the propagating (1,0) and (1,1) modes have amplitudes of 0.00210 and 0.00237, and the least-damped (1,2) mode has an amplitude of 0.00191. Thus, there is no clearly dominant acoustic mode at the computational inlet or exit boundary. In addition, as indicated in Figure 42, the modes that contribute to the pressure responses at inlet and exit reach their maximum amplitudes at different radial locations. Such features make it difficult to interpret the far-field acoustic responses from the contours plotted in Figure 50. An additional complication is the spurious pressure behavior at the computational inlet boundary, which is due, possibly, to errors introduced in specifying the wake excitation.

In the present study on the FEGV, we have limited the axial extent of the computational domain to ensure an adequate resolution of the near-field flow within available computer memory resources. In the future, it would be interesting to repeat the FEGV calculations on an H-mesh that extends further upstream and downstream from the blade row to see if a better resolution and understanding of the unsteady response far upstream and far downstream of the FEGV can be achieved. On an extended mesh, the attenuating acoustic response disturbances would occur at reduced amplitudes, or essentially disappear, at the computational inlet and exit boundaries, and the spurious behavior, associated with the wake excitation, might be seen to die out within short axial distances from the inlet boundary. As part of the present study, we have performed the FEGV, 1, 2 and 3BPF, response calculations on a $141 \times 33 \times 25$ H-mesh having the same axial extent as the $151 \times 47 \times 25$ H-mesh shown in Figure 32. The coarse and fine mesh results for the 1 and 2BPF excitations were found to be in very good agreement, but the results for the 3BPF excitation, although qualitatively similar, show small to moderate quantitative differences. Thus, at least for the 1 and 2BPF excitations, it should be possible to construct a mesh that extends further from the blade row, which still has the density required to accurately resolve the unsteady flows through the FEGV.

9. Concluding Remarks

LINFLUX, a linearized unsteady aerodynamic analysis, is being developed for turbomachinery aeroelastic and aeroacoustic response predictions. This analysis is based on the linearized Euler equations; a near-field, implicit, wave-split, finite-volume analysis for the unsteady perturbations of arbitrary mean flows; and far-field eigenanalyses for the unsteady perturbations of fully-developed, axisymmetric mean flows. The near-field numerical model is based on the scheme used in the nonlinear Euler/Navier-Stokes analysis, TURBO [Jan89, JHW92, CW93]. The far-field analyses, which are coupled to the near-field analysis at the computational inflow and outflow boundaries, allow incoming aerodynamic excitations to be prescribed, and outgoing disturbances to pass through these boundaries without spurious reflection. To date, this theoretical effort has been focused on formulating the linearized inviscid unsteady aerodynamic equations and the near- and far-field solution procedures, implementing these models into two- and three-dimensional unsteady aerodynamic codes, and validating and demonstrating these codes via numerical examples.

LINFLUX results for a helical fan and a three-dimensional version of the 10th Standard Cascade (3D SC10), each with a hub to tip ratio of 0.8, have been reported in [MV97, MV98] for unsteady flows driven by prescribed blade motions and by prescribed acoustic excitations at inlet and exit. In each case a nearly two-dimensional excitation was imposed, so that the LINFLUX predictions could be evaluated via comparisons with the predictions of well-known two-dimensional analyses. The numerical results indicate that the 3D LINFLUX code gives accurate aerodynamic response information for acoustically dominated unsteady flows, provided that the grids employed are of sufficient density and grid lines are clustered near the blade surfaces. In particular, the LINFLUX blade-surface response predictions show reasonable radial trends, and the results at midspan are in very good agreement with 2D predictions based on the Smith [Smi72] and the LINFLO [Ver93] analyses. Moreover, the axial eigenvalues, radial shapes and amplitudes of the propagating and least damped, far-field, modal acoustic disturbances are predicted accurately.

Under the present effort, we have applied the 3D LINFLUX analysis to vortically-excited, unsteady, subsonic flows through rotor and stator blade rows. The rotor is the 3D SC10 studied in [MV97, MV98], and the stator is the exit guide vane of the NASA/P&W 22 inch Advanced Ducted Propulsor [Neu97, Pod97]. The unsteady flows are excited by prescribed vortical disturbances at inlet, which model wake excitations originating from an adjacent upstream blade row. The results for the 3D SC10 have been determined in an effort to validate the LINFLUX code for simple, three-dimensional, wake/blade-row interactions; those for the fan exit guide vane (FEGV), to demonstrate the application of LINFLUX to a realistic wake/blade-row interaction. In the future, the predicted acoustic response at the exit of the FEGV will be compared, on a mode by mode basis, with experimental data taken at NASA Lewis Research Center.

The 3D SC10 consists of 24 blades which rotate within a cylindrical annular duct of constant hub and tip radii. The mean flow at inlet is uniform in the absolute frame, and thus, vortical excitations can be represented as pure axial velocity disturbances that are convected by the mean flow. Such disturbances can be prescribed as exact solutions of the linearized far-field equations. We have considered fundamental vortical or wake excitations

coming from upstream stators consisting of $N_V = 6, 12$ and 18 blades and have presented LINFLUX results for the axial eigenvalues and radial eigenmodes of the far-field acoustic response, the unsteady pressures acting on a blade surface, the unsteady pressure field, and the amplitudes of the modal acoustic responses that occur far upstream and far downstream of the blade row.

The LINFLUX predictions for the 3D SC10 blade-surface pressures show reasonable spanwise trends, and those at midspan are in very good agreement with the predictions of the 2D LINFLO analysis. Small differences exist between the LINFLUX and the LINFLO surface pressures at midspan for the $N_V = 18$ excitation, which are partially due to the influence of 3D acoustic response modes that are not determined by a 2D analysis. The predicted 3D and 2D pressure fields at blade midspan are also in good agreement, as are the amplitudes of the propagating acoustic response disturbances that occur at $N_V = 18$.

The fan exit guide vane consists of 45 blades. This stator blade row resides in an aft duct of variable inner and outer radii, downstream of a fan rotor consisting of 18 blades. We have applied the LINFLUX analysis to predict the unsteady pressure responses of the FEGV to the Fourier components, at one, two and three times the blade passing frequency (BPF), of the rotor wake excitation. The analytical description of the rotor wake excitation is based on velocity measurements taken downstream of the rotor at NASA Lewis Research Center, and a number of simplifying assumptions. The mean or circumferentially-averaged rotor exit flow (stator inlet flow), has significant swirl and radial variation. Therefore, the wake velocity excitation could not be prescribed as a solution of the linearized governing equations. Instead, an approximate, quasi-three-dimensional representation has been employed in which the wake perturbation velocity is assumed to be a convected disturbance that carries no pressure or density. This disturbance satisfies the conservation laws for mass, axial and tangential momenta and energy at each radial station, but it does not conserve radial momentum.

In addition, to the quasi-3D wake approximation a number of liberties had to be taken to analytically model the actual fan-wake/FEGV interaction. These include: geometric changes to the FEGV trailing edge and to the inlet and exit sections of the aft duct; modifications to the rotor exit flow to provide an inlet flow to the stator which would not lead to inviscid separation in the nonlinear background flow through the stator; and modifications to the inlet perturbation velocity to circumvent endwall and splitter effects and provide a more or less classical 2D wake excitation at each radial station. Empirical correlations [MG84] were also applied to estimate the strength and circumferential variation of the viscous wake excitation at the FEGV leading edge, in terms of the measurements taken upstream. Perhaps, the most severe limitation of the analytical model is that the endwall and splitter effects, which are present in the actual flow, are not properly included in the stator inflow excitation model.

We have determined the unsteady pressure responses of the FEGV to rotor wake excitations at 1, 2, and 3BPF. Because of their significant radial variations, these excitations produce very complicated unsteady pressure responses, which make it difficult to assess the performance of the LINFLUX code. Therefore, we have also determined the responses of the FEGV to simpler 1, 2, and 3BPF test excitations. The FEGV response calculations were performed over a computational domain of relatively small axial extent, so that a dense mesh could be applied to resolve the near-field unsteady flow.

We have provided detailed response predictions for the FEGV subjected to the test and rotor-wake excitations at 1 and 2BPF. The acoustic response of the FEGV at 1BPF atten-

uates with axial distance from the blade row; whereas, at 2BPF, three acoustic response modes persist far upstream and two persist downstream. These propagating acoustic responses repeat nine times around the wheel, travel circumferentially counter to the direction of the rotor rotation, and have strong radial variations in amplitude and phase.

The FEGV unsteady pressure responses to the 1 and 2BPF test excitations show reasonable behaviors, both on the blade surfaces and within the fluid domain. The results for the 2BPF test excitation indicate that the $m, \mu = 1, 0$ acoustic responses are dominant far from the blade row, and these responses show up clearly in the predicted pressure field. There is some spurious pressure behavior near the inlet boundary, which is most likely due to errors introduced by simplifying the specification of the vortical excitation.

The highly radially dependent 1 and 2BPF wake excitations produce complicated unsteady pressure responses. In particular, the blade-surface pressures for the 2BPF wake excitation show large spanwise and chordwise variations, and there is no dominant acoustic response mode in either of the far-field regions. Instead, the three upstream propagating and the two downstream propagating acoustic response modes all contribute to the pressure responses at inlet and exit, as do the least-damped acoustic response disturbances. These features make it difficult to understand the far-field responses on the basis of the predicted pressure contours. However, the LINFLUX results for the FEGV, subjected to 1 and 2BPF rotor wake excitations, do give an indication of the complexities associated with the acoustic responses to realistic, three-dimensional, wake/blade-row interactions.

Based upon the numerical results presented to date, it appears that the LINFLUX near- and far-field numerical algorithms are working properly and that these algorithms have been coupled successfully. At present, the major limitations in applying the LINFLUX analysis to study realistic wake/blade-row interactions are the inaccuracies associated with inflow excitation model, and the use of empirical relations to determine the strength and circumferential distribution of viscous wake excitation. Thus, future work should be focused on improving these aspects of a linearized, inviscid, wake/blade-row, interaction model. Improved representations of the inflow excitation will occur with time. The development of a linearized viscous unsteady aerodynamic analysis; e.g. see [HML98], could eliminate the need for an empirical wake model.

Several computational strategies could be investigated to improve the performance of the LINFLUX code. In particular, the implementation of second-order accurate surface boundary conditions would enhance solution accuracy near blade surfaces. Also, the implementation of a convergence acceleration scheme would improve computational efficiency. Finally, the mesh densities required to resolve the unsteady flows associated with wake/blade-row interactions are severe, particularly, for subsonic mean flows, at high Mach numbers, and for unsteady excitations at high reduced frequency. Reduced frequencies on the order of 5 to 50 are typical for wake/blade-row interactions. The meshes required to resolve such flows impose very serious constraints on computer memory. Thus, the development of a parallel version of the LINFLUX code, or indeed, any similar unsteady aerodynamic code, should be considered in future work.

References

[AG98] H. M. Atassi and V. V. Golubev, *Unsteady Disturbances in Swirling Turbomachinery Flows*, Unsteady Aerodynamics and Aeroelasticity of Turbomachines, edited by T. H. Fransson, Kluwer Academic Publishers, 1998, pp. 131–146.

[BH92] T. A. Beach and G. Hoffman, *IGB Grid: User's Manual (A Turbomachinery Grid Generation Code)*, CR 189104, NASA, January 1992.

[Cas83] J. R. Caspar, *Unconditionally Stable Calculation of Transonic Potential Flow through Cascades using an Adaptive Mesh for Shock Capture*, Transactions of the ASME: Journal of Engineering for Power **105** (1983), no. 3, 504–513.

[CW93] J. P. Chen and D. L. Whitfield, *Navier-Stokes Calculations for the Unsteady Flowfield of Multi-stage Turbomachinery*, Paper 93-0676, AIAA 31st Aerospace Sciences Meeting and Exhibit, Reno, Nevada, January 11–14, 1993.

[FV93] T. H. Fransson and J. M. Verdon, *Standard Configurations for Unsteady Flow through Vibrating Axial-Flow Turbomachine Cascades*, Unsteady Aerodynamics, Aeroacoustics and Aeroelasticity of Turbomachines and Propellers, edited by H. M. Atassi, Springer-Verlag, New York, 1993, pp. 859–889.

[HC93a] K. C. Hall and W. S. Clark, *Linearized Euler Predictions of Unsteady Aerodynamic Loads in Cascades*, AIAA Journal **31** (1993), no. 3, 540–550.

[HC93b] D. G. Holmes and H. A. Chuang, *2D Linearized Harmonic Euler Flow Analysis for Flutter and Forced Response*, Unsteady Aerodynamics, Aeroacoustics, and Aeroelasticity of Turbomachines and Propellers, edited by H. M. Atassi, Springer-Verlag, New York, 1993, pp. 213–230.

[HCL94] K. C. Hall, W. S. Clark, and C. B. Lorence, *A Linearized Euler Analysis of Unsteady Transonic Flows in Turbomachinery*, Transactions of the ASME: Journal of Turbomachinery **116** (1994), no. 3, 477–488.

[HL93] K. C. Hall and C. B. Lorence, *Calculation of Three-Dimensional Unsteady Flows in Turbomachinery Using the Linearized Harmonic Euler Equations*, Transactions of the ASME: Journal of Turbomachinery **115** (1993), no. 4, 800–809.

[HML98] D. G. Holmes, B. E. Mitchell, and C. B. Lorence, *Three-Dimensional Linearized Navier-Stokes Calculations for Flutter and Forced Response*, Unsteady Aerodynamics and Aeroelasticity of Turbomachines, edited by T. H. Fransson, Kluwer Academic Publishers, 1998, pp. 211–224.

[HSR91] D. L. Huff, T. W. Swafford, and T. S. R. Reddy, *Euler Flow Predictions for an Oscillating Cascade Using a High Resolution Wave-Split Scheme*, Paper 91–GT–198, ASME International Gas Turbine and Aeroengine Congress and Exposition, Orlando, Florida, June 3–6, 1991.

[HV91] K. C. Hall and J. M. Verdon, *Gust Response Analysis for Cascades Operating in Nonuniform Mean Flows*, AIAA Journal **29** (1991), no. 9, 1463–1471.

[Jan89] J. M. Janus, *Advanced 3-D CFD Algorithm for Turbomachinery*, Ph.D. thesis, Mississippi State University, Mississippi State, Mississippi, May 1989.

[JHW92] J. M. Janus, H. Z. Horstman, and D. L. Whitfield, *Unsteady Flowfield Simulation of Ducted Prop-Fan Configurations*, Paper 92–0521, AIAA 30th Aerospace Sciences Meeting and Exhibit, Reno, Nevada, January 6-9, 1992.

[Ker77] J. L. Kerrebrock, *Small Disturbances in Turbomachine Annuli with Swirl*, AIAA Journal **15** (1977), no. 6, 794–803.

[KK93] G. Kahl and A. Klose, *Computation of Time Linearized Transonic Flow in Oscillating Cascades*, ASME Paper 93–GT–269, 38th International Gas Turbine and Aeroengine Congress and Exposition, Cincinnati, Ohio, May 24–27, 1993.

[Kou95] K. A. Kousen, *Eigenmode Analysis of Ducted Flows with Radially Dependent Axial and Swirl Components*, Proceedings of the First Joint CEAS/AIAA Aeroacoustics Conference, *Vol, II* (Munich, Germany), June 12–15 1995, pp. 1085–1094.

[MG84] R. K. Majjigi and P. R Gliebe, *Development of a Rotor Wake/Vortex Model*, CR 174849, NASA, June 1984.

[MG98] J. G. Marshall and M. B. Giles, *Some Applications of a Time-Linearized Euler Method to Flutter & Forced Response in Turbomachinery*, Unsteady Aerodynamics and Aeroelasticity of Turbomachines, edited by T. H. Fransson, Kluwer Academic Publishers, 1998, pp. 225–240.

[MV95] M. D. Montgomery and J. M. Verdon, *A Linearized Unsteady Euler Analysis for Turbomachinery Blade Rows Using an Implicit Wave-Split Scheme*, Unsteady Aerodynamics and Aeroelasticity of Turbomachines, edited by Y. Tanida and M. Namba, Elsevier, Amsterdam, 1995, pp. 143–160.

[MV97] M. D. Montgomery and J. M. Verdon, *A 3D Linearized Unsteady Euler Analysis for Turbomachinery Blade Rows*, CR 4470, NASA, March 1997, prepared under Contract NAS3–26618 for NASA Lewis Research Center.

[MV98] M. D. Montgomery and J. M. Verdon, *A 3D Linearized Unsteady Euler Analysis for Turbomachinery Blade Rows, Part 1: Aerodynamic and Numerical Formulations; Part 2: Unsteady Aerodynamic Response Predictions*, Unsteady Aerodynamics and Aeroelasticity of Turbomachines, edited by T. H. Fransson, Kluwer Academic Publishers, 1998, pp. 427–464.

[Nam87] M. Namba, *Three Dimensional Flows*, AGARD Manual on Aeroelasticity in Axial-Flow Turbomachines, *Vol. 1*, Unsteady Turbomachinery Aerodynamics, edited by M. F. Platzer and F. O. Carta, AGARD AG–298, March 1987.

[Neu97] R. J. Neubert, April 1997, personal communication.

[Pod97] G. Podboy, May 1997, personal communication.

[Roe81] P. L. Roe, *Approximate Riemann Solvers, Parameter Vectors and Difference Schemes*, Journal of Computational Physics **43** (1981), 357–372.

[SLH+94] T. W. Swafford, D. H. Loe, D. L. Huff, D. H. Huddleston, and T. S. R. Reddy, *The Evolution of NPHASE: Euler/Navier-Stokes Computations of Unsteady Two-Dimensional Cascade Flow Fields*, Paper 94–1834, AIAA 12th Applied Aerodynamics Conference, Colorado Springs, Colorado, June 20–23, 1994.

[Smi72] S. N. Smith, *Discrete Frequency Sound Generation in Axial Flow Turbomachines*, R&M 3709, British Aeronautical Research Council, London, England, UK, March 1972.

[Sre96] K. Sreenivas, *Linearized Euler Analysis of Turbomachinery*, Ph.D. thesis, Mississippi State University, December 1996.

[SS91] B. K. Soni and M. H. Shih, *TIGER: Turbomachinery Interactive Grid GenERation*, Proceedings of the Third International Conference on Numerical Grid Generation in CFD (Barcelona, Spain), June 1991.

[TE99] D. A. Topol and W. Eversman, *TFaNS Tone Fan Noise Design/Prediction System, Vol. II: User's Manual*, TFaNS Vers. 1.4, NASA Contractor Report, to be published January 1999.

[TS62] J. M. Tyler and T. G. Sofrin, *Axial Flow Compressor Noise Studies*, SAE Transactions **70** (1962), 309–332.

[UV91] W. J. Usab, Jr. and J. M. Verdon, *Advances in the Numerical Analysis of Linearized Unsteady Cascade Flows*, Transactions of the ASME: Journal of Turbomachinery **113** (1991), no. 4, 633–643.

[VC84] J. M. Verdon and J. R. Caspar, *A Linearized Unsteady Aerodynamic Analysis for Transonic Cascades*, Journal of Fluid Mechanics **149** (1984), 403–429.

[Ver89] J. M. Verdon, *The Unsteady Aerodynamic Response to Arbitrary Modes of Blade Motion*, Journal of Fluids and Structures **3** (1989), no. 3, 255–274.

[Ver93] J. M. Verdon, *Unsteady Aerodynamic Methods for Turbomachinery Aeroelastic and Aeroacoustic Applications*, AIAA Journal **31** (1993), no. 2, 235–250.

[VMK95] J. M. Verdon, M. D. Montgomery, and K. A. Kousen, *Development of a Linearized Unsteady Euler Analysis for Turbomachinery Blade Rows*, NASA CR 4677, prepared under Contract NAS3–25425 for NASA Lewis Research Center, June 1995.

[VTM82] C. S. Ventres, M. A. Theobald, and W. D. Mark, *Turbofan Noise Generation, Volume 1: Analysis*, CR 167952, NASA, July 1982.

[Whi87] D. S. Whitehead, *Classical Two-Dimensional Methods*, AGARD Manual on Aeroelasticity in Axial-Flow Turbomachines, *Vol. 1*, Unsteady Turbomachinery Aerodynamics, edited by M. F. Platzer and F. O. Carta, AGARD AG–298, March 1987.

[WJS88] D.L. Whitfield, J.M. Janus, and L.B. Simpson, *Implicit Finite Volume High Resolution Wave Split Scheme for Solving the Unsteady Three-Dimensional Euler and Navier-Stokes Equations on Stationary or Dynamic Grids*, Report MSSU–EIRS–ASE–88–2, Mississippi State Engineering and Industrial Research Station, 1988.

List of Figures

Figure 1. Rotating axial compressor blade row operating within an annular duct.

Figure 2. Relative frame ($\Omega = -0.1716\mathbf{e}_\xi$), steady flow properties for a steady flow with constant swirl ($T_T^{\text{abs}} = 10.178$, $P_T^{\text{abs}} = 3.039$, $V_\theta^{\text{abs}} = 0.164$) in an annular duct with $r_D = 4.244$ and $r_H/r_D = 0.8$.

Figure 3. Axial eigenvalues, $\chi = \beta + i\kappa_\xi$, for five ($m = -2, \ldots, 2$) circumferential and three ($\mu = 0, 1, 2$) radial modes of acoustic perturbation, at $\omega = 3.089$ and $\sigma = -270$ deg, to a steady background flow with constant swirl ($T_T^{\text{abs}} = 10.178$, $P_T^{\text{abs}} = 3.039$, $V_\theta^{\text{abs}} = 0.164$), occurring within a cylindrical annular duct with $r_D = 4.244$ and $r_H/r_D = 0.8$.

Figure 4. Radial pressure modes, $p^R_{m\mu}(r)$, $m = -2, \ldots, 2$, $\mu = 0, 1, 2$, for an upstream traveling acoustic perturbation, at $\omega = 3.089$ and $\sigma = -270$ deg, to a steady background flow with constant swirl ($T_T^{\text{abs}} = 10.178$, $P_T^{\text{abs}} = 3.039$, $V_\theta^{\text{abs}} = 0.164$), occurring within a cylindrical annular duct with $r_D = 4.244$ and $r_H/r_D = 0.8$.

Figure 5. Axial eigenvalues, $\chi = \beta + i\kappa_\xi$, for five circumferential and three radial modes of acoustic perturbations, at $\omega = 3.089$ and $\sigma = -270$ deg, to steady background flows with solid-body swirl ($T_T^{\text{abs}} = 10.178$, $P_T^{\text{abs}} = 3.039$, $V_\theta^{\text{abs}} = 0.429r$) and free-vortex swirl ($T_T^{\text{abs}} = 10.178$, $P_T^{\text{abs}} = 3.039$, $V_\theta^{\text{abs}} = 0.626/r$), occurring within a cylindrical annular duct with $r_D = 4.244$ and $r_H/r_D = 0.8$.

Figure 6. Nomenclature for wake/blade-row interactions.

Figure 7. LINFLUX computational grid at midspan for the 3D 10th Standard Cascade.

Figure 8. Relative frame steady flow properties far upstream (a) and far downstream (b) of the 3D 10th Standard Cascade ($M_{-\infty}^{\text{abs}} = 0.2868$, $|\Omega| = 0.2145$).

Figure 9. Relative steady isentropic surface Mach number distributions for the 3D 10th Standard Cascade ($M_{-\infty}^{\text{abs}} = 0.2868$, $|\Omega| = 0.2145$): (a) TURBO predictions; (b) TURBO and CASPOF predictions at midspan, $r/r_D = 0.9$.

Figure 10. Steady surface pressure distributions for the 3D 10th Standard Cascade ($M_{-\infty}^{\text{abs}} = 0.2868$, $|\Omega| = 0.2145$): (a) TURBO predictions; (b) TURBO and CASPOF predictions at midspan, $r/r_D = 0.9$

Figure 11. Axial eigenvalues, $\chi = \beta + i\kappa_\xi$, for five circumferential ($m = -2, \ldots, 2$) and three radial ($\mu = 0, 1, 2$) modes of acoustic disturbance far upstream and far downstream of the 3D 10th Standard Cascade for an unsteady flow at $\omega = 1.287$ and $\sigma = -90$ deg ($N_V = 6$).

Figure 12. Axial eigenvalues, $\chi = \beta + i\kappa_\xi$, for five circumferential ($m = -2, \ldots, 2$) and three radial ($\mu = 0, 1, 2$) modes of acoustic disturbance far upstream and far downstream of the 3D 10th Standard Cascade, for an unsteady flow at $\omega = 2.574$ and $\sigma = -180$ deg ($N_V = 12$).

Figure 13. Axial eigenvalues, $\chi = \beta + i\kappa_\xi$, for five circumferential ($m = -2, \ldots, 2$) and three radial ($\mu = 0, 1, 2$) modes of acoustic disturbance far upstream and far downstream of the 3D 10th Standard Cascade, for an unsteady flow at $\omega = 3.861$ and $\sigma = -270\,\text{deg}$ ($N_V = 18$).

Figure 14. Radial pressure modes, $p^R_{m\mu}$, $m = -1, 0, 1$, $\mu = -1, 0, 1$, for the acoustic responses, at $\omega = 1.287$ and $\sigma = -90\,\text{deg}$ ($N_V = 6$), far upstream and far downstream of the 3D 10th Standard Cascade: (———) in-phase (real) component of $p^R_{m\mu}$, (– – –) out-of-phase (imaginary) component of $p^R_{m\mu}$.

Figure 15. Radial pressure modes, $p^R_{m\mu}$, $m = 0, 1, 2$, $\mu = 0, 1, 2$, for the acoustic responses, at $\omega = 2.574$ and $\sigma = -180\,\text{deg}$ ($N_V = 12$), far upstream and far downstream of the 3D 10th Standard Cascade: (———) in-phase (real) component of $p^R_{m\mu}$, (– – –) out-of-phase (imaginary) component of $p^R_{m\mu}$.

Figure 16. Radial pressure modes, $p^R_{m\mu}$, $m = 0, 1, 2$, $\mu = 0, 1, 2$, for the acoustic responses, at $\omega = 3.861$ and $\sigma = -270\,\text{deg}$ ($N_V = 18$), far upstream and far downstream of the 3D 10th Standard Cascade: (———) in-phase (real) component of $p^R_{m\mu}$, (– – –) out-of-phase (imaginary) component of $p^R_{m\mu}$.

Figure 17. Unsteady surface pressure distributions due to the interaction of a vortical gust at $\omega = 1.287$ and $\sigma = -90\,\text{deg}$ ($N_V = 6$) with the 3D 10th Standard Cascade.

Figure 18. Unsteady surface pressure distributions due to the interaction of a vortical gust at $\omega = 2.574$ and $\sigma = -180\,\text{deg}(N_V = 12)$ with the 3D 10th Standard Cascade.

Figure 19. Unsteady surface pressure distributions due to the interaction of a vortical gust at $\omega = 3.861$ and $\sigma = -270\,\text{deg}(N_V = 18)$ with the 3D 10th Standard Cascade.

Figure 20. Unsteady surface pressure distributions at midspan ($r/r_D = 0.9$) due to the interaction of a vortical gust at $\omega = 1.287$ and $\sigma = -90\,\text{deg}(N_V = 6)$, with the 3D 10th Standard Cascade.

Figure 21. Unsteady surface pressure distributions at midspan ($r/r_D = 0.9$) due to the interaction of a vortical gust at $\omega = 2.574$ and $\sigma = -180\,\text{deg}(N_V = 12)$ with the 3D 10th Standard Cascade.

Figure 22. Unsteady surface pressure distributions at midspan ($r/r_D = 0.9$) due to the interaction of a vortical gust at $\omega = 3.861$ and $\sigma = -270\,\text{deg}(N_V = 18)$ with the 3D 10th Standard Cascade.

Figure 23. Contours of the in-phase component of the unsteady pressure at midspan due to the interaction of a vortical excitation at $\omega = 1.287$ and $\sigma = -90\,\text{deg}$ ($N_V = 6$) with the 3D 10th Standard Cascade.

Figure 24. Contours of the in-phase component of the unsteady pressure at midspan due to the interaction of a vortical excitation at $\omega = 2.574$ and $\sigma = -180\,\text{deg}$ ($N_V = 12$) with the 3D 10th Standard Cascade.

Figure 25. Contours of the in-phase component of the unsteady pressure at midspan due to the interaction of a vortical excitation at $\omega = 3.861$ and $\sigma = -270\,\text{deg}$ ($N_V = 18$) with the 3D 10th Standard Cascade.

Figure 26. Relative, isentropic, surface, Mach number distributions for the 2D 10th Standard Cascade ($M_{-\infty} = 0.5$, $\Omega_{-\infty} = 55\,\text{deg}$).

Figure 27. Unsteady surface pressure distributions due to the interaction of a vortical excitation at $\omega = 3.861$ and $\sigma = -270\,\text{deg}$ ($N_V = 18$) with the 2D 10th Standard Cascade.

Figure 28. Contours of the in-phase component of the unsteady vorticity at midspan due to the interaction of a vortical gust at $\omega = 3.861$ and $\sigma = -270\,\text{deg}$ ($N_V = 18$) with the 2D 10th Standard Cascade: (a) LINFLUX calculation on a 281×81 H-mesh; (b) LINFLO calculation.

Figure 29. Contours of the in-phase component of the unsteady pressure at midspan due to the interaction of a vortical gust at $\omega = 3.861$ and $\sigma = -270\,\text{deg}$($N_V = 18$) with the 2D 10th Standard Cascade: (a) LINFLUX calculation on a 281×81 H-mesh; (b) LINFLO calculation.

Figure 30. Schematic of the PW/NASA 22 inch advanced ducted propulsor (ADP).

Figure 31. Fan exit guide vane of the 22 inch ADP.

Figure 32. LINFLUX computational grid, at 4 radial stations, for the fan exit guide vane.

Figure 33. Steady flow properties far upstream of the FEGV.

Figure 34. Absolute and relative frame velocities at the fan exit (FEGV inlet).

Figure 35. Analytic rotor-wake tangential velocity perturbations at FEGV midspan leading-edge plane ($\xi = 0$).

Figure 36. Fourier components of the analytic wake excitation velocity, $\tilde{v}_T$.

Figure 37. FEGV steady pressure field at four radial stations.

Figure 38. FEGV steady surface pressure distributions at four radial stations.

Figure 39. Absolute frame steady flow properties at the computational inlet and exit planes of the fan exit guide vane (FEGV).

Figure 40. Axial eigenvalues, $\chi = \beta + i\kappa_\xi$, of acoustic disturbances far upstream and far downstream of the fan exit guide vane (FEGV) subjected to an unsteady excitation at 1BPF ($\omega = 3.658$ and $\sigma = -144.0\,\text{deg}$).

Figure 41. Axial eigenvalues, $\chi = \beta + i\kappa_\xi$, of acoustic disturbances far upstream and far downstream of the FEGV subjected to an unsteady excitation at 2BPF ($\omega = 7.317$ and $\sigma = -288.0\,\text{deg}$).

Figure 42. Radial pressure modes of the propagating acoustic responses far upstream and far downstream of the FEGV subjected to an unsteady excitation at 2BPF ($\omega = 7.317$ and $\sigma = -288.0$ deg): (———) real part of $p^R_{m\mu}$, (– – –) imaginary part of $p^R_{m\mu}$.

Figure 43. Unsteady surface pressure distributions at 17.8 (J=4), 50.8 (J=10), 76.5 (J=16) and 94.0 (J=22) percent span for the FEGV subjected to the 1BPF test excitation.

Figure 44. Unsteady surface pressure distributions at 17.8 (J=4), 50.8 (J=10), 76.5 (J=16) and 94.0 (J=22) percent span for the FEGV subjected to the 1BPF wake excitation.

Figure 45. Unsteady pressure field, at four radial stations, for the FEGV subjected to the 1BPF test excitation.

Figure 46. Unsteady pressure field, at four radial stations, for the FEGV subjected to the 1BPF wake excitation.

Figure 47. Unsteady surface pressure distributions at 17.8 (J=4), 50.8 (J=10), 76.5 (J=16) and 94.0 (J=22) percent span for the FEGV subjected to the 2BPF test excitation.

Figure 48. Unsteady surface pressure distributions at 17.8 (J=4), 50.8 (J=10), 76.5 (J=16) and 94.0 (J=22) percent span for the FEGV subjected to the 2BPF wake excitation.

Figure 49. Unsteady pressure field, at four radial stations, for the FEGV subjected to the 2BPF test excitation.

Figure 50. Unsteady pressure field, at four radial stations, for the FEGV subjected to the 2BPF wake excitation.

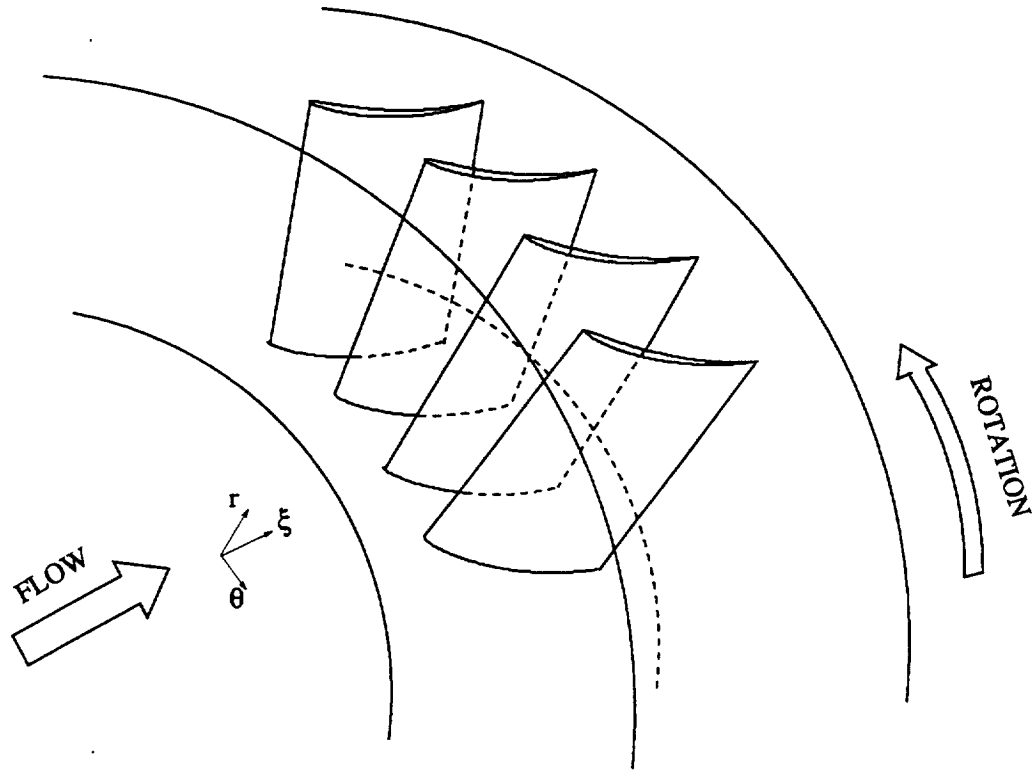

Figure 1: Rotating axial compressor blade row operating within an annular duct.

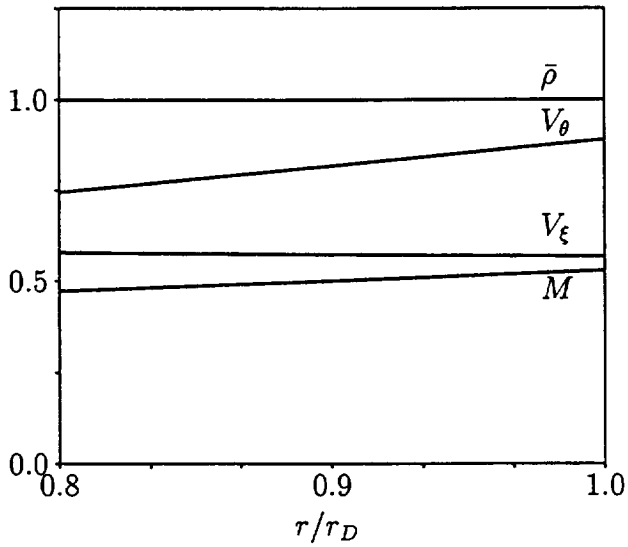

Figure 2: Relative frame ($\Omega = -0.1716\mathrm{e}_\xi$), steady flow properties for a steady flow with constant swirl ($T_T^{\mathrm{abs}} = 10.178$, $P_T^{\mathrm{abs}} = 3.039$, $V_\theta^{\mathrm{abs}} = 0.164$) in an annular duct with $r_D = 4.244$ and $r_H/r_D = 0.8$.

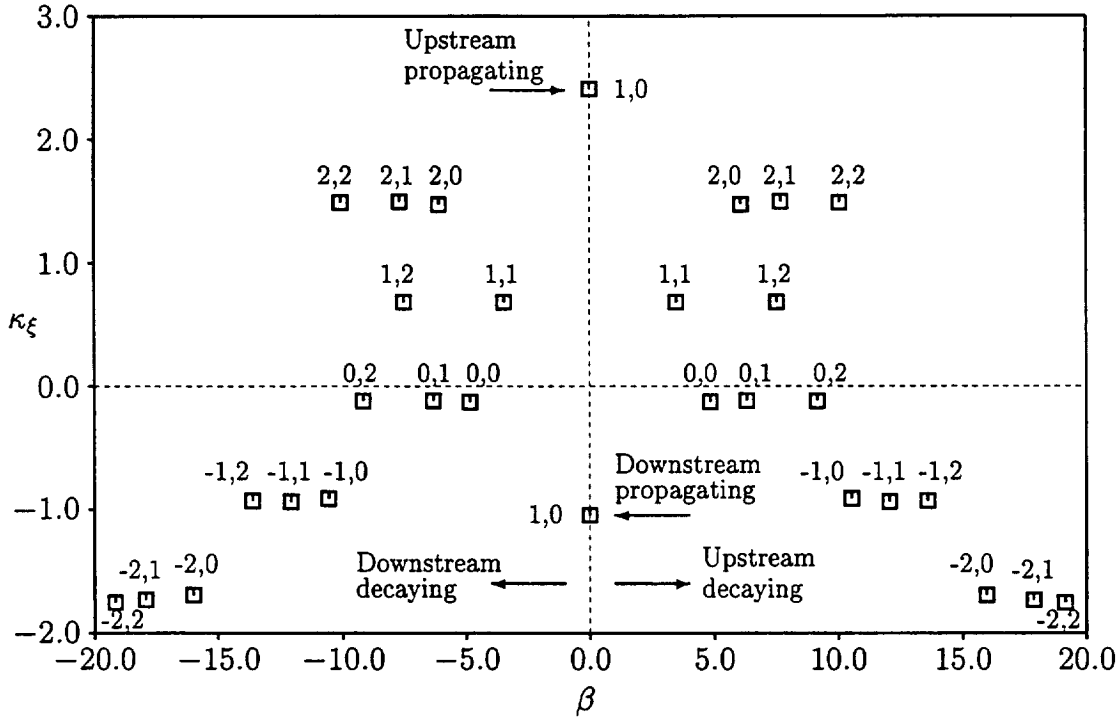

Figure 3: Axial eigenvalues, $\chi = \beta + i\kappa_\xi$, for five ($m = -2, \ldots, 2$) circumferential and three ($\mu = 0, 1, 2$) radial modes of acoustic perturbation, at $\omega = 3.089$ and $\sigma = -270\,\mathrm{deg}$, to a steady background flow with constant swirl ($T_T^{\mathrm{abs}} = 10.178$, $P_T^{\mathrm{abs}} = 3.039$, $V_\theta^{\mathrm{abs}} = 0.164$), occurring within a cylindrical annular duct with $r_D = 4.244$ and $r_H/r_D = 0.8$.

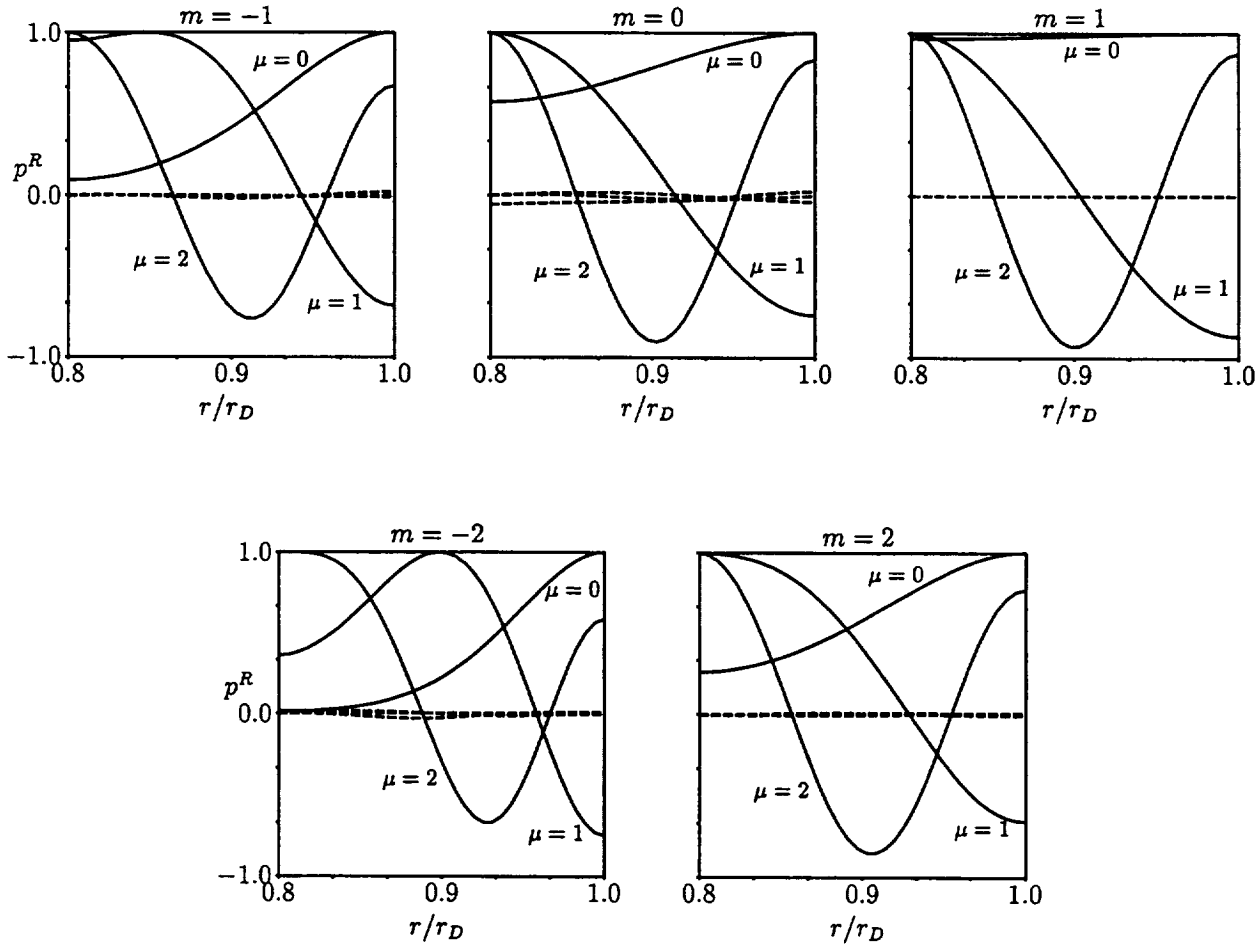

Figure 4: Radial pressure modes, $p^R_{m\mu}(r)$, $m = -2, \ldots, 2$, $\mu = 0, 1, 2$, for an upstream traveling acoustic perturbation, at $\omega = 3.089$ and $\sigma = -270\,\text{deg}$, to a steady background flow with constant swirl ($T_T^{\text{abs}} = 10.178$, $P_T^{\text{abs}} = 3.039$, $V_\theta^{\text{abs}} = 0.164$), occurring within a cylindrical annular duct with $r_D = 4.244$ and $r_H/r_D = 0.8$.

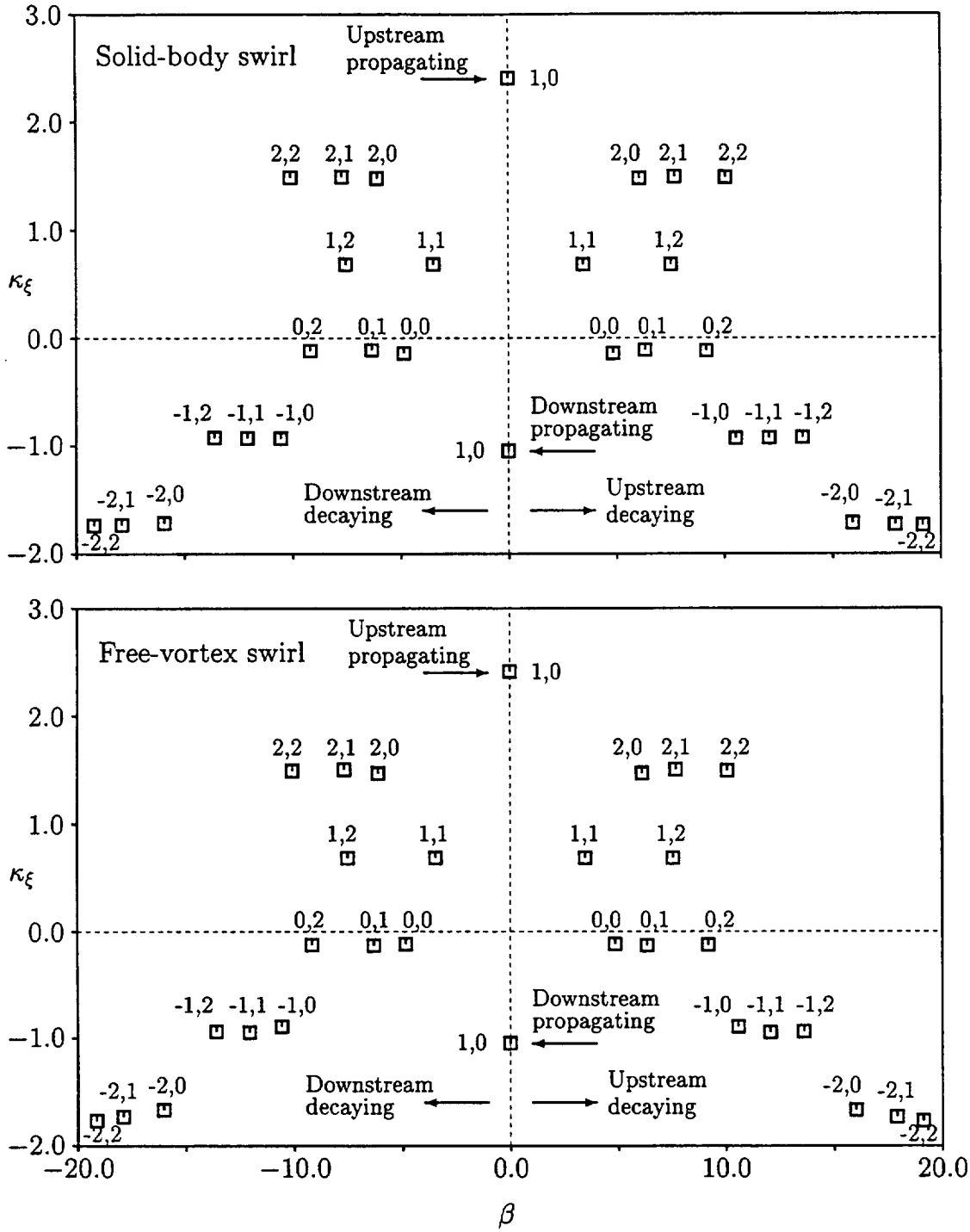

Figure 5: Axial eigenvalues, $\chi = \beta + i\kappa_\xi$, for five circumferential and three radial modes of acoustic perturbations, at $\omega = 3.089$ and $\sigma = -270\,\text{deg}$, to steady background flows with solid-body swirl ($T_T^{\text{abs}} = 10.178$, $P_T^{\text{abs}} = 3.039$, $V_\theta^{\text{abs}} = 0.429r$) and free-vortex swirl ($T_T^{\text{abs}} = 10.178$, $P_T^{\text{abs}} = 3.039$, $V_\theta^{\text{abs}} = 0.626/r$), occurring within a cylindrical annular duct with $r_D = 4.244$ and $r_H/r_D = 0.8$.

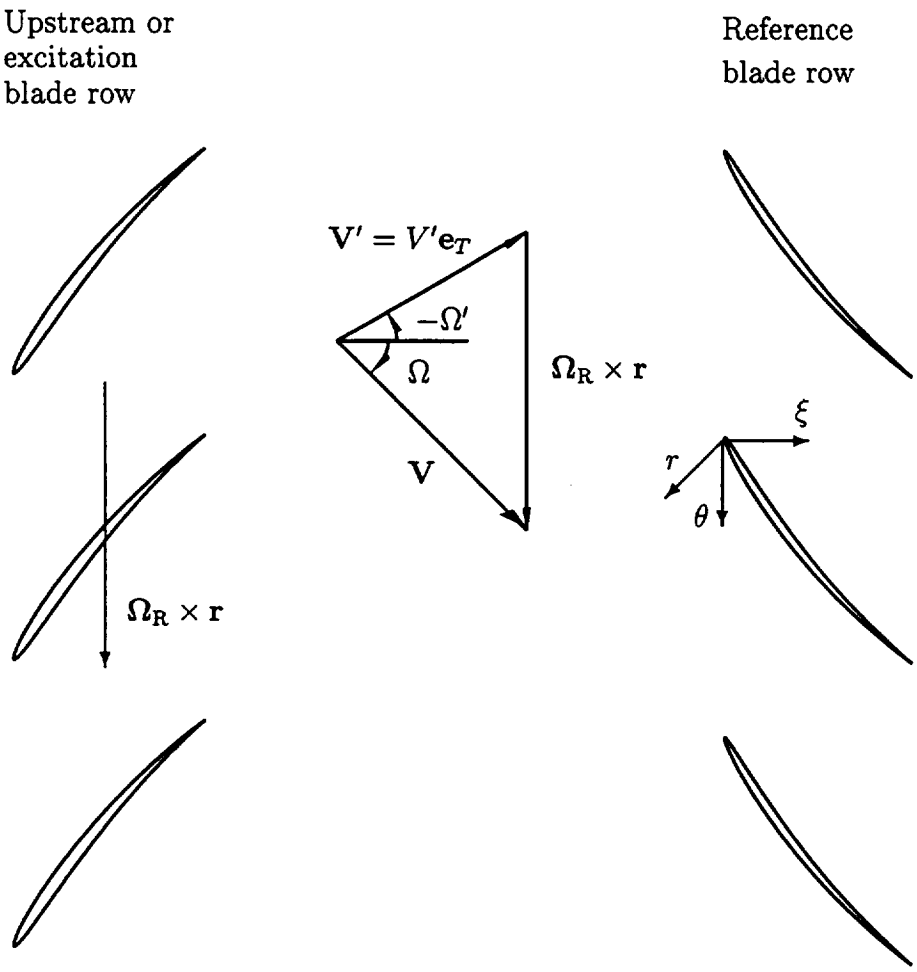

Figure 6: Nomenclature for wake/blade-row interactions.

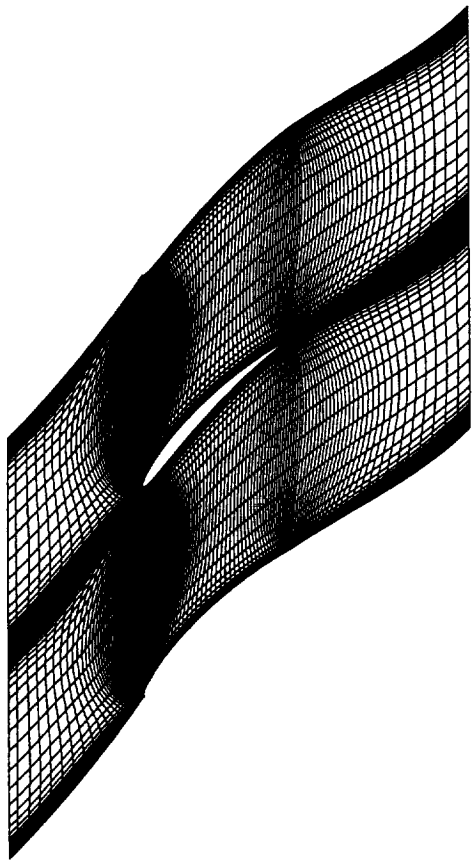

Figure 7: LINFLUX computational grid at midspan for the 3D 10th Standard Cascade.

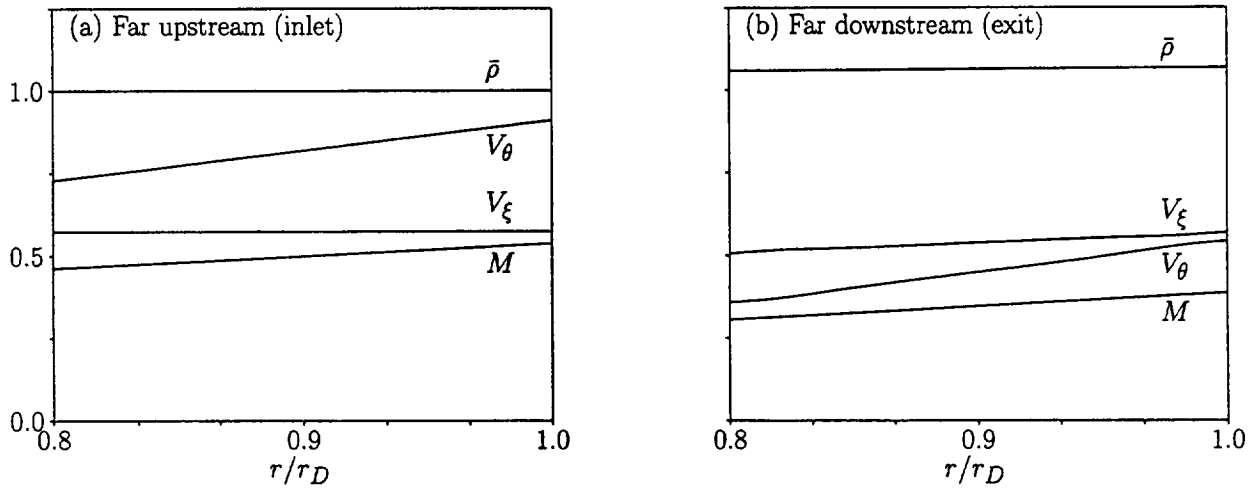

Figure 8: Relative frame steady flow properties far upstream (a) and far downstream (b) of the 3D 10th Standard Cascade ($M^{\text{abs}}_{-\infty} = 0.2868$, $|\Omega| = 0.2145$).

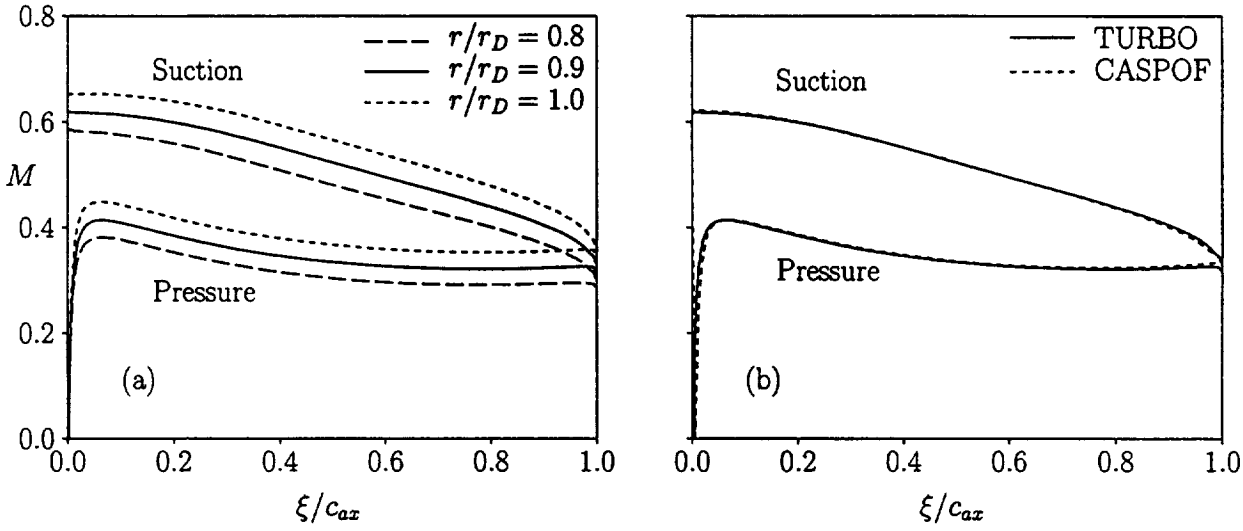

Figure 9: Relative steady isentropic surface Mach number distributions for the 3D 10th Standard Cascade ($M^{abs}_{-\infty} = 0.2868$, $|\Omega| = 0.2145$): (a) TURBO predictions; (b) TURBO and CASPOF predictions at midspan, $r/r_D = 0.9$.

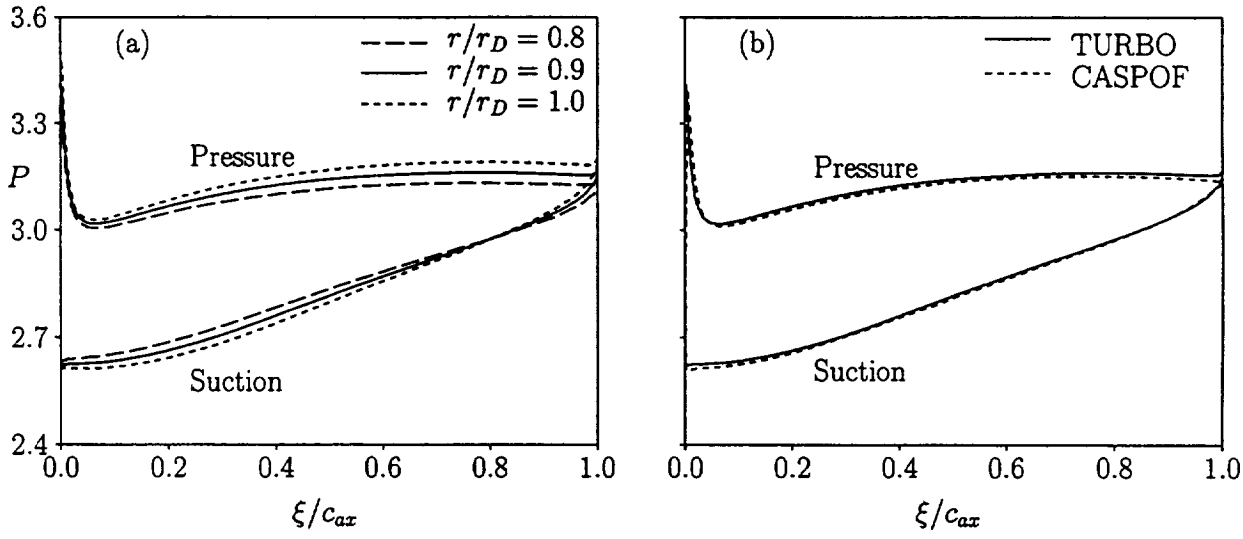

Figure 10: Steady surface pressure distributions for the 3D 10th Standard Cascade ($M^{abs}_{-\infty} = 0.2868$, $|\Omega| = 0.2145$): (a) TURBO predictions; (b) TURBO and CASPOF predictions at midspan, $r/r_D = 0.9$.

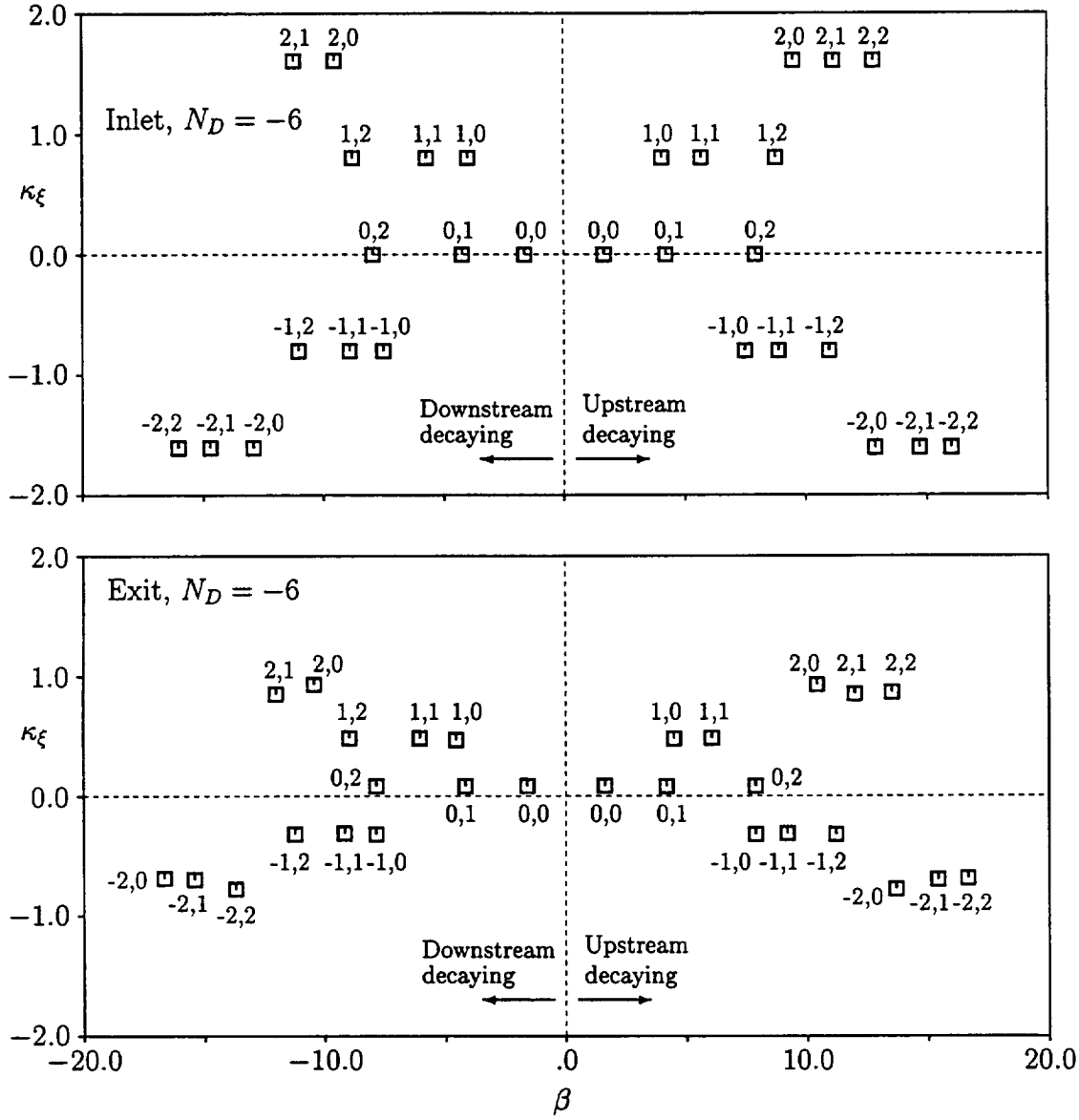

Figure 11: Axial eigenvalues, $\chi = \beta + i\kappa_\xi$, for five circumferential ($m = -2, \ldots, 2$) and three radial ($\mu = 0, 1, 2$) modes of acoustic disturbance far upstream and far downstream of the 3D 10th Standard Cascade for an unsteady flow at $\omega = 1.287$ and $\sigma = -90\,\text{deg}$ ($N_V = 6$).

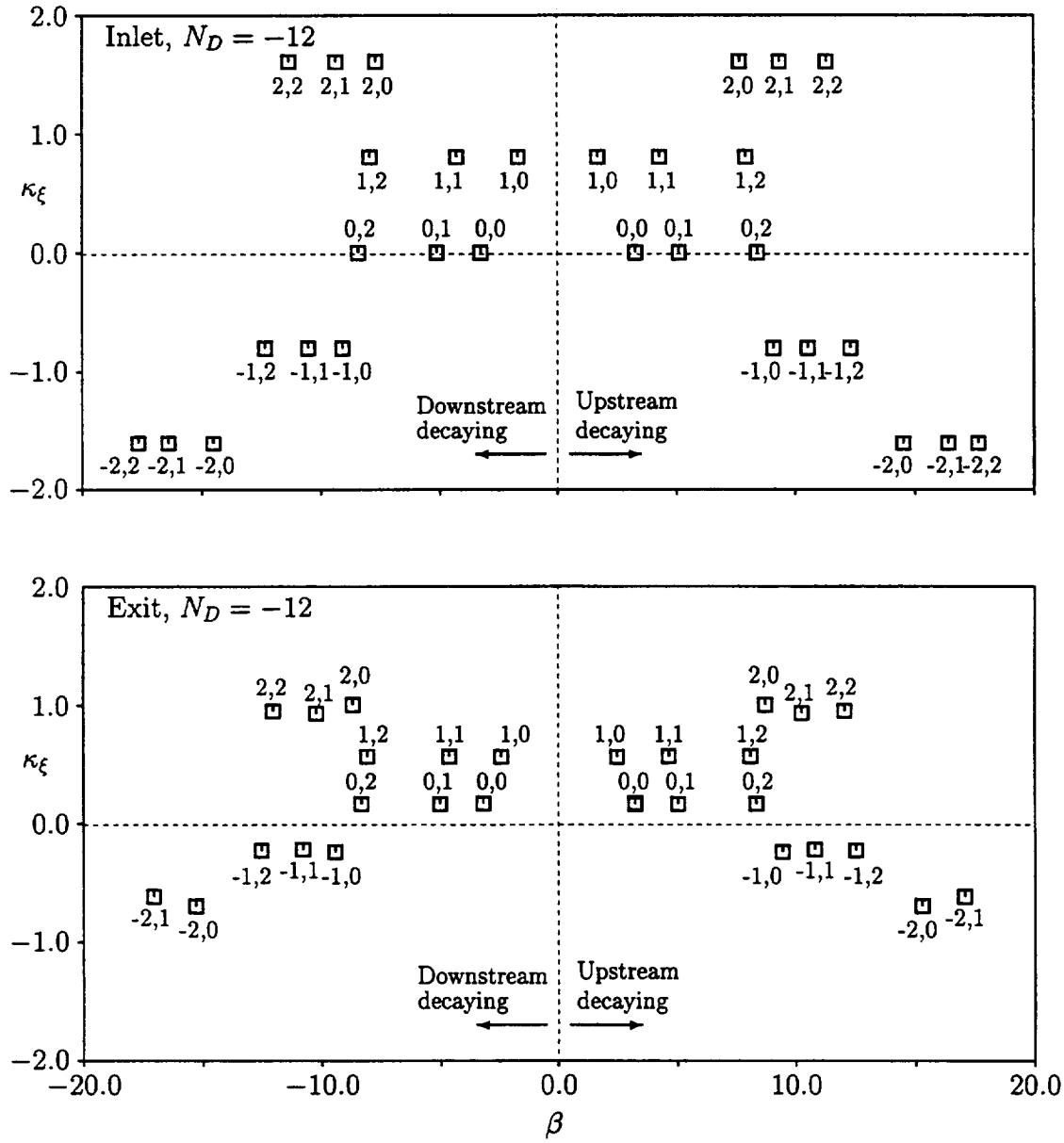

Figure 12: Axial eigenvalues, $\chi = \beta + i\kappa_\xi$, for five circumferential ($m = -2, \ldots, 2$) and three radial ($\mu = 0, 1, 2$) modes of acoustic disturbance far upstream and far downstream of the 3D 10th Standard Cascade, for an unsteady flow at $\omega = 2.574$ and $\sigma = -180$ deg ($N_V = 12$).

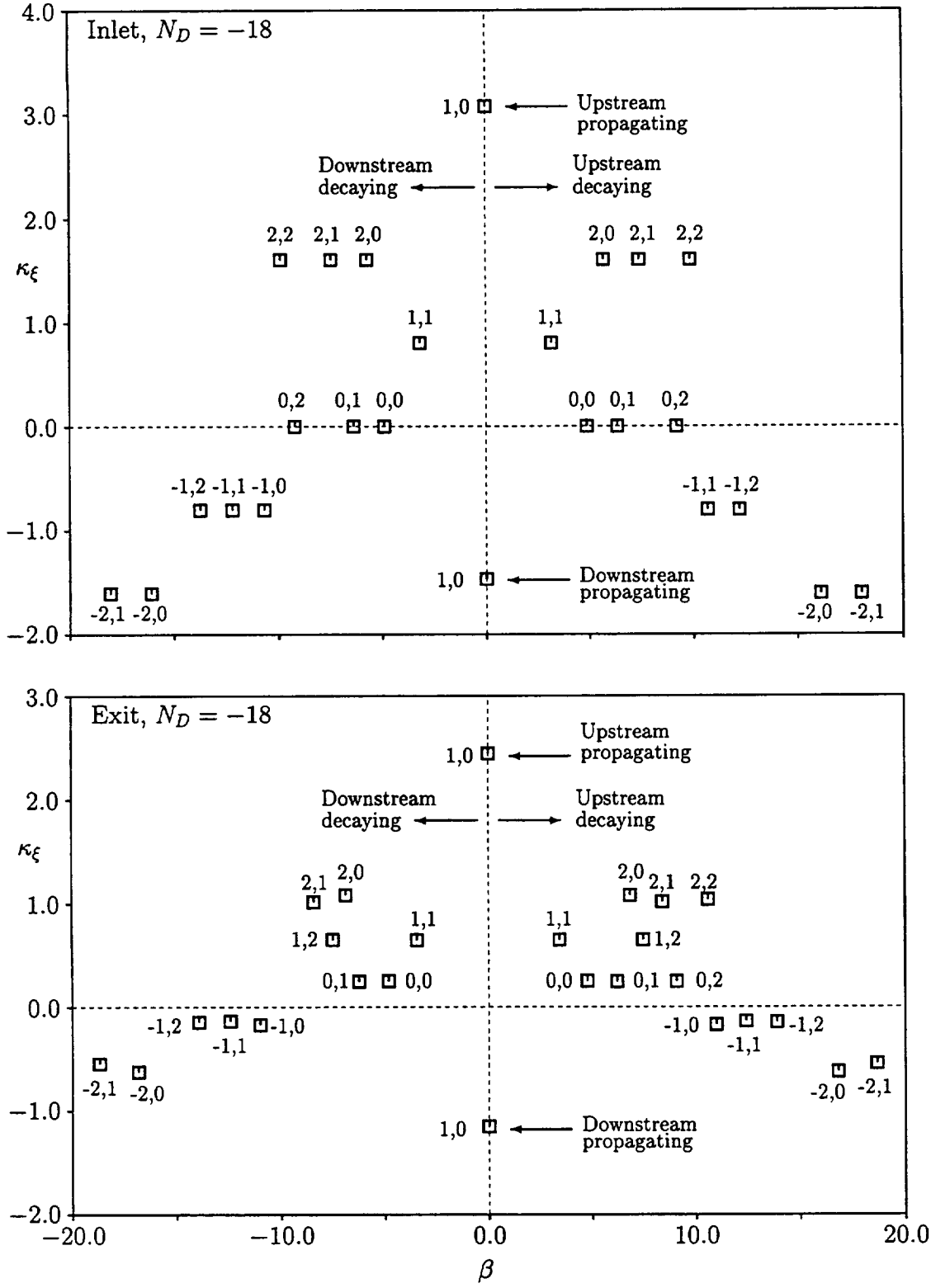

Figure 13: Axial eigenvalues, $\chi = \beta + i\kappa_\xi$, for five circumferential ($m = -2, \ldots, 2$) and three radial ($\mu = 0, 1, 2$) modes of acoustic disturbance far upstream and far downstream of the 3D 10th Standard Cascade, for an unsteady flow at $\omega = 3.861$ and $\sigma = -270\,\text{deg}$ ($N_V = 18$).

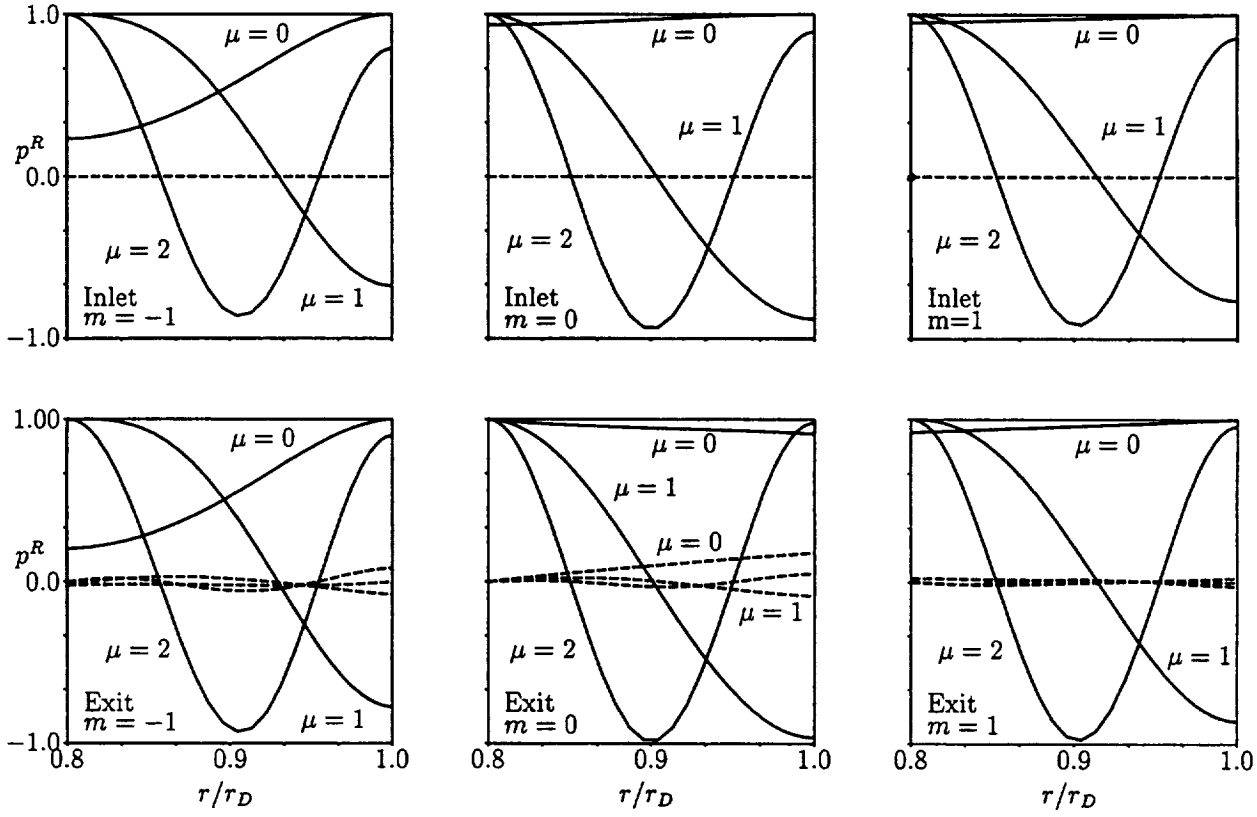

Figure 14: Radial pressure modes, $p^R_{m\mu}$, $m = -1, 0, 1$, $\mu = -1, 0, 1$, for the acoustic responses, at $\omega = 1.287$ and $\sigma = -90\,\text{deg}$ ($N_V = 6$), far upstream and far downstream of the 3D 10th Standard Cascade: (———) in-phase (real) component of $p^R_{m\mu}$, (– – –) out-of-phase (imaginary) component of $p^R_{m\mu}$.

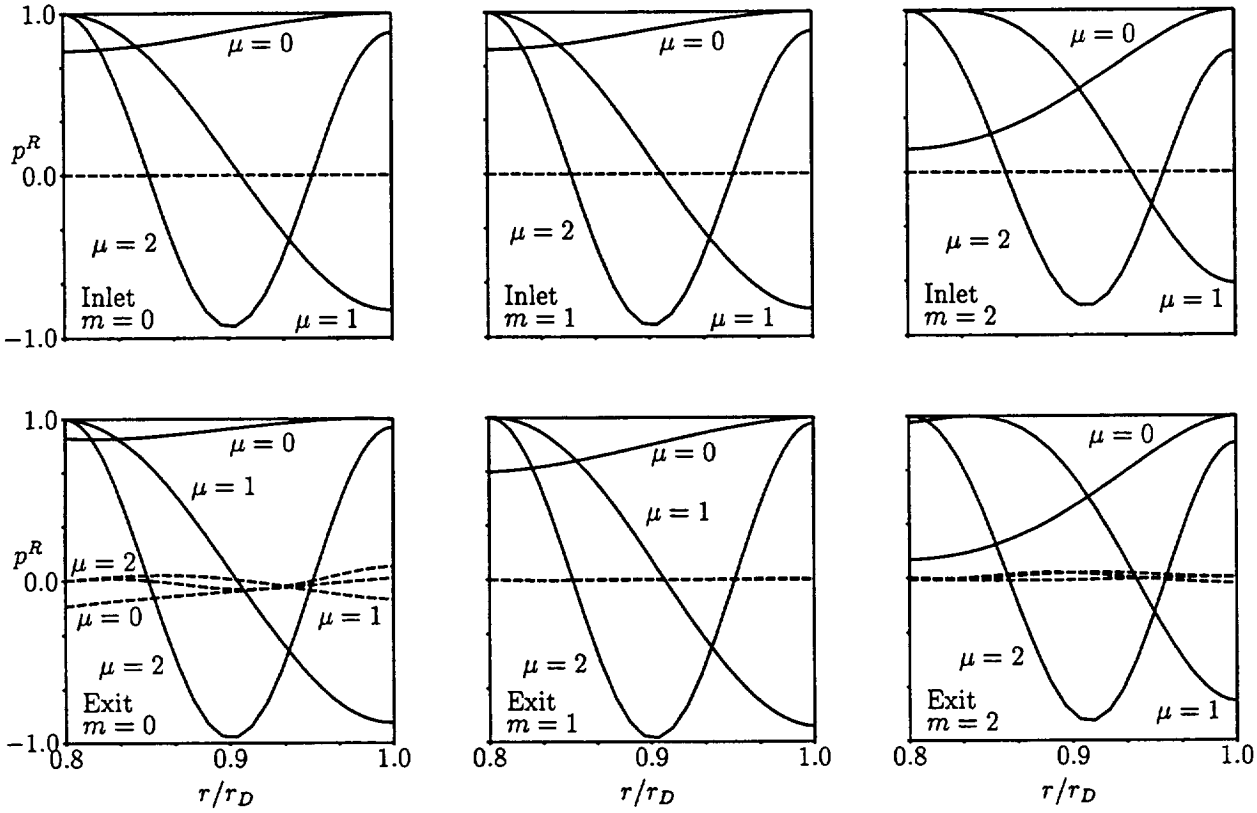

Figure 15: Radial pressure modes, $p^R_{m\mu}$, $m = 0, 1, 2$, $\mu = 0, 1, 2$, for the acoustic responses, at $\omega = 2.574$ and $\sigma = -180\,\text{deg}$ ($N_V = 12$), far upstream and far downstream of the 3D 10th Standard Cascade: (———) in-phase (real) component of $p^R_{m\mu}$, (− − −) out-of-phase (imaginary) component of $p^R_{m\mu}$.

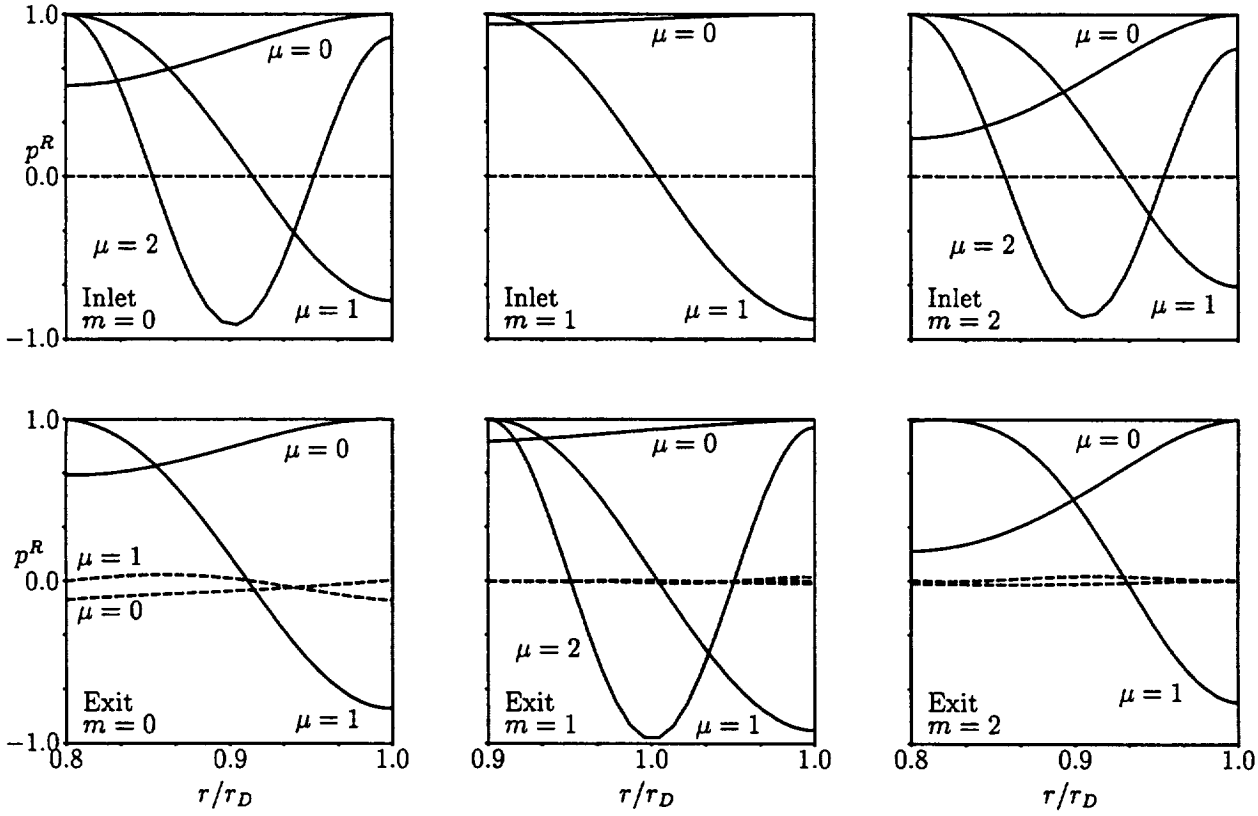

Figure 16: Radial pressure modes, $p^R_{m\mu}$, $m = 0, 1, 2$, $\mu = 0, 1, 2$, for the acoustic responses, at $\omega = 3.861$ and $\sigma = -270\,\text{deg}$ ($N_V = 18$), far upstream and far downstream of the 3D 10th Standard Cascade: (———) in-phase (real) component of $p^R_{m\mu}$, (– – –) out-of-phase (imaginary) component of $p^R_{m\mu}$.

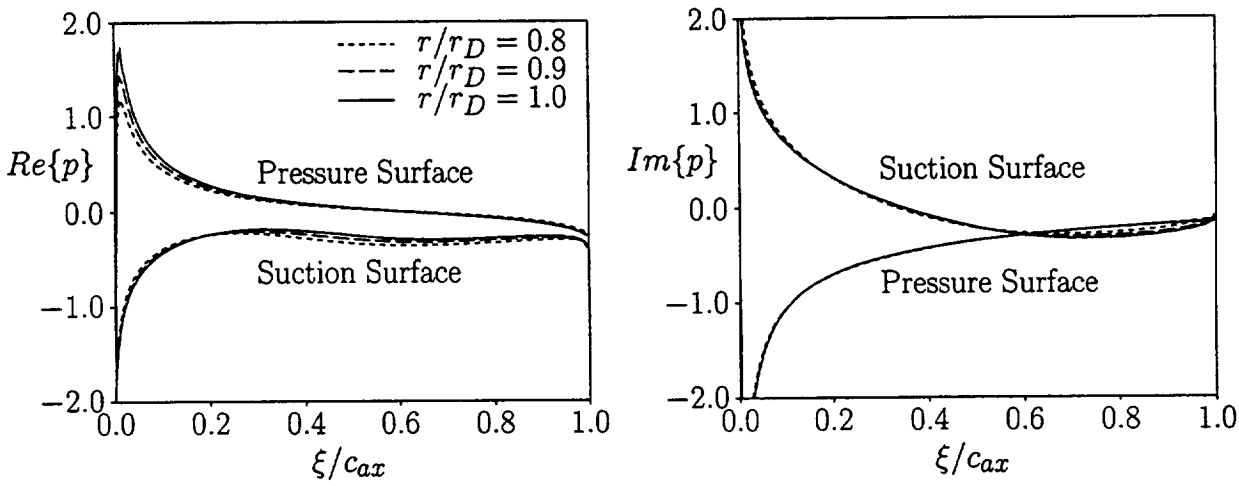

Figure 17: Unsteady surface pressure distributions due to the interaction of a vortical gust at $\omega = 1.287$ and $\sigma = -90\,\text{deg}$ ($N_V = 6$) with the 3D 10th Standard Cascade.

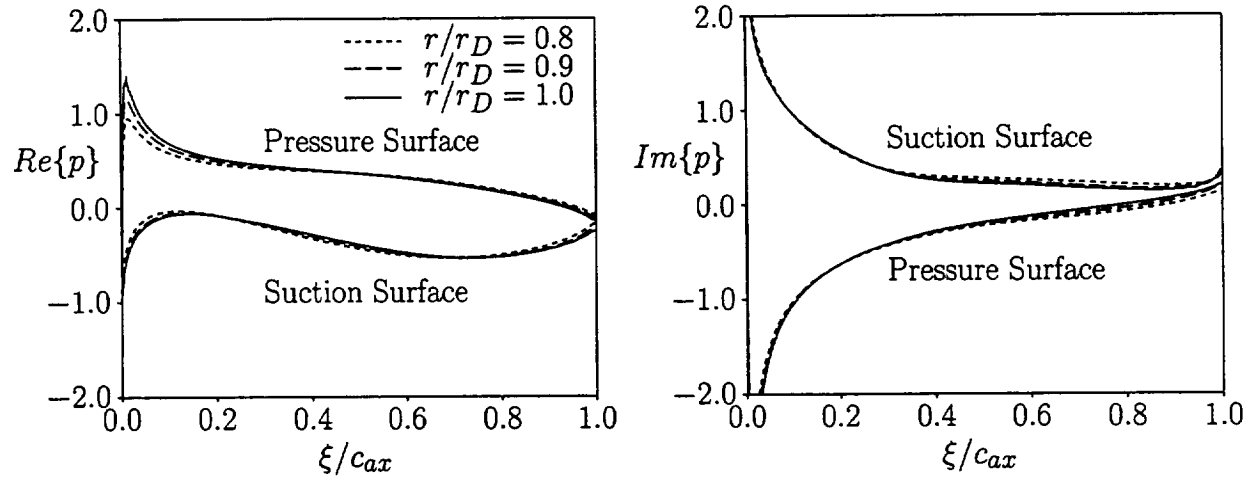

Figure 18: Unsteady surface pressure distributions due to the interaction of a vortical gust at $\omega = 2.574$ and $\sigma = -180\,\text{deg}(N_V = 12)$ with the 3D 10th Standard Cascade.

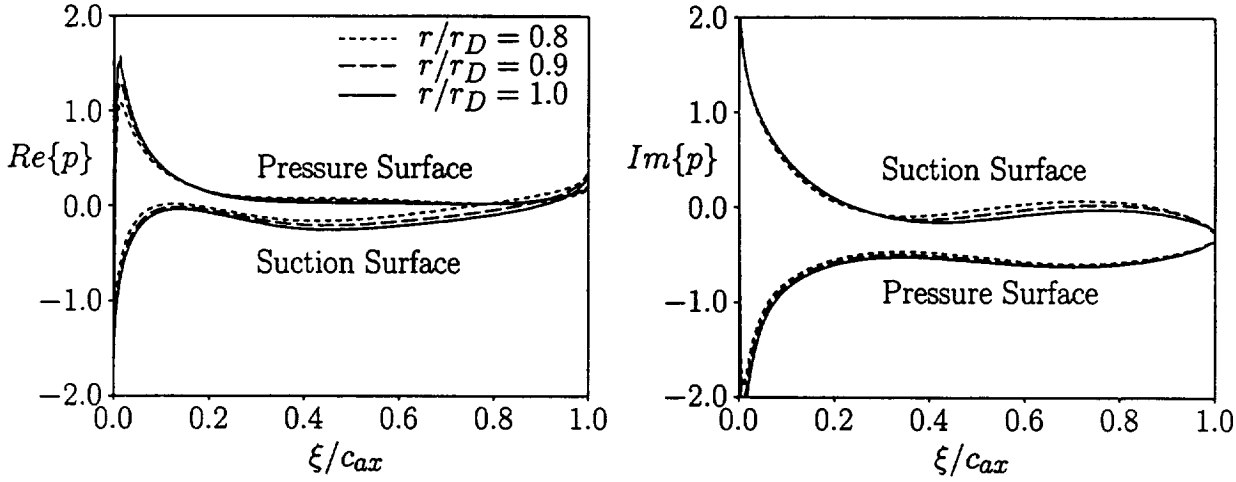

Figure 19: Unsteady surface pressure distributions due to the interaction of a vortical gust at $\omega = 3.861$ and $\sigma = -270\,\mathrm{deg}(N_V = 18)$ with the 3D 10th Standard Cascade.

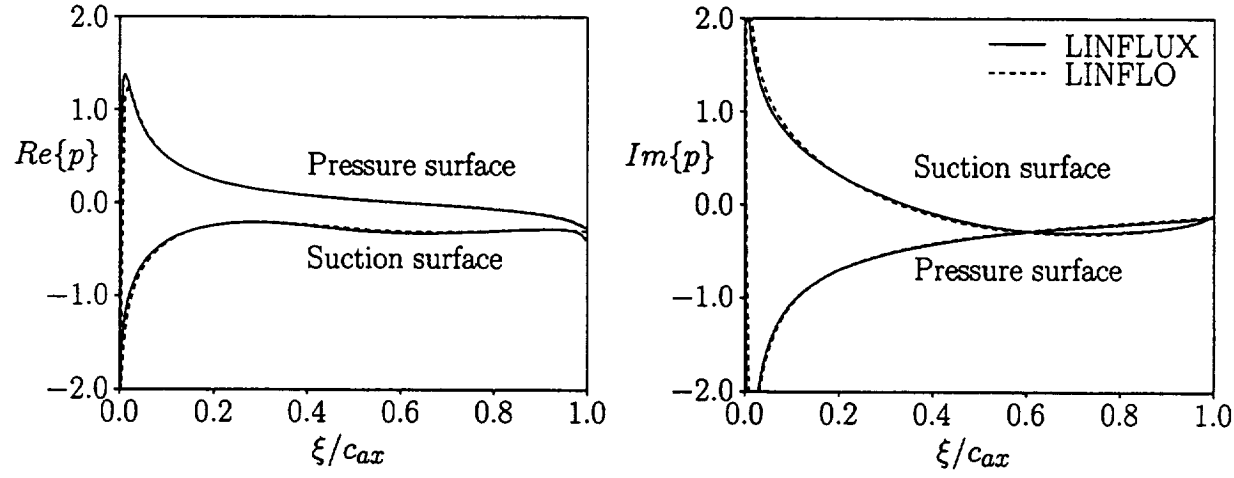

Figure 20: Unsteady surface pressure distributions at midspan ($r/r_D = 0.9$) due to the interaction of a vortical gust at $\omega = 1.287$ and $\sigma = -90\,\mathrm{deg}(N_V = 6)$, with the 3D 10th Standard Cascade.

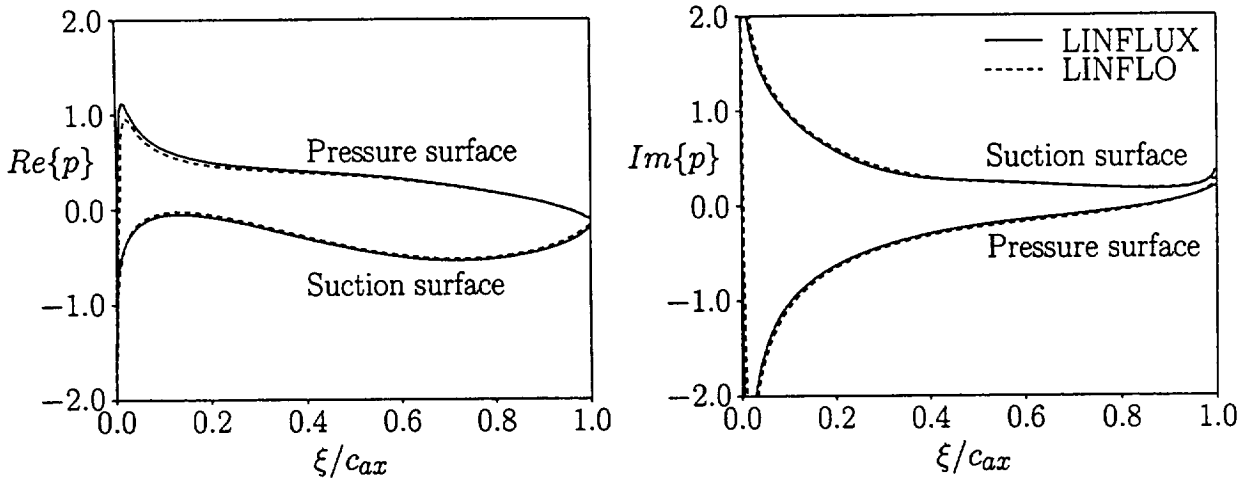

Figure 21: Unsteady surface pressure distributions at midspan ($r/r_D = 0.9$) due to the interaction of a vortical gust at $\omega = 2.574$ and $\sigma = -180\,\mathrm{deg}(N_V = 12)$ with the 3D 10th Standard Cascade.

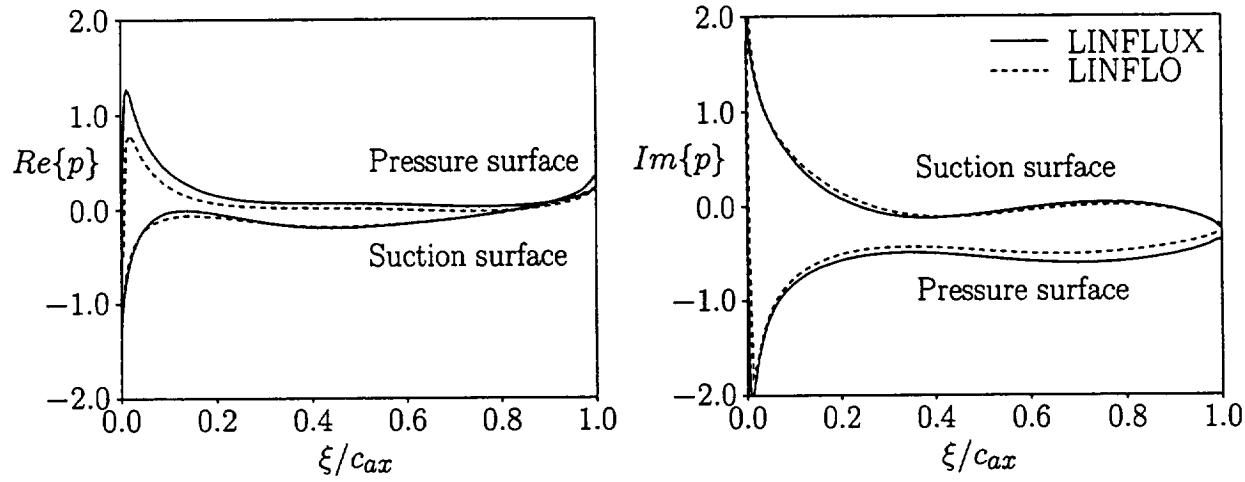

Figure 22: Unsteady surface pressure distributions at midspan ($r/r_D = 0.9$) due to the interaction of a vortical gust at $\omega = 3.861$ and $\sigma = -270\,\mathrm{deg}(N_V = 18)$ with the 3D 10th Standard Cascade.

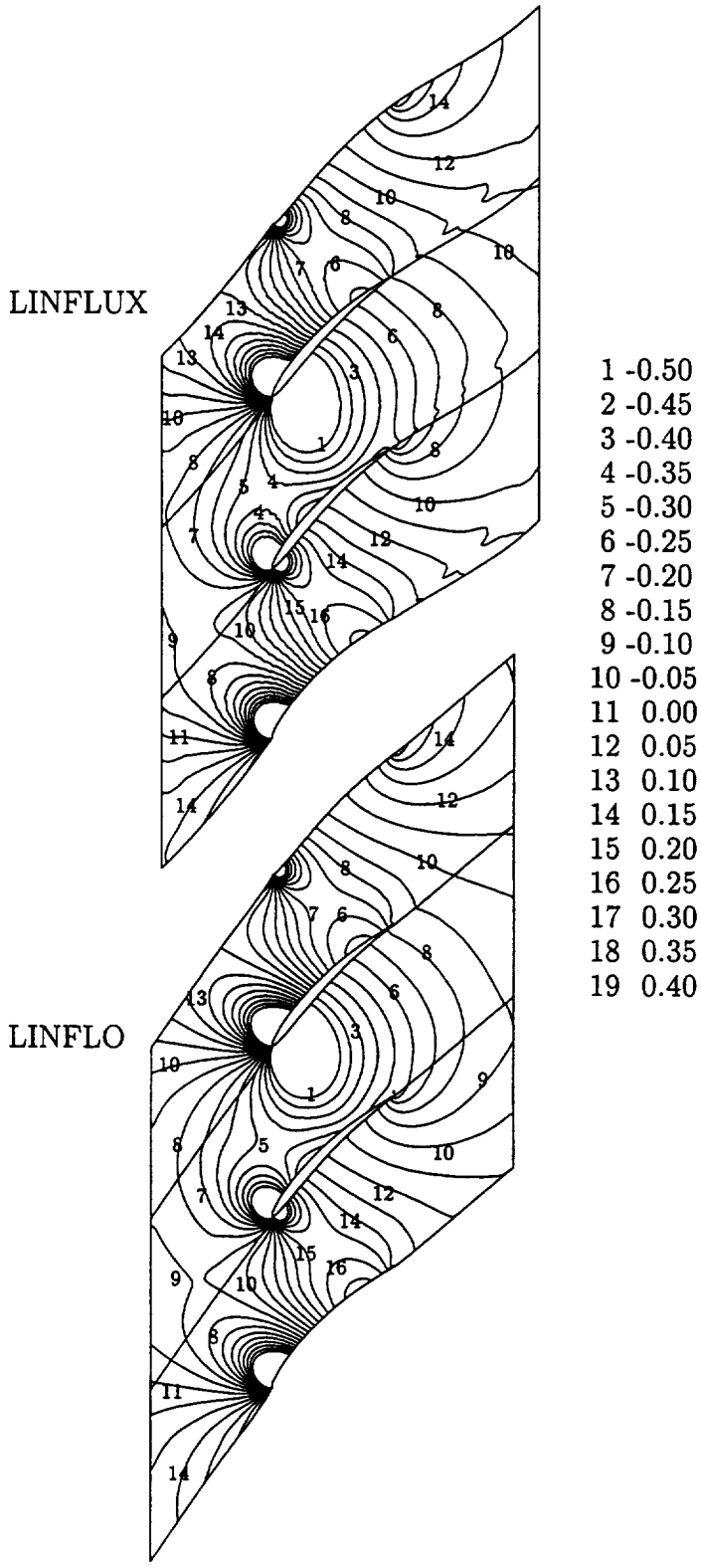

Figure 23: Contours of the in-phase component of the unsteady pressure at midspan due to the interaction of a vortical excitation at $\omega = 1.287$ and $\sigma = -90\,\text{deg}$ ($N_V = 6$) with the 3D 10th Standard Cascade.

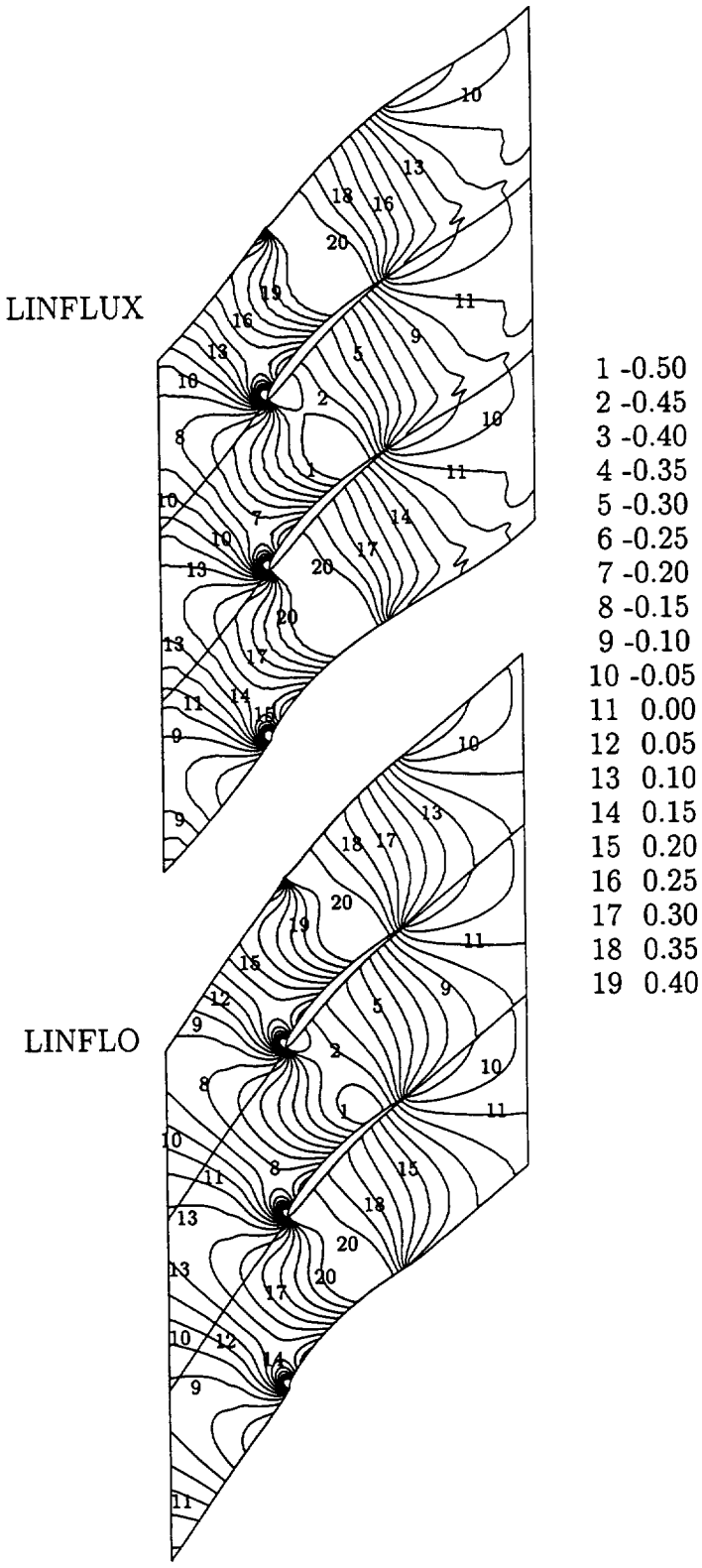

Figure 24: Contours of the in-phase component of the unsteady pressure at midspan due to the interaction of a vortical excitation at $\omega = 2.574$ and $\sigma = -180\,\text{deg}$ ($N_V = 12$) with the 3D 10th Standard Cascade.

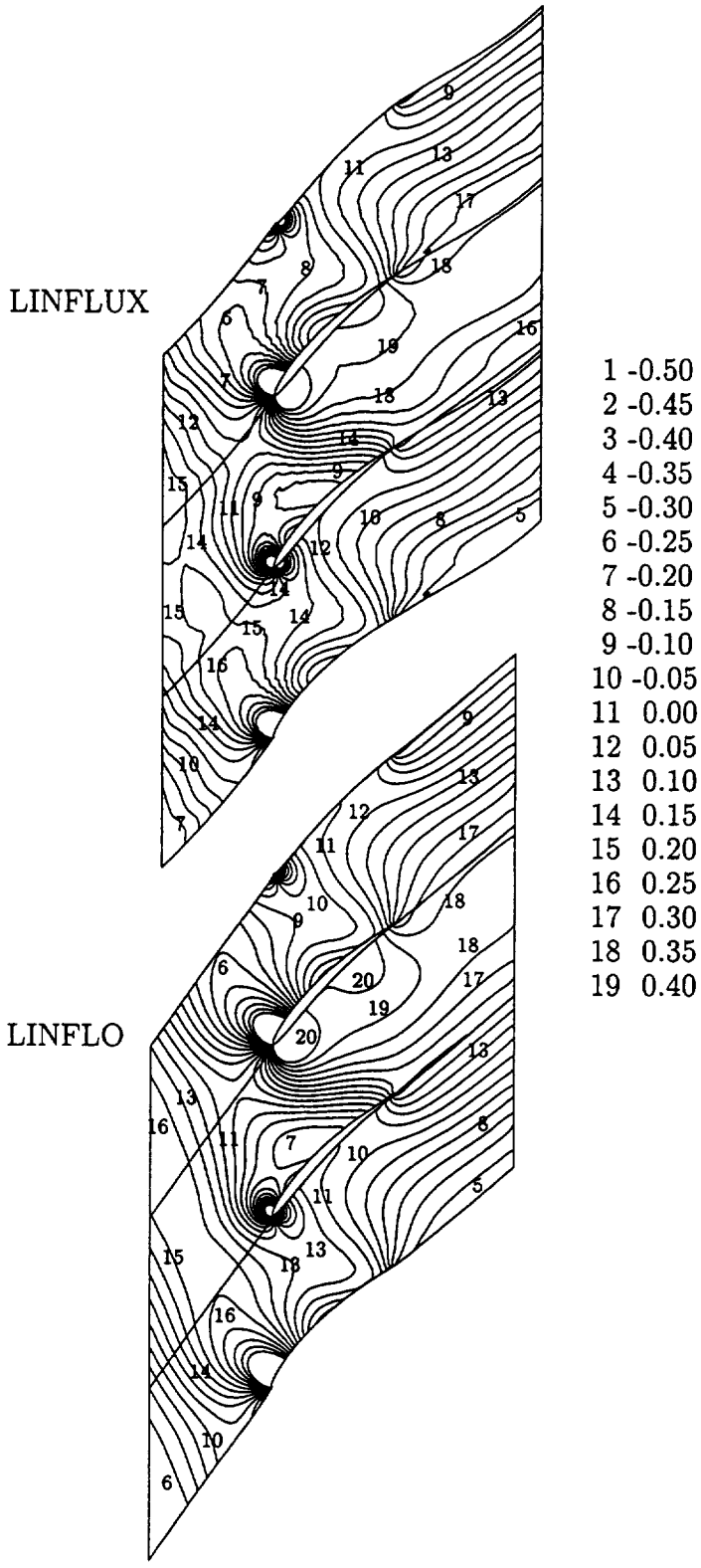

Figure 25: Contours of the in-phase component of the unsteady pressure at midspan due to the interaction of a vortical excitation at $\omega = 3.861$ and $\sigma = -270\,\text{deg}$ ($N_V = 18$) with the 3D 10th Standard Cascade.

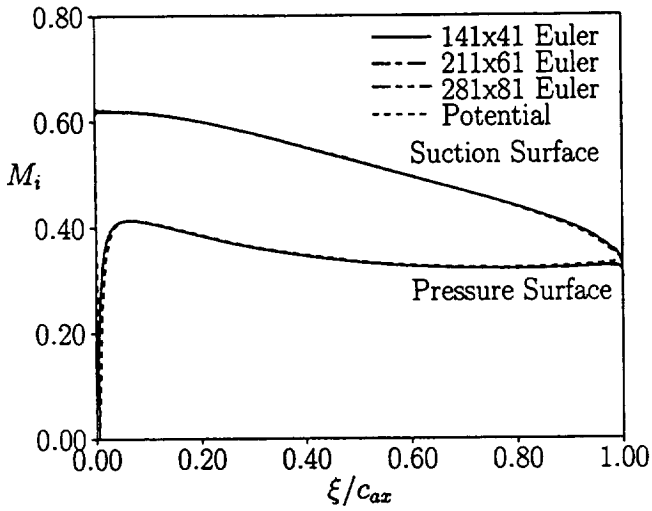

Figure 26: Relative, isentropic, surface, Mach number distributions for the 2D 10th Standard Cascade ($M_{-\infty} = 0.5$, $\Omega_{-\infty} = 55\,\text{deg}$).

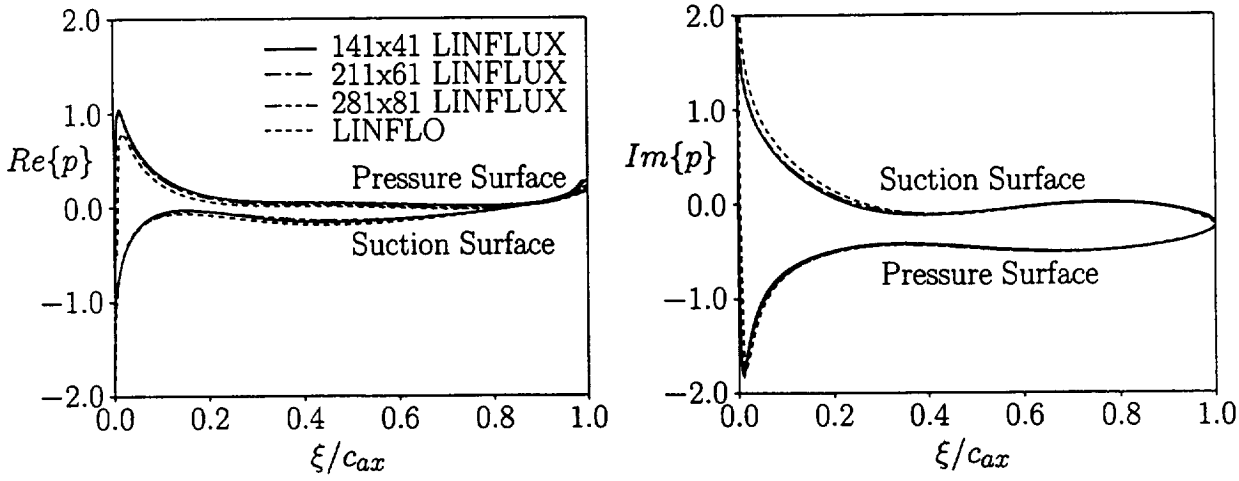

Figure 27: Unsteady surface pressure distributions due to the interaction of a vortical excitation at $\omega = 3.861$ and $\sigma = -270\,\text{deg}$ ($N_V = 18$) with the 2D 10th Standard Cascade.

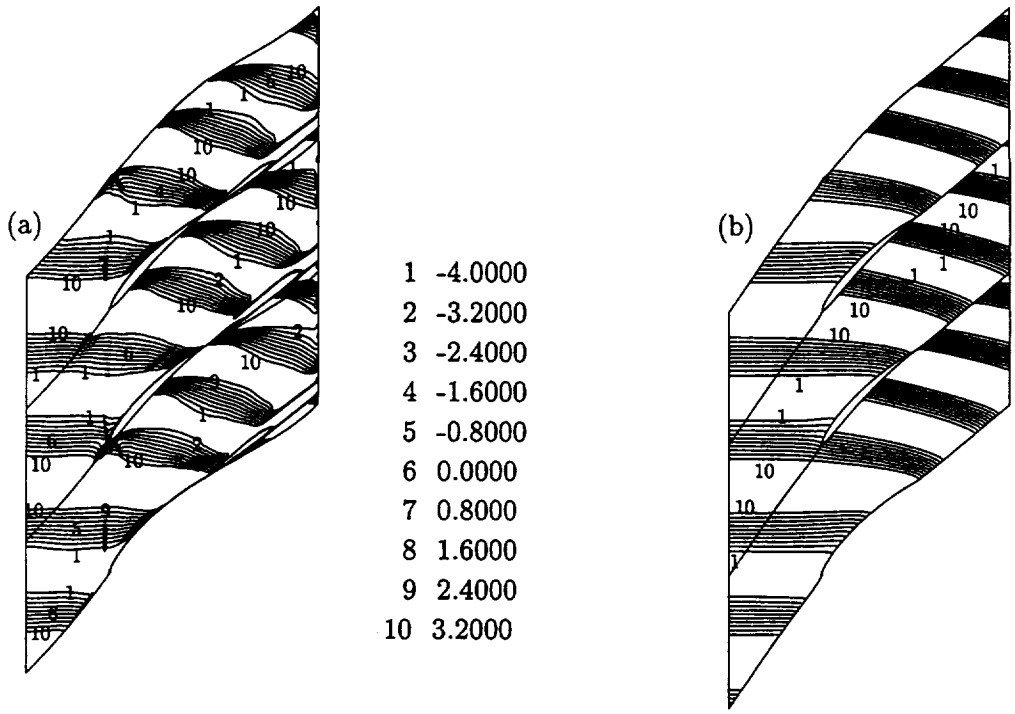

Figure 28: Contours of the in-phase component of the unsteady vorticity at midspan due to the interaction of a vortical gust at $\omega = 3.861$ and $\sigma = -270\,\mathrm{deg}$ ($N_V = 18$) with the 2D 10th Standard Cascade: (a) LINFLUX calculation on a 281 × 81 H-mesh; (b) LINFLO calculation.

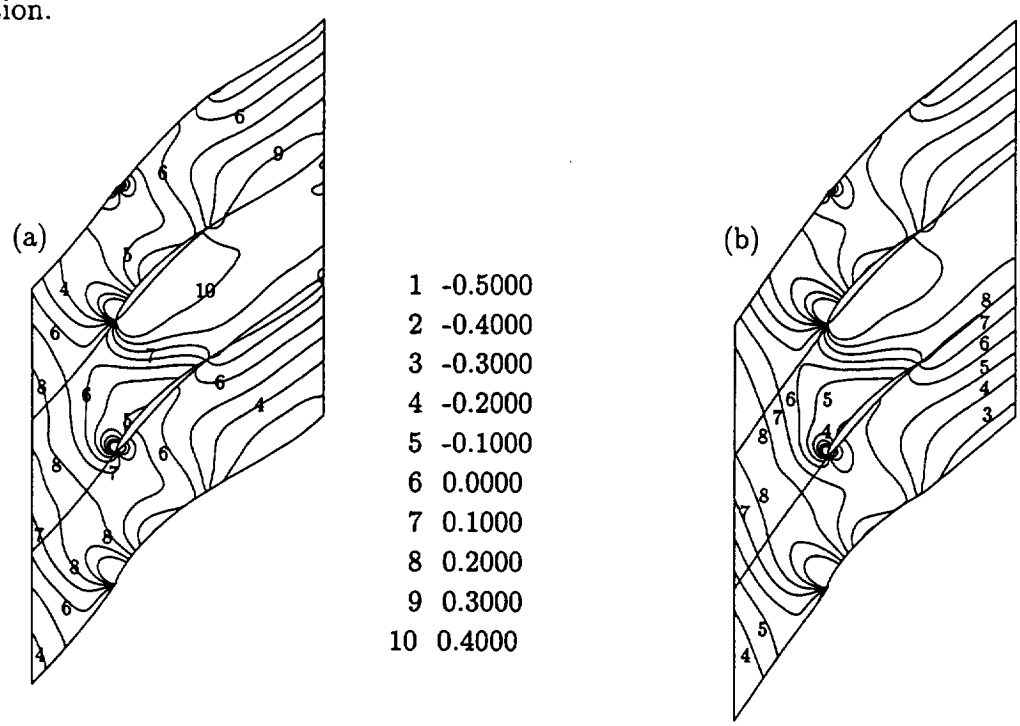

Figure 29: Contours of the in-phase component of the unsteady pressure at midspan due to the interaction of a vortical gust at $\omega = 3.861$ and $\sigma = -270\,\mathrm{deg}(N_V = 18)$ with the 2D 10th Standard Cascade: (a) LINFLUX calculation on a 281 × 81 H-mesh; (b) LINFLO calculation.

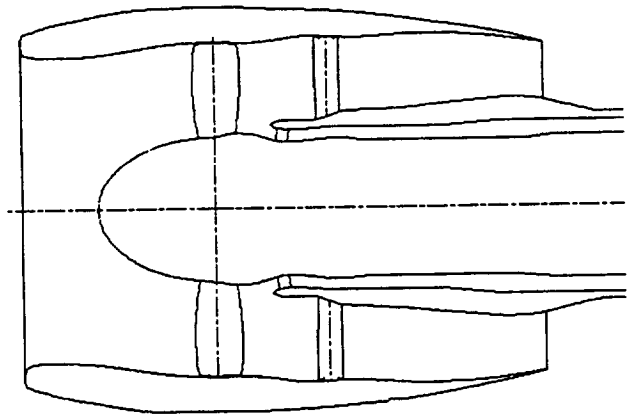

Figure 30: Schematic of the PW/NASA 22 inch advanced ducted propulsor (ADP).

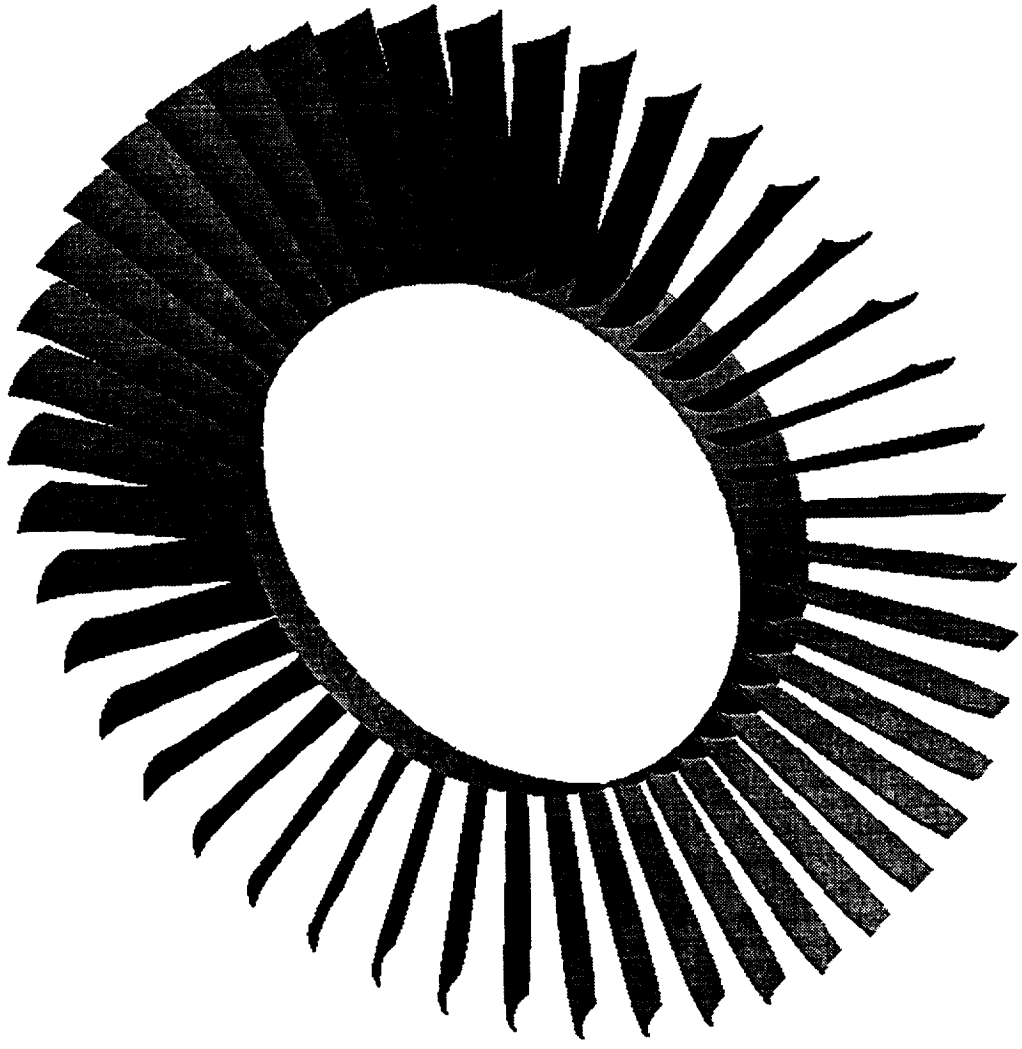

Figure 31: Fan exit guide vane of the 22 inch ADP.

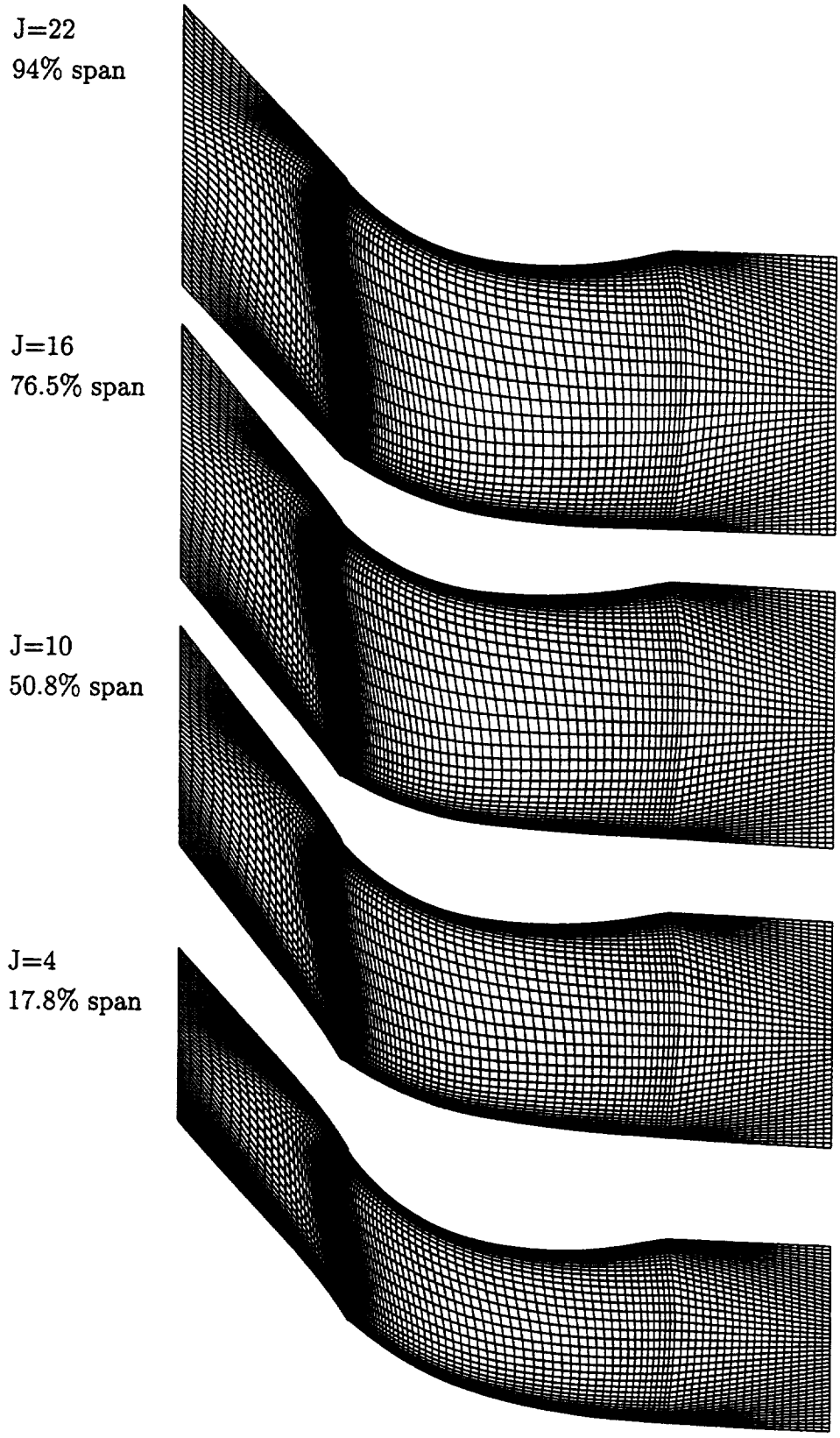

Figure 32: LINFLUX computational grid, at 4 radial stations, for the fan exit guide vane.

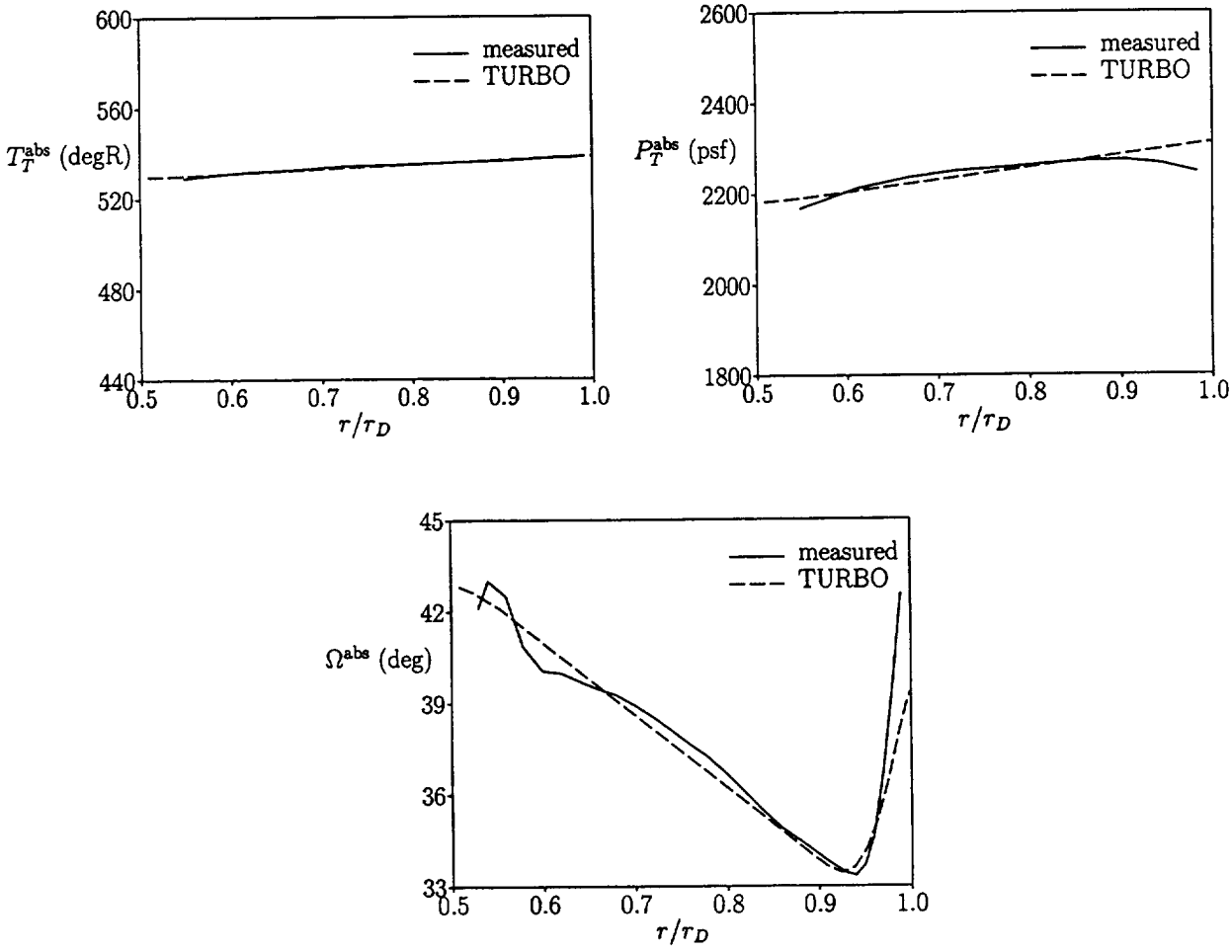

Figure 33: Steady flow properties far upstream of the FEGV.

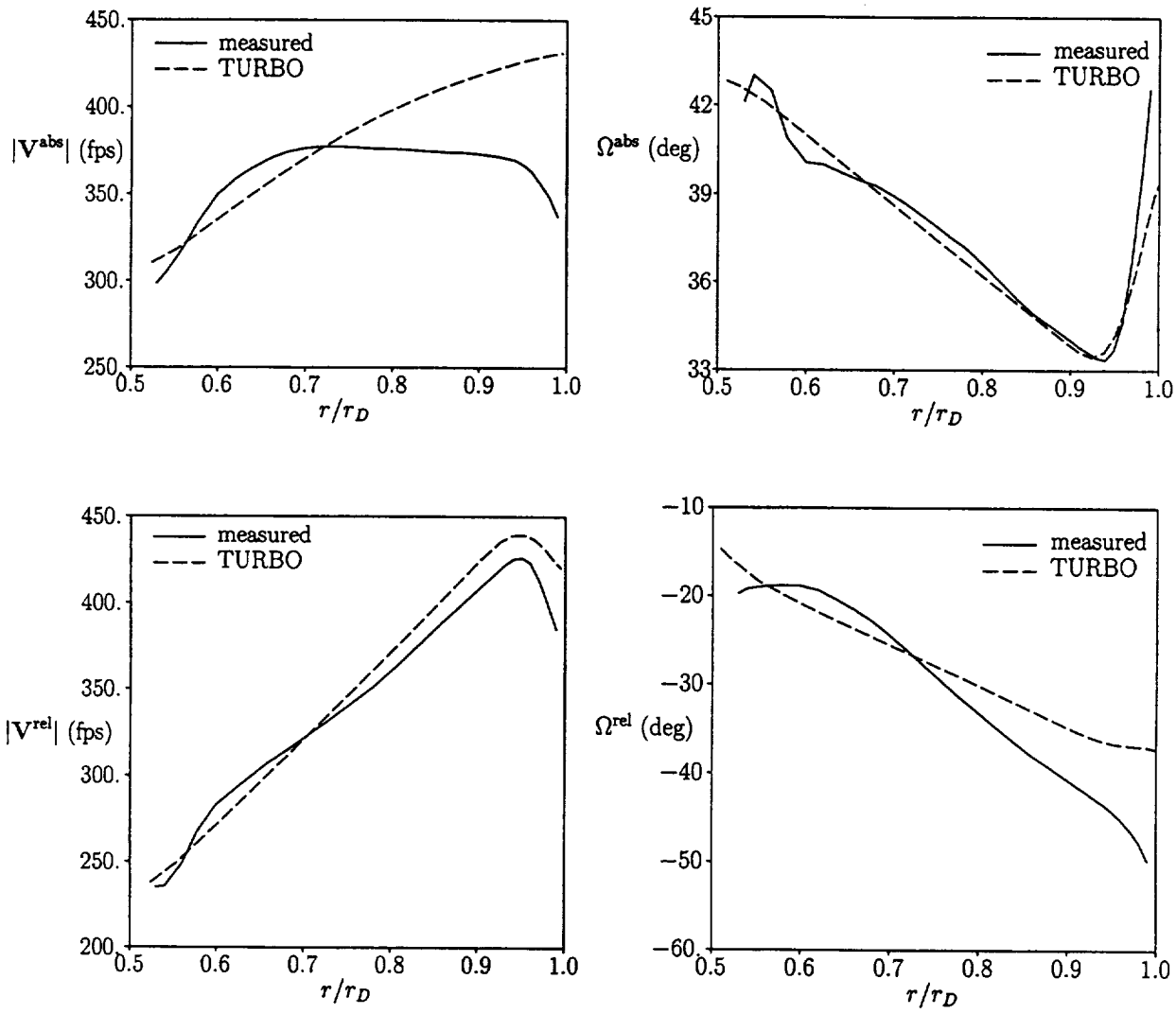

Figure 34: Absolute and relative frame velocities at the fan exit (FEGV inlet).

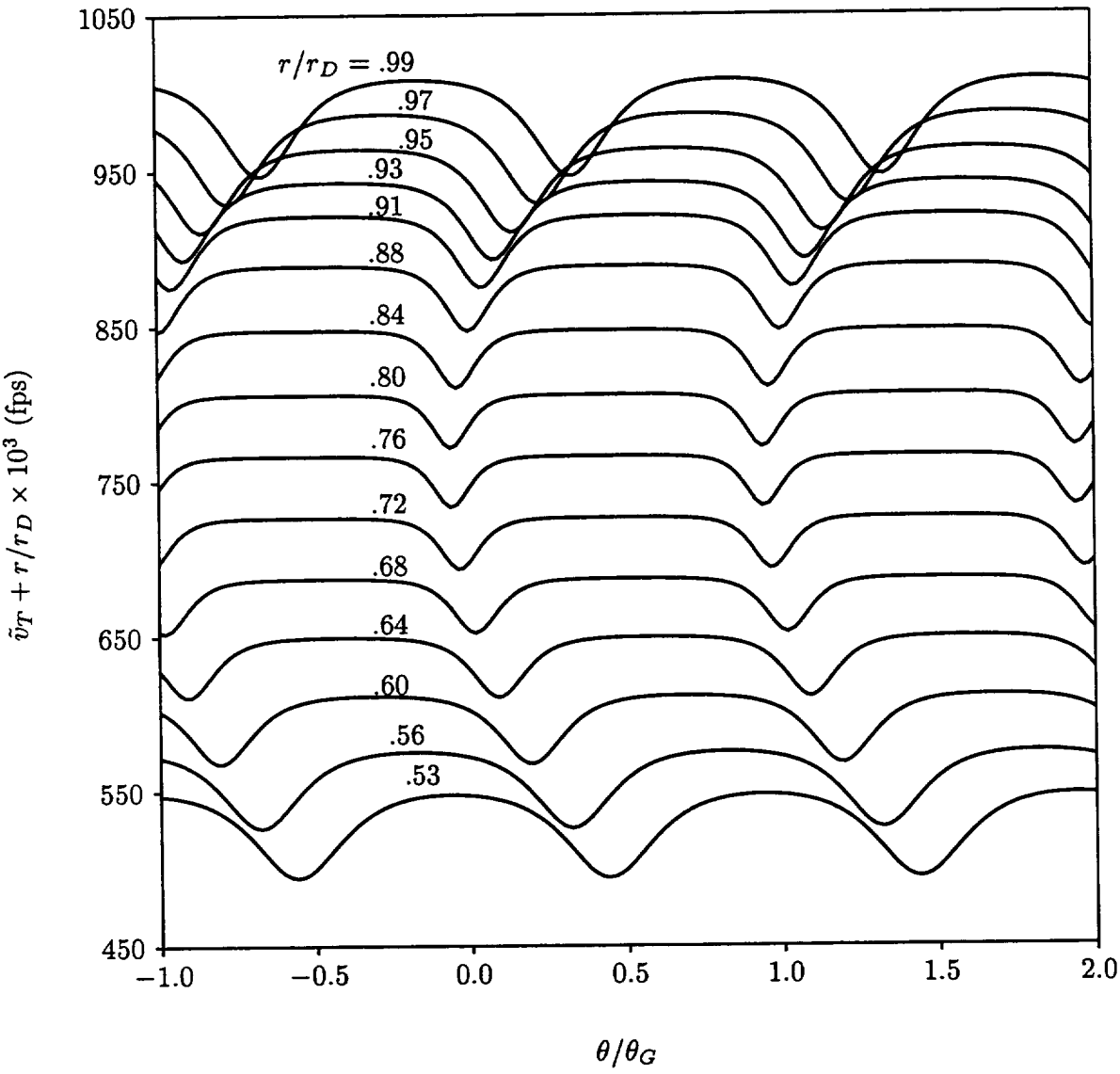

Figure 35: Analytic rotor-wake tangential velocity perturbations at FEGV midspan leading-edge plane ($\xi = 0$).

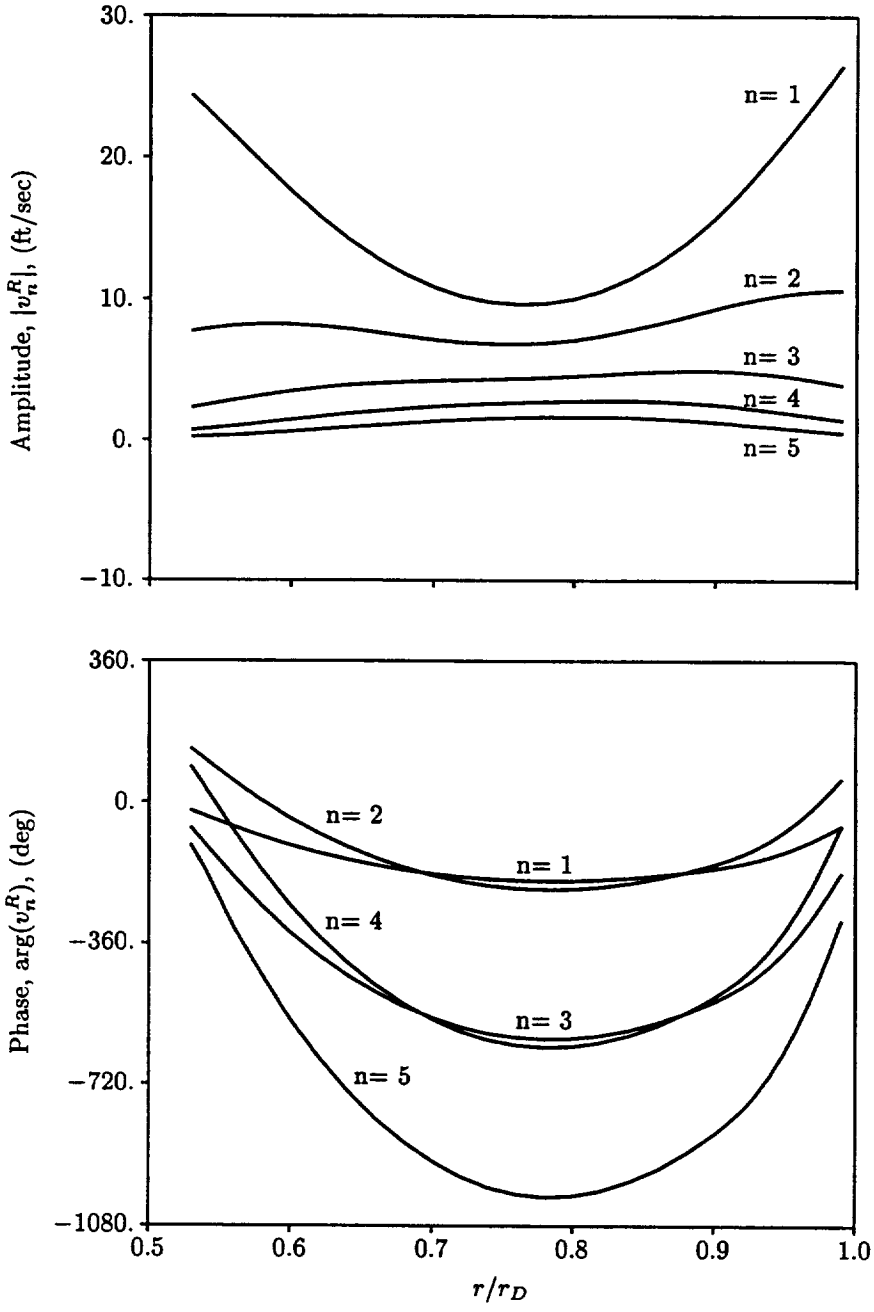

Figure 36: Fourier components of the analytic wake excitation velocity, $\tilde{v}_T$.

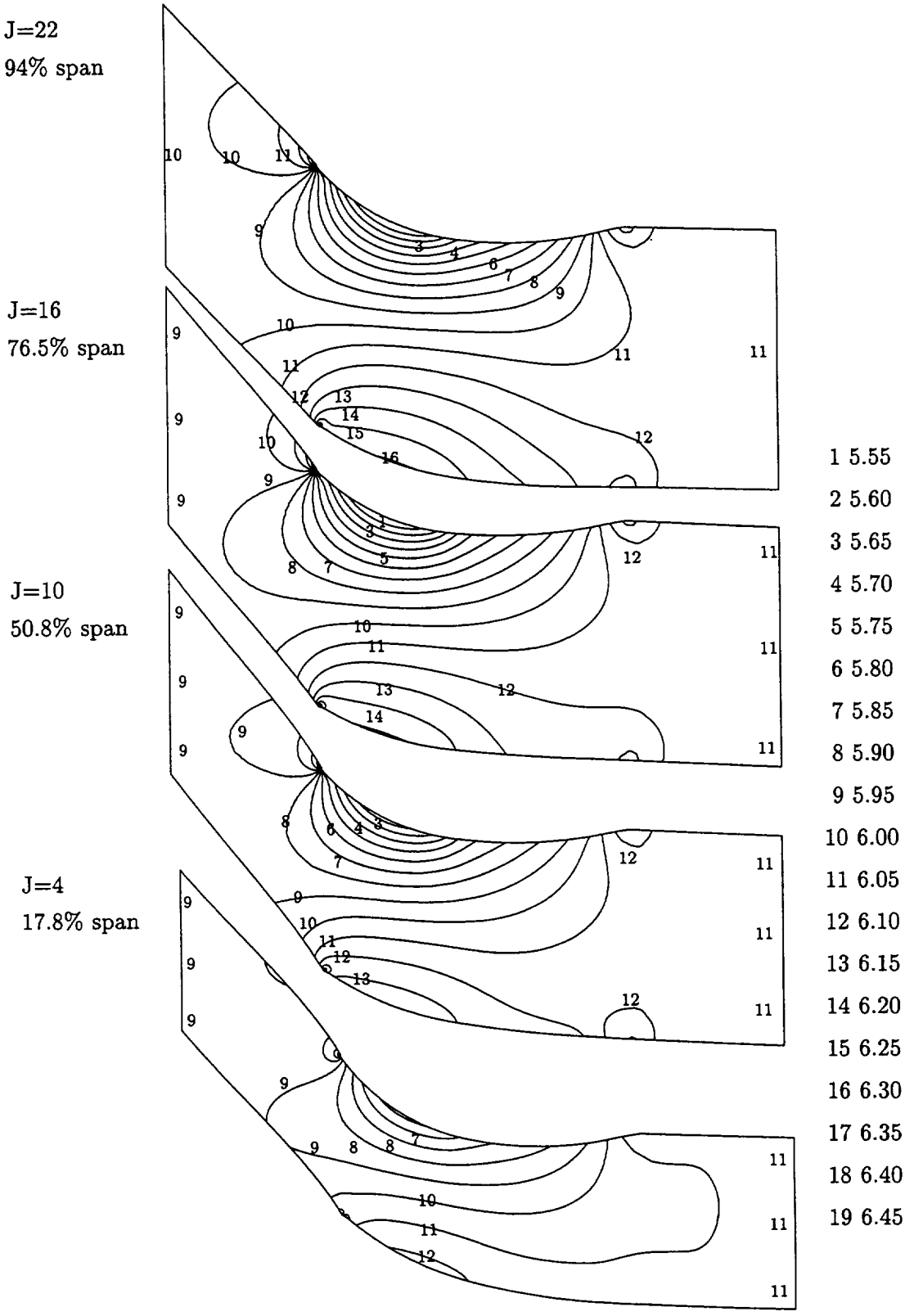

Figure 37: FEGV steady pressure field at four radial stations.

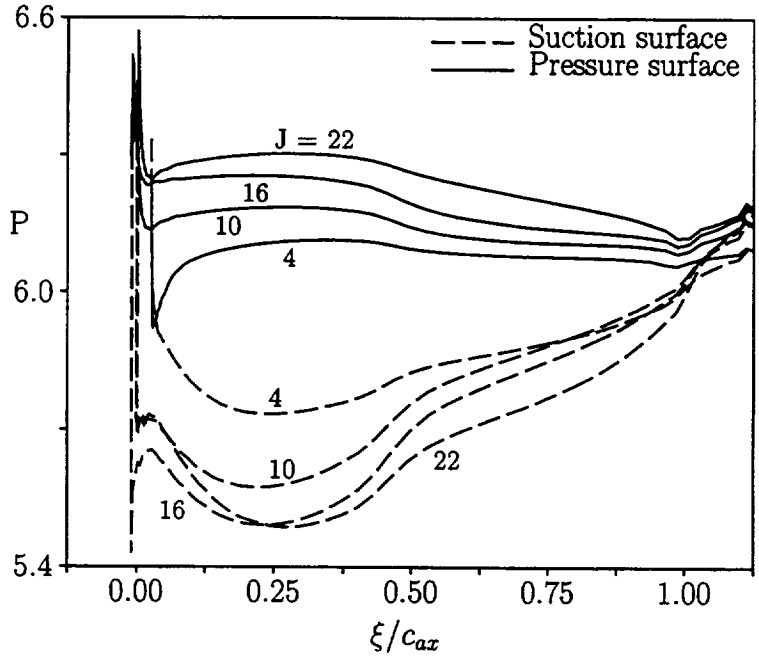

Figure 38: FEGV steady surface pressure distributions at four radial stations.

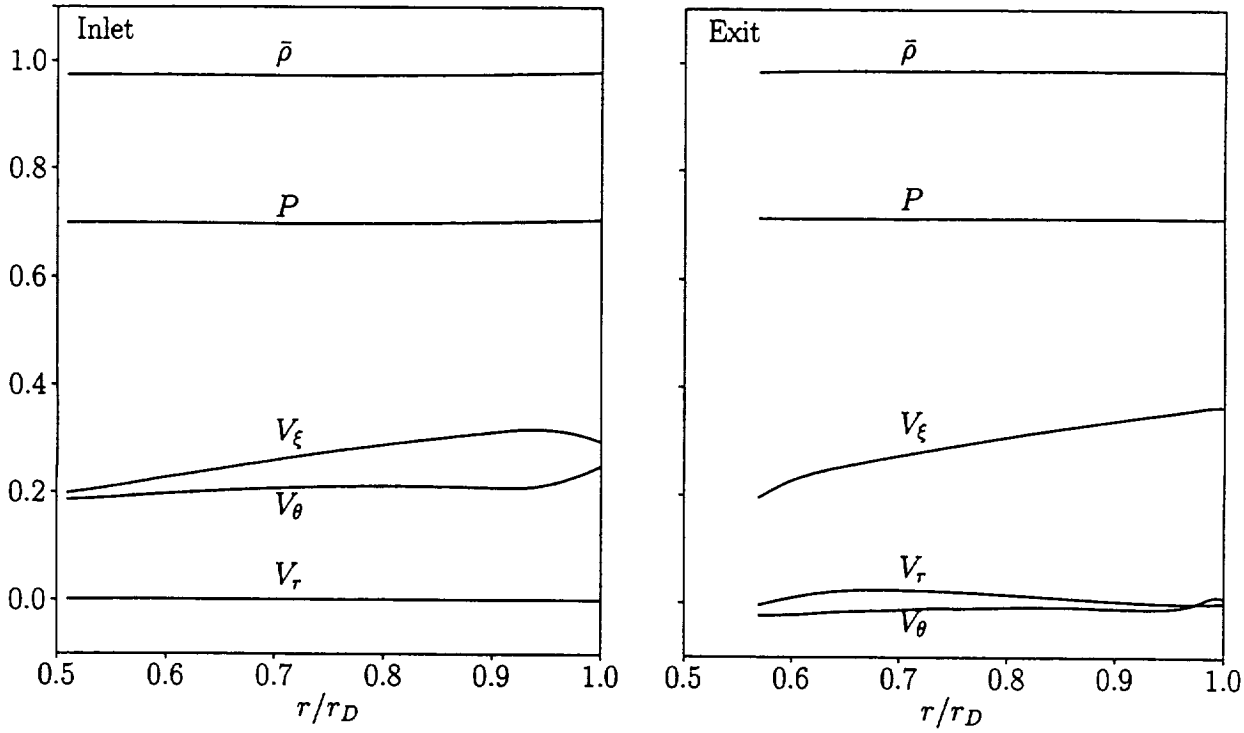

Figure 39: Absolute frame steady flow properties at the computational inlet and exit planes of the fan exit guide vane (FEGV).

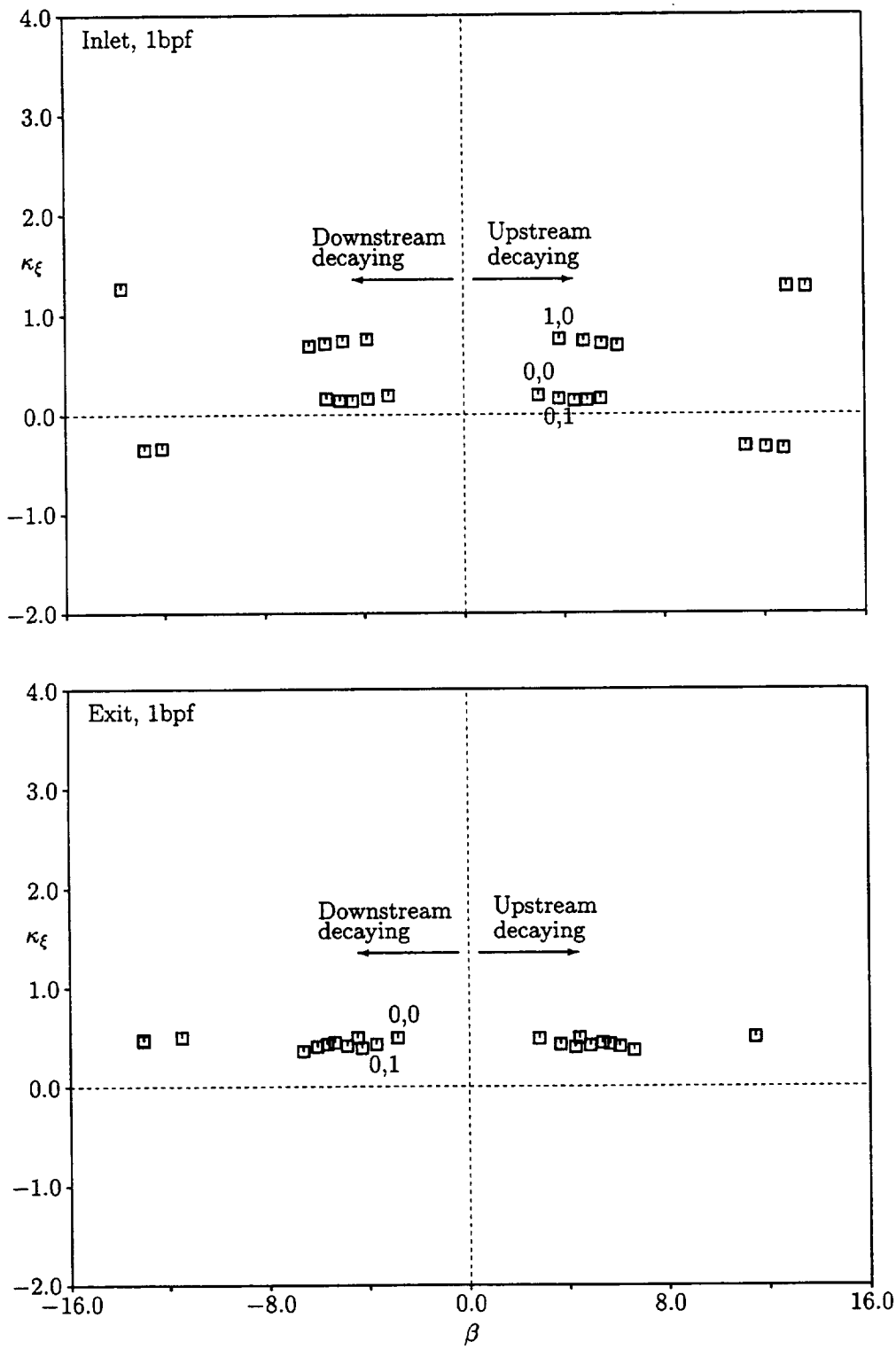

Figure 40: Axial eigenvalues, $\chi = \beta + i\kappa_\xi$, of acoustic disturbances far upstream and far downstream of the fan exit guide vane (FEGV) subjected to an unsteady excitation at 1BPF ($\omega = 3.658$ and $\sigma = -144.0\,\mathrm{deg}$).

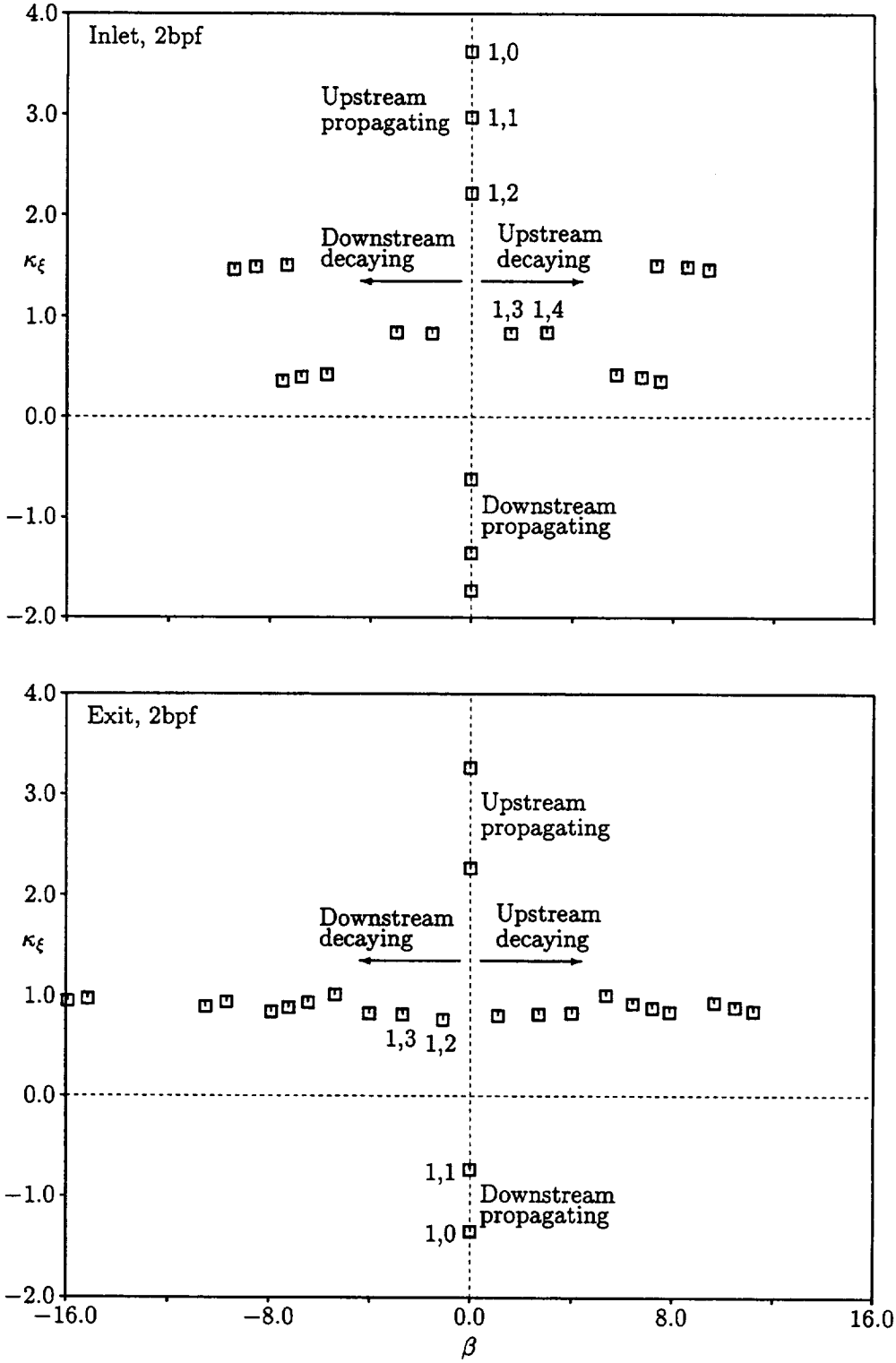

Figure 41: Axial eigenvalues, $\chi = \beta + i\kappa_\xi$, of acoustic disturbances far upstream and far downstream of the FEGV subjected to an unsteady excitation at 2BPF ($\omega = 7.317$ and $\sigma = -288.0\,\text{deg}$).

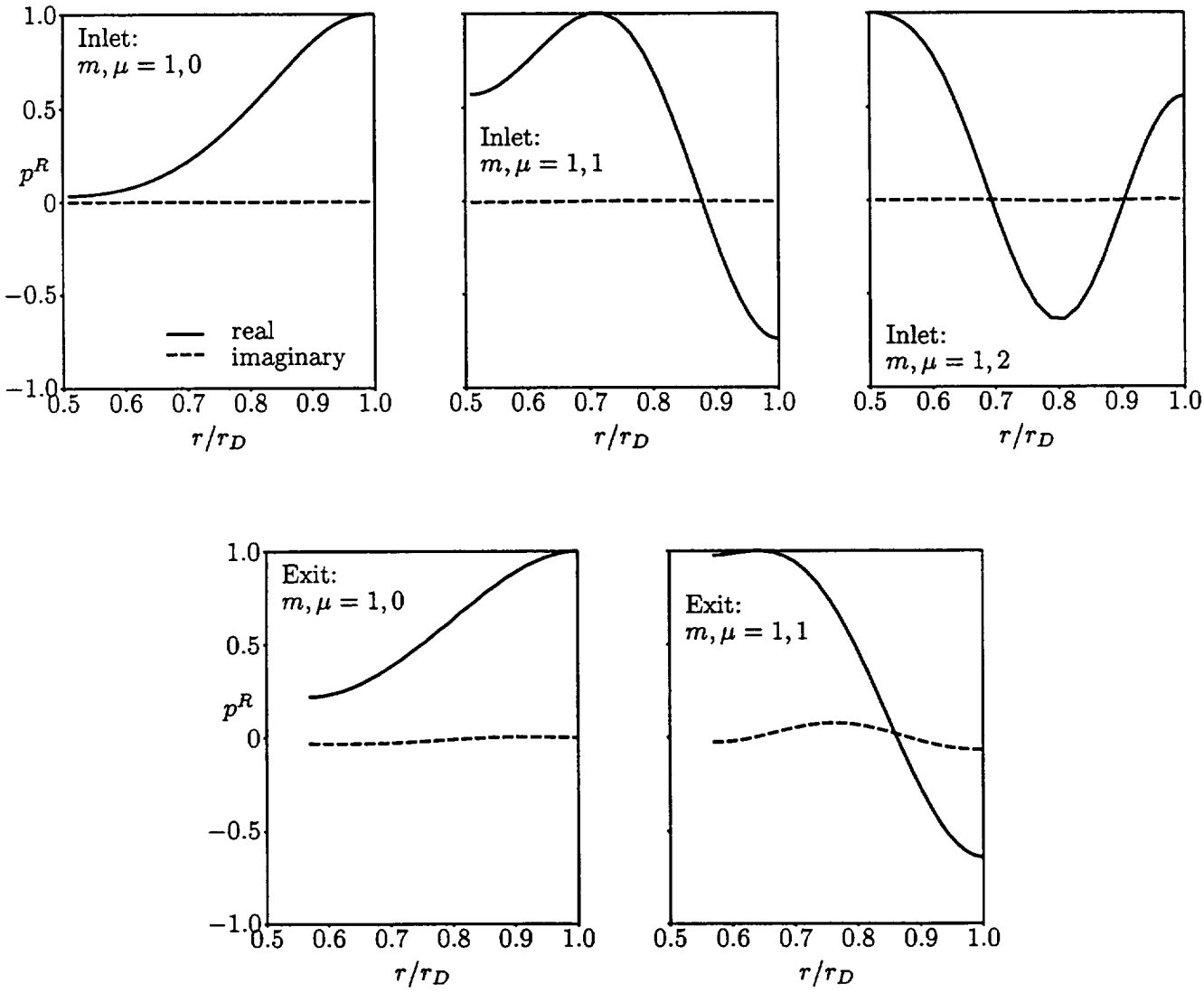

Figure 42: Radial pressure modes of the propagating acoustic responses far upstream and far downstream of the FEGV subjected to an unsteady excitation at 2BPF ($\omega = 7.317$ and $\sigma = -288.0\,\text{deg}$): (———) real part of $p^R_{m\mu}$, (− − −) imaginary part of $p^R_{m\mu}$.

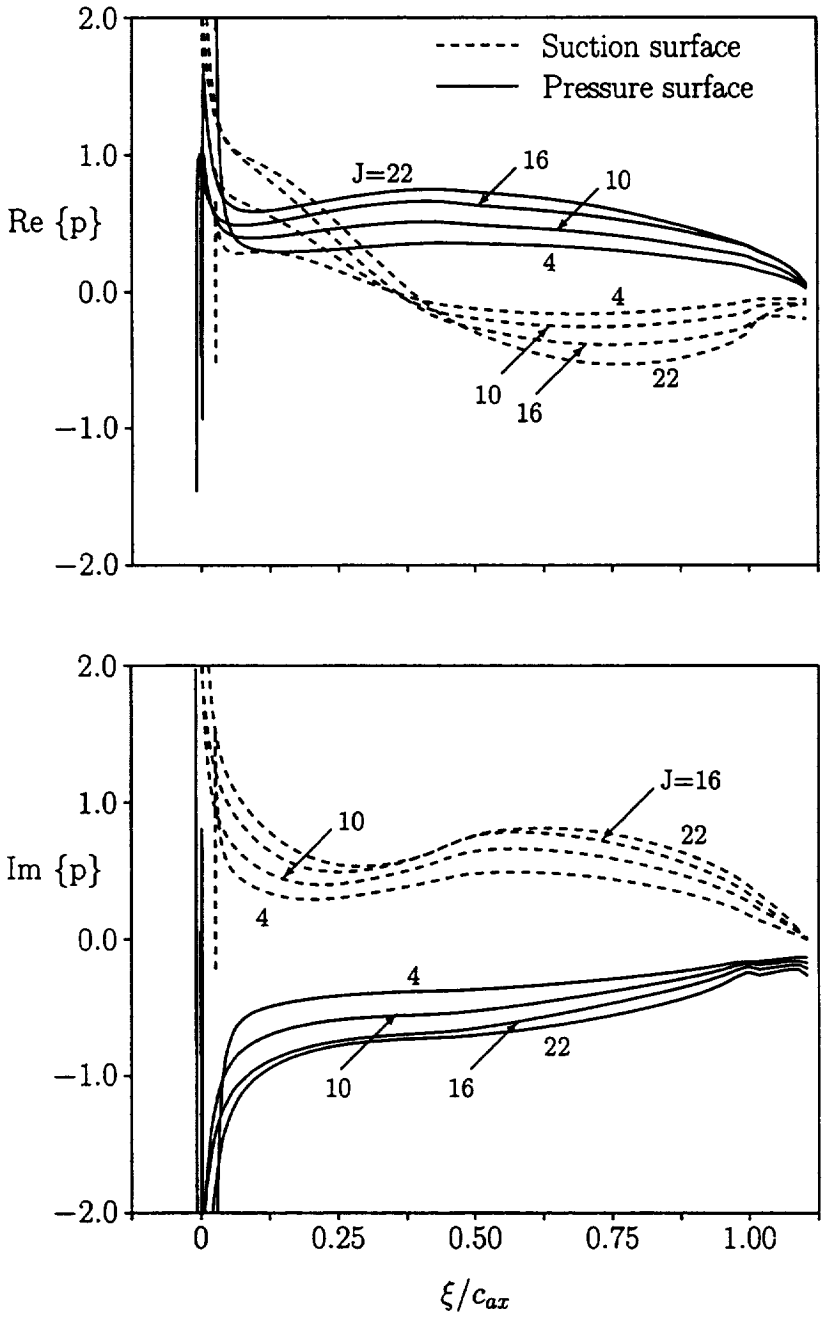

Figure 43: Unsteady surface pressure distributions at 17.8 (J=4), 50.8 (J=10), 76.5 (J=16) and 94.0 (J=22) percent span for the FEGV subjected to the 1BPF test excitation.

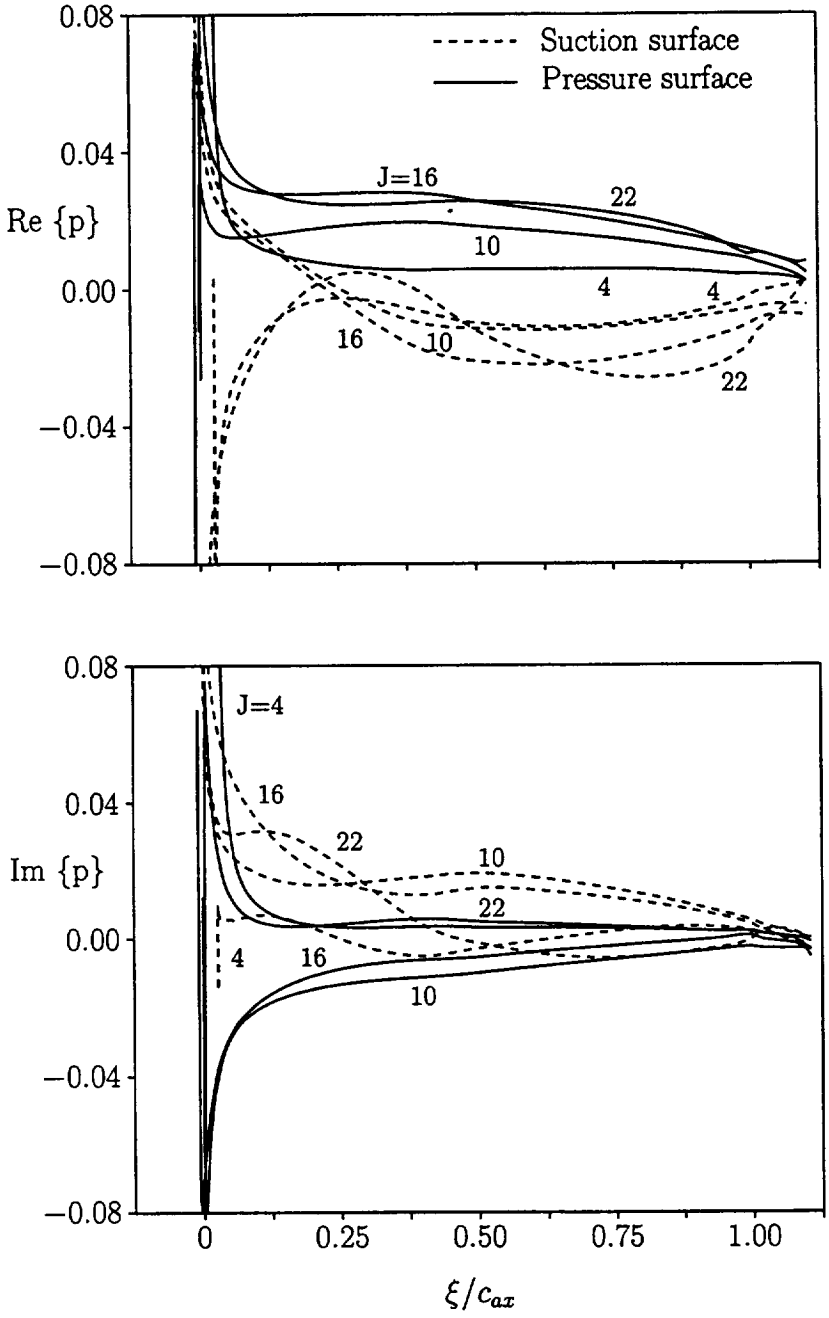

Figure 44: Unsteady surface pressure distributions at 17.8 (J=4), 50.8 (J=10), 76.5 (J=16) and 94.0 (J=22) percent span for the FEGV subjected to the 1BPF wake excitation.

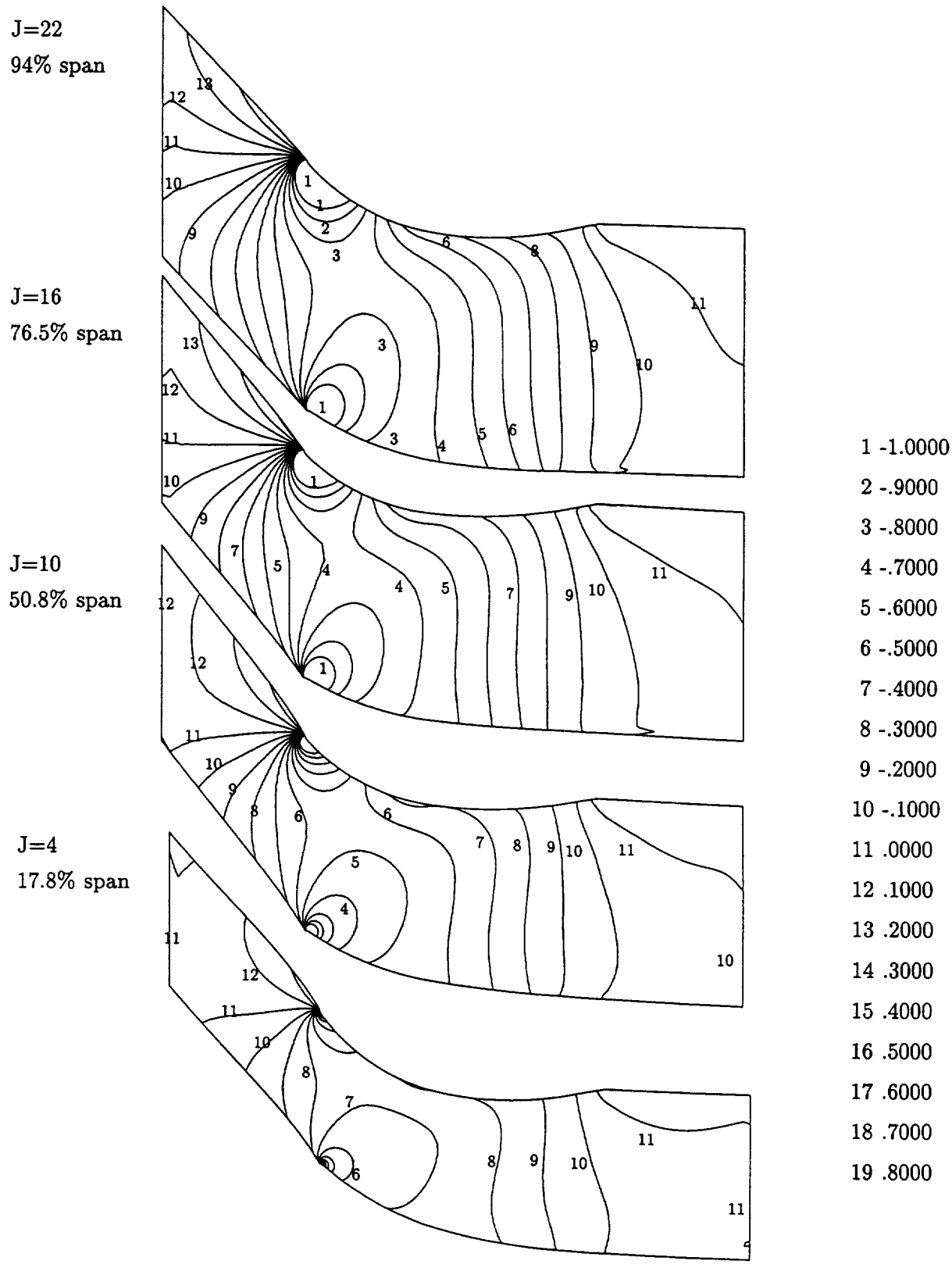

Figure 45: Unsteady pressure field, at four radial stations, for the FEGV subjected to the 1BPF test excitation.

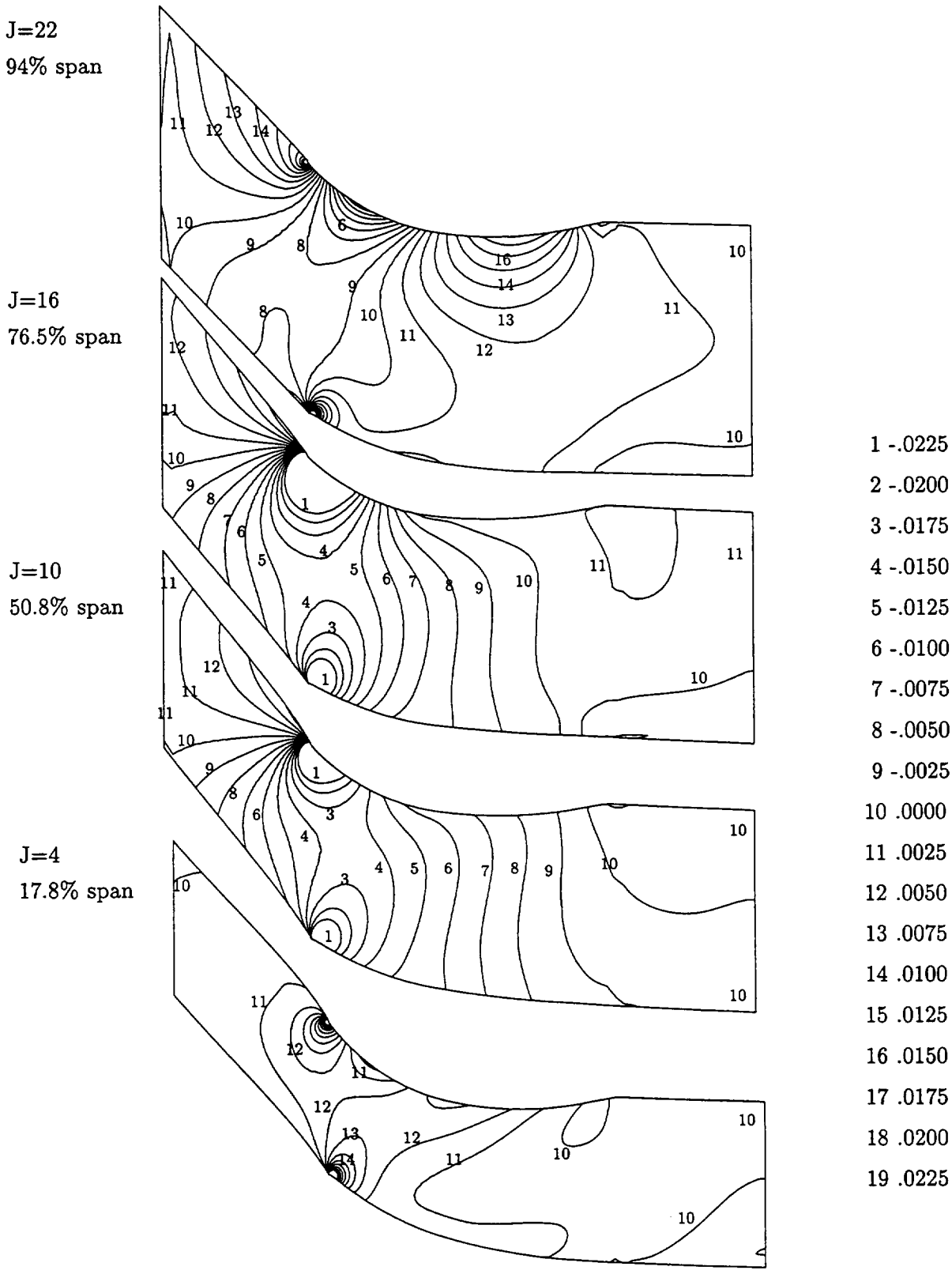

Figure 46: Unsteady pressure field, at four radial stations, for the FEGV subjected to the 1BPF wake excitation.

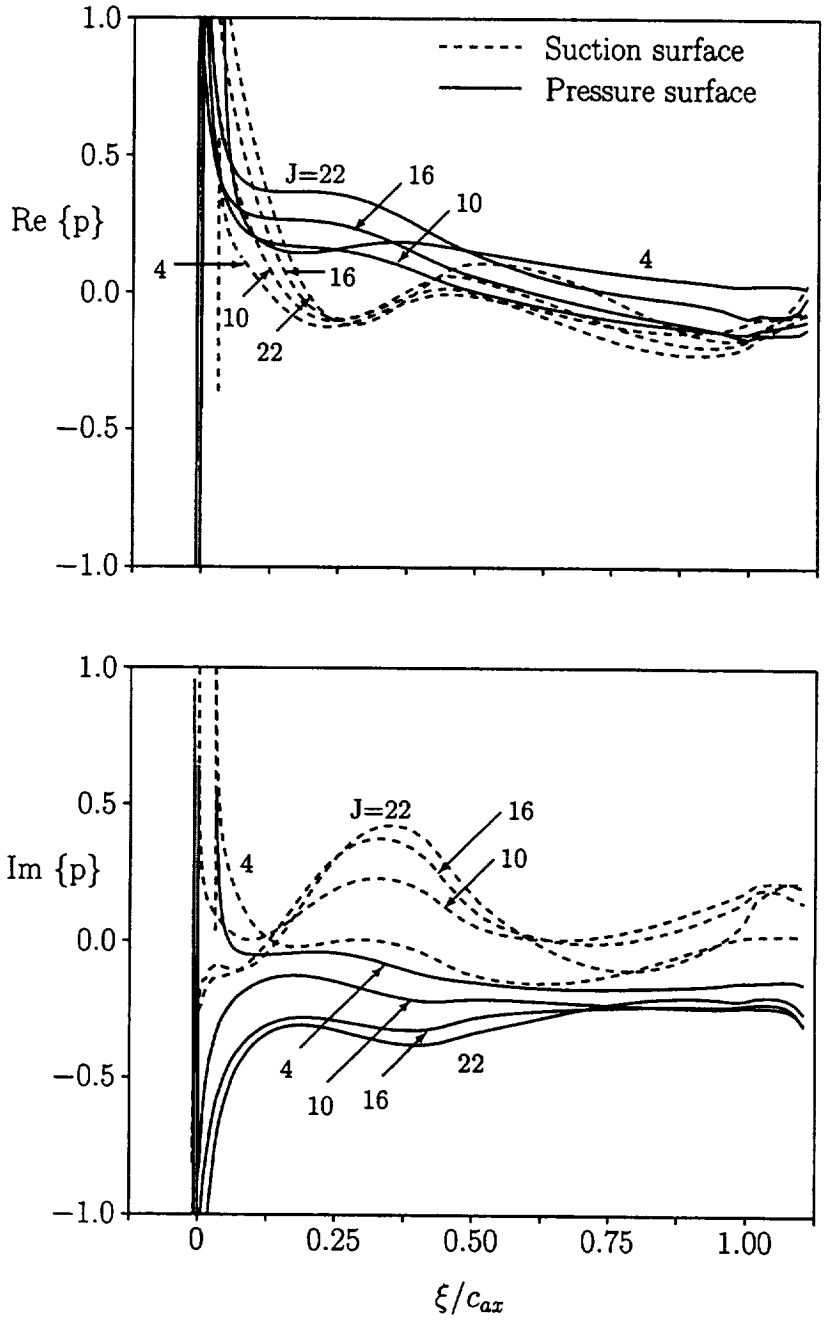

Figure 47: Unsteady surface pressure distributions at 17.8 (J=4), 50.8 (J=10), 76.5 (J=16) and 94.0 (J=22) percent span for the FEGV subjected to the 2BPF test excitation.

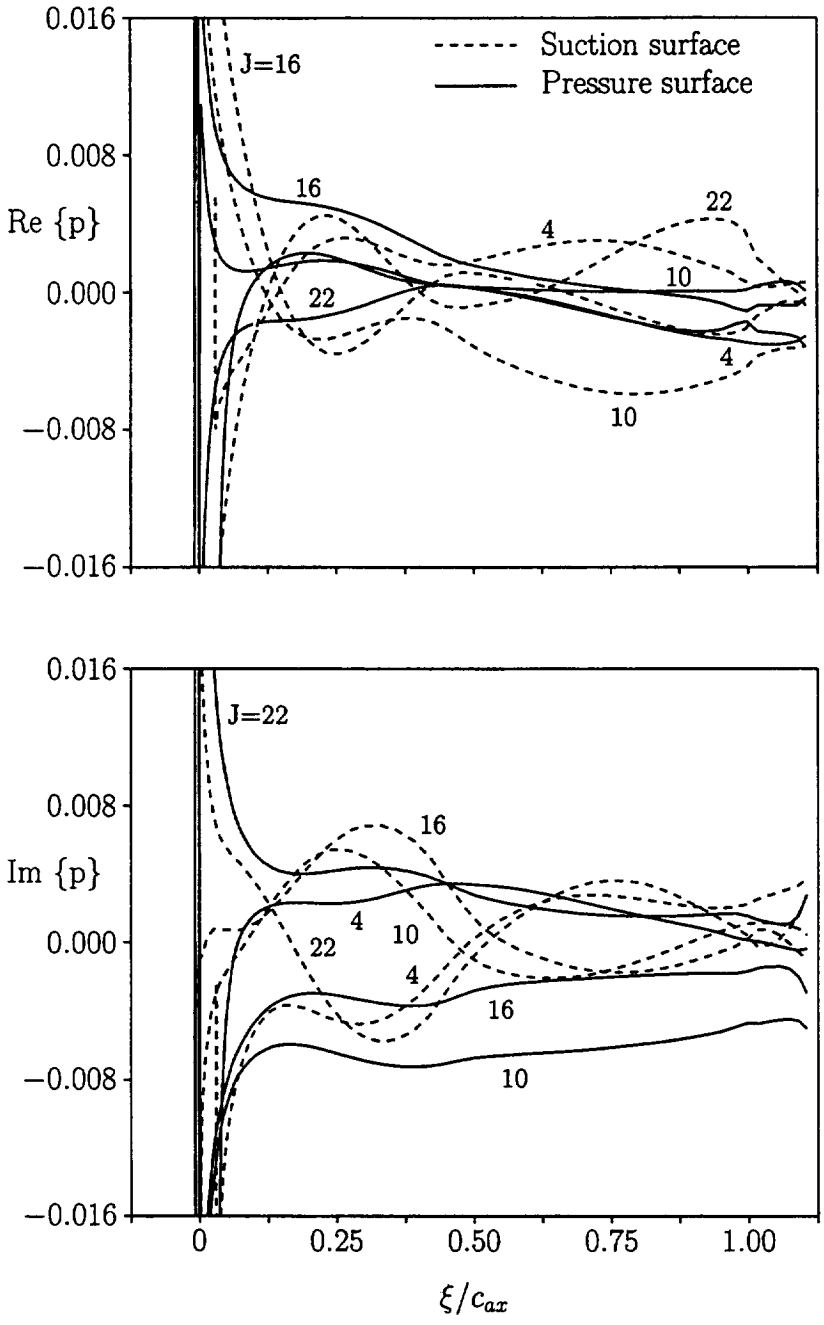

Figure 48: Unsteady surface pressure distributions at 17.8 (J=4), 50.8 (J=10), 76.5 (J=16) and 94.0 (J=22) percent span for the FEGV subjected to the 2BPF wake excitation.

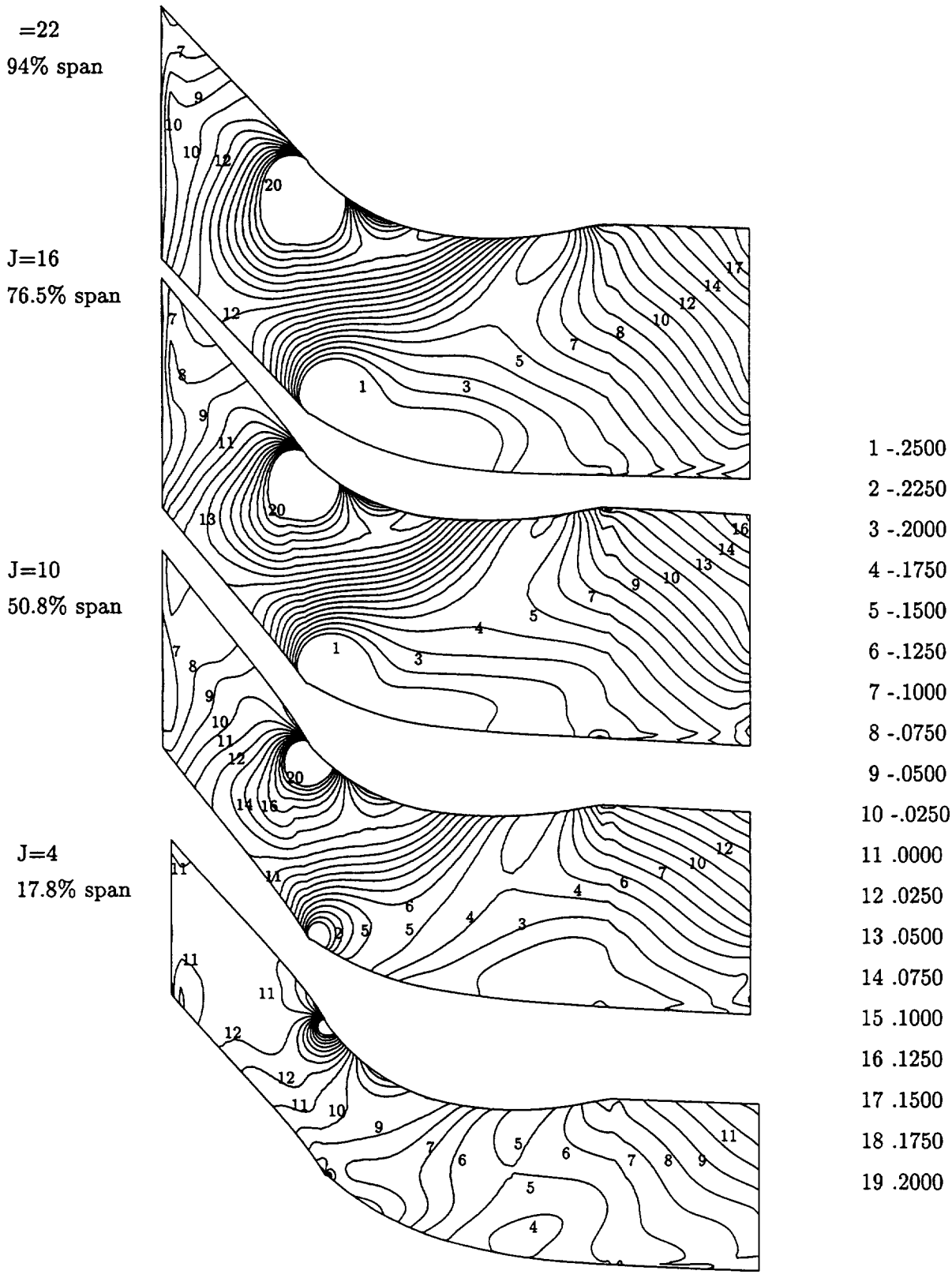

Figure 49: Unsteady pressure field, at four radial stations, for the FEGV subjected to the 2BPF test excitation.

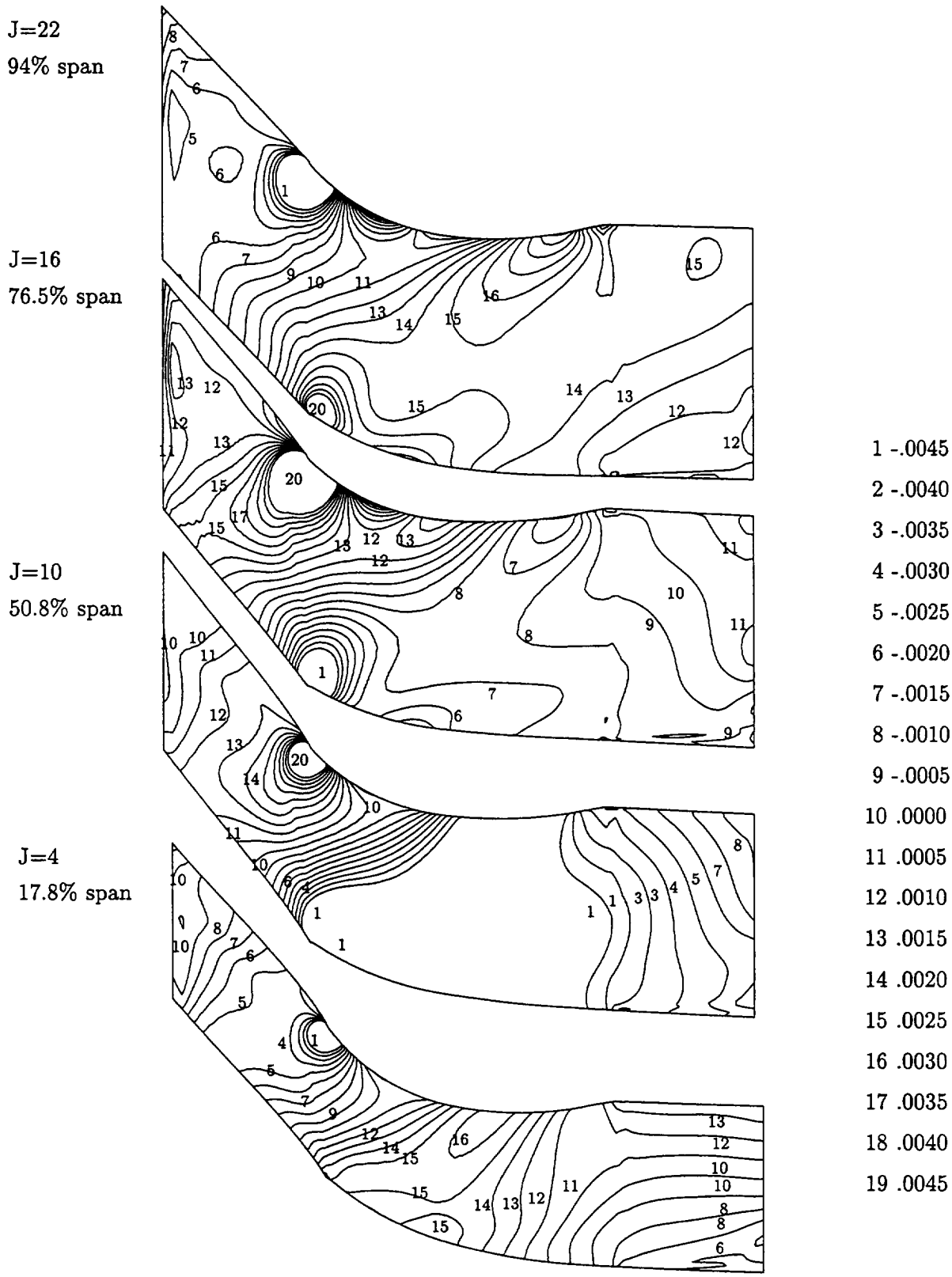

Figure 50: Unsteady pressure field, at four radial stations, for the FEGV subjected to the 2BPF wake excitation.

REPORT DOCUMENTATION PAGE

Form Approved
OMB No. 0704-0188

1. AGENCY USE ONLY (*Leave blank*)	2. REPORT DATE	3. REPORT TYPE AND DATES COVERED
	March 1999	Final Contractor Report

4. TITLE AND SUBTITLE

Development of a Linearized Unsteady Euler Analysis With Application to Wake/Blade-Row Interactions

5. FUNDING NUMBERS

WU–538–03–11–00
NAS3–27727

6. AUTHOR(S)

Joseph M. Verdon, Matthew D. Montgomery, and H. Andrew Chuang

7. PERFORMING ORGANIZATION NAME(S) AND ADDRESS(ES)

United Technologies Research Center
Aeromechanical, Chemical, and Fluid Systems
411 Silver Lane
East Hartford, Connecticut 06108

8. PERFORMING ORGANIZATION REPORT NUMBER

E–11597

9. SPONSORING/MONITORING AGENCY NAME(S) AND ADDRESS(ES)

National Aeronautics and Space Administration
John H. Glenn Research Center at Lewis Field
Cleveland, Ohio 44135–3191

10. SPONSORING/MONITORING AGENCY REPORT NUMBER

NASA CR—1999-208879
UTRC Report R98–4.101.0255

11. SUPPLEMENTARY NOTES

Project Manager, Dennis L. Huff, NASA Lewis Research Center, organization code 5940, (216) 433–3913.

12a. DISTRIBUTION/AVAILABILITY STATEMENT

Unclassified - Unlimited
Subject Category: 71 Distribution: Nonstandard

This publication is available from the NASA Center for AeroSpace Information, (301) 621–0390.

12b. DISTRIBUTION CODE

13. ABSTRACT (***Maximum 200 words***)

A three-dimensional, linearized, Euler analysis is being developed to provide a comprehensive and efficient unsteady aerodynamic analysis for predicting the aeroacoustic and aeroelastic responses of axial-flow turbomachinery blading. The mathematical models needed to describe nonlinear and linearized, inviscid, unsteady flows through a blade row operating within a cylindrical annular duct are presented in this report. A numerical model for linearized inviscid unsteady flows, which couples a near-field, implicit, wave-split, finite volume analysis to far-field eigenanalyses, is also described. The linearized aerodynamic and numerical models have been implemented into the three-dimensional unsteady flow code, LINFLUX. This code is applied herein to predict unsteady subsonic flows driven by wake or vortical excitations. The intent is to validate the LINFLUX analysis via numerical results for simple benchmark unsteady flows and to demonstrate this analysis via application to a realistic wake/blade-row interaction. Detailed numerical results for a three-dimensional version of the 10th Standard Cascade and a fan exit guide vane indicate that LINFLUX is becoming a reliable and useful unsteady aerodynamic prediction capability that can be applied, in the future, to assess the three-dimensional flow physics important to blade-row, aeroacoustic and aeroelastic responses.

14. SUBJECT TERMS	15. NUMBER OF PAGES
Acoustics; Turbomachinery; Noise fans	100
	16. PRICE CODE: A05

17. SECURITY CLASSIFICATION OF REPORT	18. SECURITY CLASSIFICATION OF THIS PAGE	19. SECURITY CLASSIFICATION OF ABSTRACT	20. LIMITATION OF ABSTRACT
Unclassified	Unclassified	Unclassified	